Coil Development for 7 Tesla Magnetic Resonance Imaging of The Prostate

Aleksej Polpudenko

Submitted in fulfilment of the requirements of the Degree of Doctor of Philosophy

School of Psychology and Neuroscience,
College of Medical, Veterinary and Life Sciences,
University of Glasgow

December, 2024

Contents

List of Figures

List of Tables

Acknowledgements

I thankfully acknowledge the following contributions to the work presented in this thesis: provision of the TR switch, cable trap and shield designs by Dr. Shajan Gunamony; Dr. Paul McElhinney's and Dr. Sarah Alwood-Spiers's help with phantom solution preparation; the coil's temperature mapping data produced by Dr. Sarah Allwood-Spiers; DWI images from a volunteer scan acquired by Prof. David Porter; hosting of the array comparison session in Oxford and satTFL B_1+ mapping by Prof. Aaron Hess; Siemens for providing the VOP compression tool.

Abstract

Prostate imaging performed on the contemporary 1.5-3 T clinical magnetic resonance imaging (MRI) systems has proven to be of great benefit within the context of prostate cancer management. The use of multi-parametric MRI (mpMRI) aids the clinicians in identifying the biopsy sites and offers a non-invasive way of staging the disease and monitoring its progression. Given the clinically verified usefulness of prostate MRI on the current clinical systems, it is logical to ask if further benefits can be extracted by exploring prostate imaging on ultra-high-field (UHF) scanners. UHF systems boast main magnetic field strengths of $\geq$ 7T and offer a much higher potential signal-to-noise ratio (SNR). The additional SNR can be traded for higher resolution anatomical images or faster acquisition times compared to the lower field strength scanners. Realising the SNR gain of higher field systems, however, requires an appropriately designed radiofrequency (RF) coil. A well-built MR body coil is the necessary precursor for an objective assessment of the clinical diagnostic utility of the higher field systems in the context of prostate imaging. The project sought to develop a coil for prostate imaging at 7T. As part of the project, multiple loop coil configurations were simulated and compared. A six-channel transmit-receive design was constructed, characterised and approved for use in healthy volunteers. Preliminary volunteer T_2 and diffusion-weighted images were acquired, demonstrating promising results.

Chapter 1

Introduction

Magnetic resonance imaging (MRI) is a non-invasive imaging technique that utilises the phenomenon of nuclear magnetic resonance (NMR) to extract a wide array of clinical diagnostic data, ranging from detailed structural images of the anatomy of interest, to its metabolite spectra and other physiological data. MRI does not use ionising radiation, making it a comparatively safe imaging modality for both patients and clinical staff. MRI's versatility saw to its routine application in every anatomical region and organ, including the prostate.

The prostate gland is an important part of the male reproductive system. Its secretions form part of the seminal fluid. The organ is situated directly beneath the bladder, surrounding the urethra, and in an average healthy individual is approximately 25 ml in volume[1]. Prostate pathologies, including the prostate cancer (PC), typically result in lower urinary tract symptoms (abnormalities in passing urine). Prostate cancer (PC) is the most prevalent type of cancer amongst men in the UK and globally[2, 3]. Nevertheless, it is not uncommon for the disease to reside in an indolent state[4] that does not require radical clinical intervention that involves prostatectomy, chemotherapy, radiotherapy or their combinations. A typical prostate referral process begins with a rectal prostate examination, followed by a prostate specific antigen (PSA) test and a biopsy in case of a suspicious finding. Not only does the biopsy bear risks of side effects shared by all surgical procedures, a lack of prior knowledge about the potential cancer's localisation may result in a false negative. Having the ability to reliably and non-invasively differentiate between different forms of the disease to veer the treatment plan is of great benefit to everyone involved: from patients with an indolent PC that are spared from debilitating side effects of radical treatment, to healthcare services that avoided unnecessary time, material and human resource expenditures, and to patients with an aggressive form of the disease, to whom the freed up resources can now be allocated to facilitate a better treatment outcome.

Prostate MRI using contemporary clinical 1.5 and 3T systems has proven to be a valuable tool in prostate cancer management[4], aiding the clinicians in identifying the biopsy sites

and determining if the biopsy is needed in the first place, and offering a non-invasive way of staging the disease and monitoring its progression. A multi-parametric MRI (mpMRI) examination employed for prostate assessment comprises T_1- and T_2-weighted anatomical imaging of the prostate and its surroundings, along with diffusion weighted (DWI) and dynamic contrast enhanced (DCE) scans to infer finer structures such as degree of vascularisation[4, 5]. The procured mpMRI data is then given a radiological assessment following Prostate Imaging - Reporting and Data System (PI-RADS) guidelines[6] to derive a score that determines further course of action.

Given the clinically verified usefulness of prostate MRI on current 1.5 and 3T clinical systems, it is logical to ask if further benefits can be extracted by exploring prostate imaging on ultra-high-field (UHF) scanners. UHF systems boast main magnetic field strengths of $\geq$ 7T and offer a much higher potential signal-to-noise ratio (SNR)[7]. The additional SNR can be traded for higher resolution anatomical images or faster acquisition times compared to the lower field strength scanners. The potential to reduce the acquisition times can be of great benefit in DWI and DCE. Realising the SNR gain of higher field systems, however, requires an appropriately designed radio frequency (RF) coil. A well-built MR body coil is the necessary precursor for an objective assessment of the clinical diagnostic utility of the higher field systems in the context of prostate imaging.

RF coils constitute one of the key components of an MRI experiment, responsible for perturbing an ensemble of spins within a strong static magnetic field away from the equilibrium, and required for subsequent capture of the free induction decay signal arising as a result of the system returning to its ground state. An appropriately designed coil must provide good SNR and a sufficient spin excitation efficiency within the target anatomy, whilst simultaneously minimising the tissue heating. Heating is the principal safety concern of the non-ionising electromagnetic radiation (EM), caused by the resistive and dielectric losses from the interaction of the electric field component of the EM wave with the tissue's free (ions) and bound charges (polar molecules). The increased SNR offered by the UHF imaging systems, and the correspondingly higher Larmor frequencies required to produce an excitation, have a number of implications for the body coil design for the field strengths of 7T and above. The shortened excitation wavelengths, that are now smaller than the dimensions of the abdomen cross-section, lead to a formation of standing wave patterns, resulting in an inhomogeneous RF excitation within the anatomy of interest and poor image quality[8]. The increased tissue heating further compromises the patient safety, and an inhomogeneous electric field distribution leads to a formation of localised hotspots that cannot be measured directly. The prostate gland's focal localisation within the pelvis, coupled with the abdomen's lack of rotational symmetry, make producing sufficient excitation without inducing a lot of heating challenging. One way of addressing the problems of RF inhomogeneity and increased tissue heating in UHF MRI is through the use of parallel transmission (pTx)[9, 10, 11], which is a paradigm that uses multiple individually-powered transmit channels to drive the coil elements in order

to produce the desired RF field or flip angle (FA) distributions, by static of dynamic RF shimming.

The use of dipole and its variations as an elementary unit for the multi-channel body arrays has become a standard in 7T body imaging, owing to their ease of manufacturing and the reported favourable transmit performance at depth compared to the loops[12, 13, 14, 15, 16]. Dipole arrays have been shown to induce minimal tissue heating, whilst exhibiting increased central SNR when receiving. At the same time, the dipoles present a disadvantage of lower tuning stability and stronger inter-element coupling, whilst lacking simple strategies to reduce the interaction, which limits the practically realisable element density, losing out on SNR. The use of loops in combination with dipoles to increase the element density has been shown to produce considerable improvements in the coil's performance compared to pure dipole arrays. The 7T body array designs that combine loops and dipoles currently boast the highest reported SAR and B_1+ performance in the context of prostate imaging[13, 15]. Nevertheless, a significant interaction remains between the dipoles and the neighbouring loops belonging to the adjacent loop-dipole pairs.

Although the dipoles seemingly superseded the loops as the coil building blocks, their continued use as receivers in hybrid arrays prompted a re-evaluation of their utility as standalone elements for 7T body imaging. The project sought to develop an MR coil for 7T prostate MRI that can be used by the on-site scientists to investigate the clinical utility of the 7T prostate MRI. A rigid coil design comprising anterior and posterior halves with a local shield was considered. Four overlapped loop configurations were simulated using Duke digital body model: featuring three rectangular loops with and without the next-neighbouring decoupling within each half, and four-channel and three-channel dual row configurations (elements within the same column were driven in-phase by a single transmit channel). Constrained optimisation was used to derive B1+ and SAR phase and amplitude RF shims. The resulting transmit (mean B1+ induced within the prostate per square root of input power) and SAR efficiencies (mean B1+ induced by the coil per square root of peak SAR induced by the coil) were used to compare the four configurations, as well as a generic eight-channel shortened dipole array. The three-loop configuration was extended into a full six-channel array comprising rigid anterior and posterior halves. The proposed six-channel loop array boasted a nominal simulated B_1+ efficiency of 0.303 $\mu\mathrm{T}/\sqrt{\mathrm{W}}$ within the prostate, and a nominal simulated SAR efficiency of 0.52 $\mu\mathrm{T}/\sqrt{\mathrm{W/kg}}$ within Duke digital body model. The simulated nominal B_1+ efficiency within Duke exceeds the simulated efficiency reported in the literature for the 8- and 10-channel dipole arrays, and matches the performance of the 16-channel combined loop and dipole array when all 16 channels are used for shimming. The SAR performance of the SAR shim of the proposed six-channel loop array matches the SAR performance of the 8-channel dipole and the 16-channel combined loop and dipole arrays (when the latter is shimmed by only adjusting the phase), whilst maintaining a higher B_1+ efficiency. The proposed array could also

retain almost all of its nominal efficiency when using a phase-only shim. The proposed six-channel transmit-receive loop array (6TxRx) was built, validated and approved for use in healthy volunteers. The preliminary T_2 TSE and DWI images were acquired. A transmit efficiency comparison was done with a commercial 8TxRx fractionated dipole array in Oxford.

The project was funded by UKRI and set up as part of the MRC DTP in precision medicine, a joint collaboration between the University of Glasgow and the University of Edinburgh. The work was carried out under the supervision of Prof. David Porter. The work was carried out within the context of a larger 7T coil-development project as part of the Living Lab research programme, funded by the UKRI Strength-in-Places scheme. The project was based on Queen Elizabeth University Hospital (QEUH) campus, home to a Siemens Magnetom Terra 7T clinical research scanner, located in the Imaging Centre of Excellence (ICE) along with Glasgow university's MR coil laboratory led by Dr. Shajan Gunamony. The project involved a collaboration with NHS Greater Glasgow and Clyde in getting the ethics and safety approvals, as well as preliminary imaging study in healthy volunteers. The project included a two months collaboration with the programme's industrial partner MR CoilTech Ltd. (Dr. Gunamony's company), during which a receive array for one of the commercial head coils was assembled and tested.

The theory part of the thesis provides an overview of the Maxwell's equations in Sec. 2.1, computational electromagnetism in Sec. 2.2, fundamentals of MRI in Sec. 2.3 and MRI coils in Sec. 2.4, and safety aspects of RF radiation in Sec. 2.5, within the context of 7T prostate coil development. Coil simulations and design approach is covered in chapter 3. The coil construction is covered in chapter 4. The coil validation procedure and results are covered in chapter 5. A transmit performance comparison with an 8TxRx commercial fractionated dipole that took place in Oxford is covered in chapter 6. The preliminary healthy volunteer images are found in chapter 7. Conclusive summary of the project and future work are provided in chapter 8. The supplemental MATLAB code and VBA scripts used for post-processing of the simulation and scanner data are enclosed in the appendices.

Chapter 2

Theory

2.1 Classical electromagnetism

2.1.1 Maxwell's equations

Classical electromagnetism[17] is an eloquent theory establishing a direct link between the phenomena of electricity and magnetism with the introduction of the concepts of electric and magnetic fields that foster the interaction between the charges. The theory is governed by a set of four coupled differential equations known as (microscopic) Maxwell's equations (2.1):

$$\nabla \cdot \vec{E} = \frac{\rho}{\epsilon_0} \tag{2.1a}$$

$$\nabla \cdot \vec{B} = 0 \tag{2.1b}$$

$$\nabla \times \vec{E} = -\frac{\partial \vec{B}}{\partial t} \tag{2.1c}$$

$$\nabla \times \vec{B} = \mu_0 \left(\vec{J} + \epsilon_0 \frac{\partial \vec{E}}{\partial t} \right) \tag{2.1d}$$

The equation (2.1a) is known as Gauss's law, and defines an electric field $\vec{E}$ as a scalar field whose intensity diminishes as a square of the distance from the charge ρ that generated it outwith an arbitrary volume enclosing ρ. The Gauss's law of magnetism (2.1a) together with the Ampere's law (2.1d) defines the magnetic field $\vec{B}$ as a curling, non-diverging field arising from the motion of charge $\vec{J}$ or a change of the electric field. Finally, the Faraday's law (2.1c) links the change in the magnetic field back to the electric field, and furthermore, gives the direction of the resulting electric field such that the induced magnetic field opposes the change, conserving the energy. The constants ϵ_0 and μ_0 are known as permittivity and permeability of free space, both serving to scale the field quantities accordingly to the unit system being used. The set of equations in (2.1) are known as microscopic equations, as they describe electromagnetism from the point of individual charges and their motion. In practice, however, dealing with such a low level of abstrac-

tion is cumbersome when fields inside the real materials are considered at supra-molecular levels, and the microscopic equations are replaced with their macroscopic versions given by (2.2)

$$\nabla \cdot \vec{D} = \rho_f \tag{2.2a}$$

$$\nabla \cdot \vec{B} = 0 \tag{2.2b}$$

$$\nabla \times \vec{E} = -\frac{\partial \vec{B}}{\partial t} \tag{2.2c}$$

$$\nabla \times \vec{H} = \left(\vec{J_f} + \frac{\partial \vec{D}}{\partial t} \right) \tag{2.2d}$$

, which introduce a displacement field $\vec{D}$ and the magnetic field $\vec{H}$ to serve as equivalents of $\vec{E}$ and $\vec{B}$ inside the materials that include within them contributions from the bound charges and currents, separating them from their free counterparts ρ_f and $\vec{J_f}$.

As the bound charges and currents are now abstracted away from, the quantities $\vec{D}$ and $\vec{H}$ are related to their counterparts $\vec{E}$ and $\vec{B}$ by (2.3), where ϵ is the absolute permittivity of the material, discussed further in subsection 2.1.2, and $\vec{M}$ is the magnetisation.

$$\vec{E} = \epsilon \vec{D} \tag{2.3a}$$

$$\vec{B} = \mu_0 (\vec{H} + \vec{M}) \tag{2.3b}$$

A profound corollary of the classical electromagnetism is the existence of the transverse electromagnetic waves: the fundamentally intertwined nature of the electric and magnetic fields enables them to propagate in space. Combining the Faraday's law with the Ampere's law whilst setting the current and charge to zero yields a wave equation in free space (2.4), with the speed of propagation given by (2.5a), the speed of light in vacuum. The wavelength λ is given by (2.5b), where f is the oscillation frequency.

$$\begin{gathered}
\nabla \times \vec{E} = \nabla \times (\nabla \times \vec{B}) = \nabla \times \left(\mu_0 \epsilon_0 \frac{\partial \vec{E}}{\partial t} \right) = \mu_0 \epsilon_0 \frac{\partial}{\partial t} \left(\nabla \times \vec{E} \right) = -\mu_0 \epsilon_0 \frac{\partial^2}{\partial t^2} \vec{B} \\
\nabla \times \vec{B} = \nabla \times (\nabla \times \vec{E}) = \nabla \times \left(-\frac{\partial \vec{B}}{\partial t} \right) = -\frac{\partial}{\partial t} \left(\nabla \times \vec{B} \right) = -\mu_0 \epsilon_0 \frac{\partial^2}{\partial t^2} \vec{E} \\
\mu_0 \epsilon_0 \frac{\partial^2}{\partial t^2} \vec{B} = \Delta \vec{B} \\
\mu_0 \epsilon_0 \frac{\partial^2}{\partial t^2} \vec{E} = \Delta \vec{E}
\end{gathered} \tag{2.4}$$

$$v = \frac{1}{\sqrt{\mu_0 \epsilon_0}} = c \tag{2.5a}$$

$$\lambda = \frac{c}{f} \tag{2.5b}$$

Whilst the orientation of the electromagnetic fields $\vec{E}$ and $\vec{B}$ is fixed to be transverse to the direction of the wave propagation (and orthogonal to relative to each other), their orientation within the transverse plane defines the wave polarisation. The polarisation can be linear, circular or elliptical. In case of a linear polarisation, the E-field direction is fixed, but its amplitude can vary with time. In a circularly polarised wave, the magnitude of the E-field is fixed and only its orientation varies with time. Elliptical polarisation represents the most general case, where both the amplitude and direction of the E-field may vary in time.

Linearly polarised waves can be expressed as a superposition of the two circularly polarised components rotating at the same rate in the opposite directions. Rotating B-fields play a crucial role in MRI[18], as they are responsible for the spin excitation and receive sensitivity patterns, discussed in detail in subsection 2.3.2. Treatment of the linear polarisation as a combination of the two circularly polarised components is also a key concept in MR quadrature coils, described briefly in subsection 2.4.1.

2.1.2 Matter description

The response of the materials to the electromagnetic fields within the classical electromagnetism is governed by their conductivity σ, permittivity ϵ and permeability μ. The quantities are macroscopic, defining the bulk behaviour of the materials without considering the underlying quantum mechanical processes responsible for their formation. The parameters can vary spatially, directionally and temporally, in which case they can be used to describe inhomogeneous, anisotropic and dispersive media. The electromagnetic properties can also be coupled to other parameters, such as the material's mechanic and thermodynamic states.

Conductivity describes the ability of the material to accommodate the motion of charge. A material with enough charge carriers that may be treated as floating almost unimpeded within it, exhibiting high conductivity as a result, is classed as a conductor. In the presence of an external static electric field, charges within the conductor eventually arrange such that the net electric field within the conductor is null. In the presence of the oscillating electromagnetic field, in addition to the motion of charge induced by the electric field, eddy currents are formed that oppose the formation of the magnetic field within the conductor. The response of the material is not instantaneous, given its finite conductivity, leading to some penetration of the oscillating EM fields into the conductor.

Permittivity describes the material's ability to polarise in response to the externally applied electric field. Materials with predominantly bound charges are known as dielectrics. In the presence of a static external electric field, the bound charges of a dielectric with permittivity ϵ are displaced to form an electric dipole, resulting in a polarisation density P and a displacement field $\vec{D}$ (2.6).

$$\vec{P} = (\epsilon - \epsilon_0)\vec{E} \implies \vec{D} = \epsilon_0\vec{E} + \vec{P} = \epsilon_0\vec{E} + (\epsilon - \epsilon_0)\vec{E} = \epsilon\vec{E} \tag{2.6}$$

The polarisation does not occur instantaneously, exhibiting a hysteresis when the changing fields are considered, making permittivity a dispersive property. Furthermore, real dielectrics are lossy and dissipate part of the electromagnetic energy as heat. The permittivity is therefore generally treated as a complex, (angular) frequency-dependent quantity (2.7), with ϵ' denoting the real part and $i\epsilon''$ corresponding to a dielectric loss, indistinguishable from the resistive losses due to σ. The ratio (2.8) is known as the loss tangent.

$$\epsilon = \epsilon' + i\epsilon'' = \epsilon' + i\frac{\sigma}{\omega\epsilon_0} \tag{2.7}$$

$$\tan\delta = \frac{\epsilon''}{\epsilon'} \tag{2.8}$$

Numerous models exist that can be fitted to the permittivity measurements acquired at key frequency points to produce a broad spectrum characterisation of relative permittivity ϵ_r. Examples include a first-order Debye relaxation model (2.9a) and its generalisation known as Cole-Cole model (2.9b)[19, 20]. The latter is used for modelling the biological tissue, which acts as lossy dielectrics[21, 19]. The ϵ_∞ and ϵ_s correspond to the high frequency and low frequency (static) complex permittivity measurements, τ is the dielectric relaxation time constant and α is a parameter controlling the spectrum stretch.

$$\epsilon_r(\omega) = \epsilon_\infty + \frac{\epsilon_s - \epsilon_\infty}{1 + i\omega\tau} \tag{2.9a}$$

$$\epsilon_r(\omega) = \epsilon_\infty + \frac{\epsilon_s - \epsilon_\infty}{1 + (i\omega\tau)^{1-\alpha}} \tag{2.9b}$$

Accurate description of the biological tissue frequency response is crucial for the RF safety assessment, as the EM energy deposition rate is proportional to the conductivity. The real part of the tissue permittivity tends to decrease with frequency, whilst the conductivity increases[22]. The increased conductivity results in a higher RF energy deposition rate within the tissue, as well as a decrease in the penetration depth. Both aspects pose a challenge for UHF MRI, as the former compromises the patient safety and the latter makes achieving sufficient MR excitation in deep-seated organs such as the prostate difficult. The RF safety is discussed in further detail in Sec. 2.5.

The wavelength within a media is given by (2.10), where λ_0 is the wavelength in vacuum, and ϵ' and μ' are the real parts of the complex permittivity and permeability. At 297.2 MHz, corresponding to the Larmor frequency at 7 T, the wavelength within the abdomen is in the 13-17 cm range. The change in the propagation velocity at the air-tissue interface leads to partial reflection and refraction.

$$\lambda = \frac{\lambda_0}{\sqrt{\mu'\epsilon'}} \tag{2.10}$$

A complex relative permeability μ is defined in a similar fashion to the complex permittivity (2.11), with magnetic hysteresis replacing the dielectric relaxation. However, as human tissue is non-magnetic ($\mu = 1$), further discussion of the permeability in the context of MRI is omitted.

$$\mu = \mu' + i\mu'' \tag{2.11}$$

2.2 Computational electromagnetism

2.2.1 Overview

The numerical methods for solving the EM problems can be broadly categorised into time and frequency domain methods. The time domain method analyses the problem by propagating a wideband excitation in time, capturing the system's wideband response in a single simulation, whilst the frequency domain methods focus on a single frequency, making the problems amenable to re-casting into a system of linear equations. The need to discretise time in addition to space within the time domain methods introduces an additional source of error compared to the frequency domain methods. The numerical simulations for the project were performed using a time domain solver provided by a commercial software CST Studio Suite, which implements a finite integration technique (FIT) approach for solving the Maxwell's equations on a discrete, orthogonal hexahedral grid[20, 23, 24, 25]. The software further extends the technique with a proprietary Perfect Boundary Approximation (PBA) and Thin Sheet Approximation (TST) algorithms for a more accurate handling of the curved or non-orthogonal (relative to the discretisation grid) geometries[20].

2.2.2 Finite integration technique

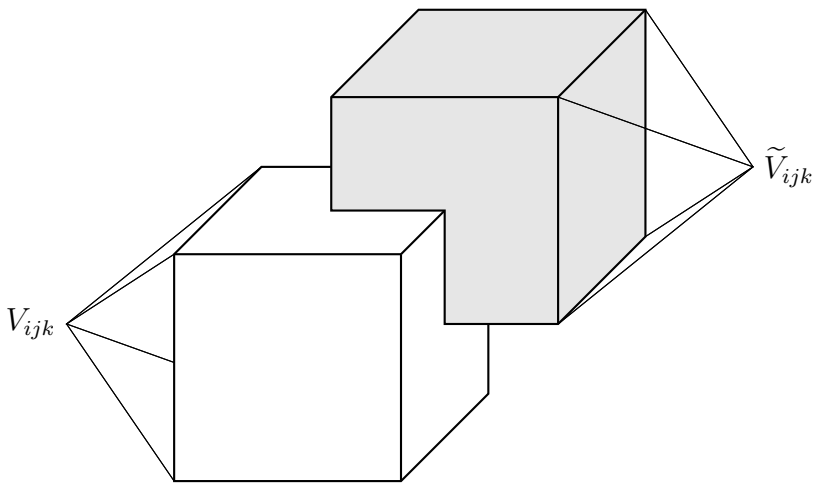

Figure 2.1: A primary cell V_{ijk} along with its dual $\widetilde{V}_{ijk}$.

The finite integration technique (FIT)[23, 24] is a numerical method for solving electromagnetic field problems in a three-dimensional space. The approach first discretises the

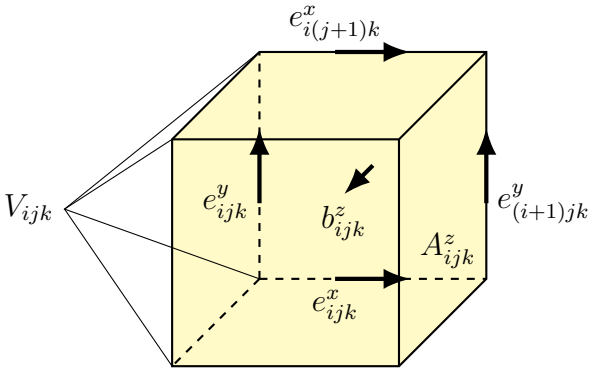

Figure 2.2: Hexahedral cell V_{ijk} along with the electric voltages e necessary to compute the magnetic flux b^z_{ijk} through a facet A^z_{ijk}.

simply connected computational region $\Omega \subseteq \mathbb{R}^3$ into a finite $(I-1)\times(J-1)\times(K-1)$ set of oriented hexahedral cells V_{ijk} to form a primary cell complex G described by (2.12) in a Cartesian coordinate system. A second, dual grid $\widetilde{G}$ with the same number of elements is then defined with its cells $\widetilde{V}_{ijk}$ originating from the centres of their respective primary cells in G as depicted in Fig. 2.1.

$$\begin{aligned} G \coloneqq \{V_{ijk} \in \Omega \mid [x_i, x_{i+1}] \times [y_j, y_{j+1}] \times [z_k, z_{k+1}]\,, \\ i = \{1, \ldots, I-1\}\,, j = \{1, \ldots, J-1\}\,, k = \{1, \ldots, K-1\}\} \end{aligned} \tag{2.12}$$

The first set of Maxwell's integral equations comprising the Faraday's law of induction (2.13a) and the Gauss's law for magnetism (2.13b) are defined for the orthogonal facets of the cells within the primary complex G.

$$\oint_{\partial A} \vec{E} \cdot \mathrm{d}\vec{s} = -\iint_A \frac{\partial}{\partial t}\vec{B} \cdot \mathrm{d}\vec{A} \tag{2.13a}$$

$$\oiint_{\partial V} \vec{B} \cdot \mathrm{d}\vec{A} = 0 \tag{2.13b}$$

Given a diagram Fig. 2.2 depicting a primary hexahedral cell V_{ijk}, the Faraday's law for its facet A^z_{ijk} is re-written as (2.14), where the closed line integral on the left-hand side of the (2.13a) is substituted with a summation of the electric voltages $e^{x,y,-x,-y}$ along the edges of the facet, and b^z_{ijk} defines the respective magnetic flux. The procedure is repeated for the remaining two orthogonal faces A^x_{ijk} and A^y_{ijk}.

$$e^x_{ijk} + e^y_{(i+1)jk} - e^x_{i(j+1)k} - e^y_{ijk} = -\frac{\mathrm{d}}{\mathrm{d}t} b^z_{ijk} \tag{2.14}$$

Given the $(I-1)\times(J-1)\times(K-1)$ number of cells, the total number of mesh points and the adjacent faces is $N_p = I \times J \times K$. The three-dimensional array of points can be represented as a vector by enforcing an order, such as sorting the points according to their position along the z-, then y- and lastly x-axes. Each mesh point n has associated with it a triplet (e^x_n, e^y_n, e^z_n) of the electric voltages and a triplet (b^x_n, b^y_n, b^z_n) of the magnetic fluxes. Then the vectors $\mathbf{e}$ and $\mathbf{b}$ can be constructed according to (2.15), encompassing

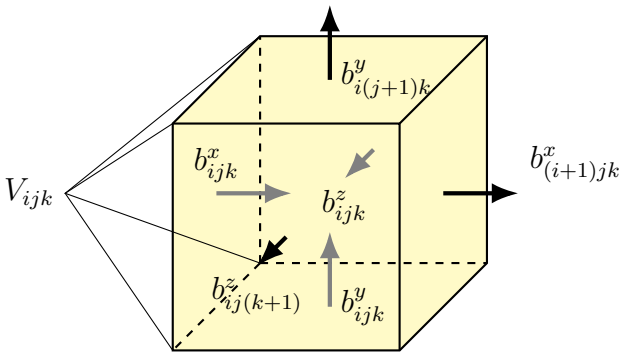

Figure 2.3: Magnetic fluxes through the facets of the primary cell V_{ijk} used to define the Gauss's law of magnetism.

all the electric voltages and the magnetic fluxes defined on G, respectively.

$$\mathbf{e} \coloneqq \left\{ (\boldsymbol{e}_1 \cdots \boldsymbol{e}_{N_p})^T \in \mathbb{R}^{3N_p} \mid \boldsymbol{e}_{n\in\{1,\dots,N_p\}} = (e^x_n \quad e^y_n \quad e^z_n) \right\} \tag{2.15a}$$

$$\mathbf{b} \coloneqq \left\{ (\boldsymbol{b}_1 \cdots \boldsymbol{b}_{N_p})^T \in \mathbb{R}^{3N_p} \mid \boldsymbol{b}_{n\in\{1,\dots,N_p\}} = (b^x_n \quad b^y_n \quad b^z_n) \right\} \tag{2.15b}$$

The two quantities can be related via a sign matrix $\mathbf{C} \in \{-1, 0, 1\}^{3N_p \times 3N_p}$, which encodes the cell orientation direction and the ordering scheme to "select" the correct combination (and orientation) of the electric voltages to compute the corresponding magnetic flux, yielding a matrix form of the Faraday's law given by (2.16). The matrix $\mathbf{C}$ represents a discrete curl operator.

$$\underbrace{\begin{pmatrix} & \cdots & \cdots & \cdots & & \\ 1 & \cdots & 1 & \cdots & -1 & \cdots & -1 \\ & \cdots & \cdots & \cdots & & \end{pmatrix}}_{\mathbf{C}} \cdot \underbrace{\begin{pmatrix} e_{n_1} \\ \vdots \\ e_{n_2} \\ \vdots \\ e_{n_3} \\ \vdots \\ e_{n_4} \end{pmatrix}}_{\mathbf{e}} = -\frac{\mathrm{d}}{\mathrm{d}t} \underbrace{\begin{pmatrix} \vdots \\ b_n \\ \vdots \end{pmatrix}}_{\mathbf{b}} \tag{2.16a}$$

$$\mathbf{C}\mathbf{e} = -\frac{\mathrm{d}}{\mathrm{d}t}\mathbf{b} \tag{2.16b}$$

The total magnetic flux through the surface enclosing the cell V_{ijk} can be represented as a sum of the magnetic fluxes through all its facets as shown in Fig. 2.3, which according to the Gauss's law of magnetism must equate to zero, giving rise to the expression (2.17), which similarly to the Faraday's law can be re-cast into the matrix notation (2.18), where $\mathbf{S} \in \{-1, 0, 1\}^{N_p \times 3N_p}$ represents a discrete divergence operator.

$$-b^x_{ijk} + b^x_{(i+1)jk} - b^y_{ijk} + b^y_{i(j+1)k} - b^z_{ijk} + b^z_{ij(k+1)} = 0 \tag{2.17}$$

$$\underbrace{\begin{pmatrix} & \cdots & \cdots & \cdots & & & & \\ \cdots & -1 & 1 & -1 & 1 & -1 & 1 & \cdots \\ & \cdots & \cdots & \cdots & & & & \end{pmatrix}}_{\mathbf{S}} \cdot \underbrace{\begin{pmatrix} \vdots \\ b_{n_1} \\ b_{n_2} \\ b_{n_3} \\ b_{n_4} \\ b_{n_5} \\ b_{n_6} \\ \vdots \end{pmatrix}}_{\mathbf{b}} = 0 \tag{2.18a}$$

$$\mathbf{Sb} = 0 \tag{2.18b}$$

The second set of Maxwell's integral equations comprising the Ampere's law (2.19a) and the Gauss's law (2.19b) are defined for the orthogonal facets of the cells within the dual complex $\widetilde{G}$ as shown in *Fig.* .

$$\oint_{\partial A} \vec{H} \cdot \mathrm{d}\vec{s} = \iint_{A} \left(\frac{\partial}{\partial t} \vec{D} + \vec{J} \right) \cdot \mathrm{d}\vec{A} \tag{2.19a}$$

$$\oiint_{\partial V} \vec{D} \cdot \mathrm{d}\vec{A} = \frac{1}{\epsilon_0} \iiint_{V} \rho \mathrm{d}V \tag{2.19b}$$

The Ampere's law is discretised in a similar manner to the Faraday's law, with the magnetomotive force $\mathbf{h}$ replacing the electric voltages along the edges of the facet, and the conductive current $\mathbf{j}$ and the displacement flux $\mathbf{d}$ replacing the magnetic fluxes, resulting in an expression (2.20), with $\widetilde{\mathbf{C}}$ defining a discrete curl operator on the dual grid $\widetilde{G}$.

$$\widetilde{\mathbf{C}}\mathbf{h} = \frac{\mathrm{d}}{\mathrm{d}t}\mathbf{d} + \mathbf{j} \tag{2.20}$$

The discrete Gauss's law is defined according to (2.21), where $\mathbf{d}$ is a displacement flux through each facet, q is a free charge enclosed within the volume of the cell $\widetilde{V}_{ijk}$ and $\widetilde{\mathbf{S}}$ is a discrete divergence operator on the dual grid $\widetilde{G}$.

$$\widetilde{\mathbf{S}}\mathbf{d} = q \tag{2.21}$$

The four matrix equations given by (2.16), (2.18), (2.20) and (2.21) constitute Maxwell's grid equations (MGEs) ((2.22)) that represent an exact formulation of the classic laws of electromagnetism computed on a grid, with no error being introduced so far as a result of discretisation.

$$\begin{aligned} \mathbf{Ce} &= -\frac{\mathrm{d}}{\mathrm{d}t}\mathbf{b}, \quad \mathbf{Sb} = 0 \\ \widetilde{\mathbf{C}}\mathbf{h} &= \frac{\mathrm{d}}{\mathrm{d}t}\mathbf{d} + \mathbf{j}, \quad \widetilde{\mathbf{S}}\mathbf{d} = q \end{aligned} \tag{2.22}$$

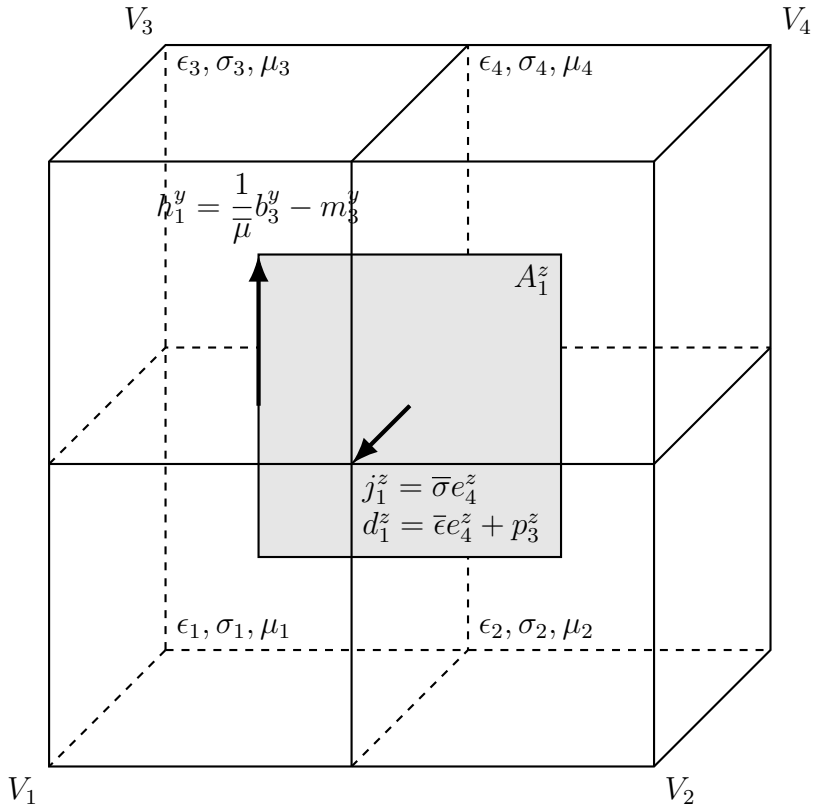

Figure 2.4: Primary cells $V_{1,2,3,4}$, whose permittivities, conductivities and reluctivities are used to compute their respective averages $\overline{\epsilon}$, $\overline{\sigma}$ and $\overline{\mu}$ that are used to establish the relationship between the quantities defined on the primary (b, e) and the dual (h, d) grids.

The first fundamental source of error of the FIT is the spatial discretisation of the simulated object geometries, whose electromagnetic properties are necessary to establish a relationship between the quantities defined on the primary and dual grids as described by (2.23), where $\mathbf{M}_\epsilon, \mathbf{M}_\sigma, \mathbf{M}_\nu \in \mathbb{R}^{3N_p \times 3N_p}$ are the matrices of the averaged permittivities, conductivities and reluctivities, and $\mathbf{p}, \mathbf{m} \in \mathbb{R}^{3N_p}$ are the permanent material polarisation and magnetisation, respectively.

$$\mathbf{d} = \mathbf{M}_\epsilon \mathbf{e} + \mathbf{p}, \quad \mathbf{j} = \mathbf{M}_\sigma \mathbf{e}, \quad \mathbf{h} = \mathbf{M}_\nu \mathbf{b} - \mathbf{m} \tag{2.23}$$

The discretisation of the material properties is performed along the primary grid G. Since the equations within the same grid complex are coupled using the quantities defined only on the cell's face (flux through the facet is defined only in terms of the voltages along its edges), the dual cell vectors $\mathbf{d}, \mathbf{h}$ can be related to their respective primary cell quantities $\mathbf{e}, \mathbf{b}$ via the averaged electromagnetic properties $\overline{\epsilon}$, $\overline{\sigma}$, $\overline{\mu}$ of the four primary cells encasing the dual facet in question, as illustrated in Fig. 2.4 for the facet $\widetilde{A}_1^z$. The MGEs described above do not take into account the dispersive properties of the materials and require an alteration to account for the hysteresis exhibited by the electromagnetic fields within most real dielectrics[26]. Within the context of MRI RF coil simulations, however, the dispersive behaviour of the materials can be ignored due to a narrowband nature of the excitation pulse.

The fields are propagated in time using a leap-frog integration scheme as described by (2.24) that replaces the partial derivatives with central differences and computes the electric and magnetic fields at different time steps[20].

$$\begin{aligned} \mathbf{e}^{n+1/2} &= \mathbf{e}^{n-1/2} + \Delta t \mathbf{M}_{\epsilon}^{-1} \lfloor \widetilde{\mathbf{C}} \mathbf{M}_{\mu}^{-1} \mathbf{b}^{n} + \mathbf{j}^{n} \rfloor \\ \mathbf{b}^{n+1} &= \mathbf{b}^{n} - \Delta t \mathbf{C} \mathbf{e}^{n+1/2} \end{aligned} \tag{2.24}$$

The scheme's convergence condition is given by the Courant-Friedrichs-Levy (CFL) criterion described by (2.25) for every mesh cell. The criterion demands that the simulation time step is chosen such that the propagation of the EM interaction (which occurs with the speed $1/\sqrt{\mu\epsilon}$) does not lead to cells being skipped.

$$\Delta t \leq \sqrt{\frac{\epsilon\mu}{\left(\frac{1}{\Delta x}\right)^2 + \left(\frac{1}{\Delta y}\right)^2 + \left(\frac{1}{\Delta z}\right)^2}} \tag{2.25}$$

2.2.3 Boundary conditions

Due to a finite representation of the EM problem within the computer memory a boundary condition must be imposed. The choice of boundary condition is entirely dependent on the problem at hand, but the four commonly used boundary conditions are electric, magnetic, open and periodic. An electric boundary condition represents an ideal conductor, and forces the tangential components of the electric field and the normal magnetic flux component to zero. A magnetic boundary condition nulls the tangential magnetic fields and normal electric fluxes. An open boundary condition is an umbrella term encompassing a variety of techniques that seek to mimic an open space by absorbing the incident wave. Amongst such techniques is a perfectly matched layer (PML) – an artificial construct that acts as a near-perfect, almost reflectionless absorber, discussed in more detail in the subsequent section. A periodic boundary condition approximates an infinitely large array, mapping one side of the boundary along a chosen direction to its opposite counterpart.

2.2.4 Perfectly matched layer

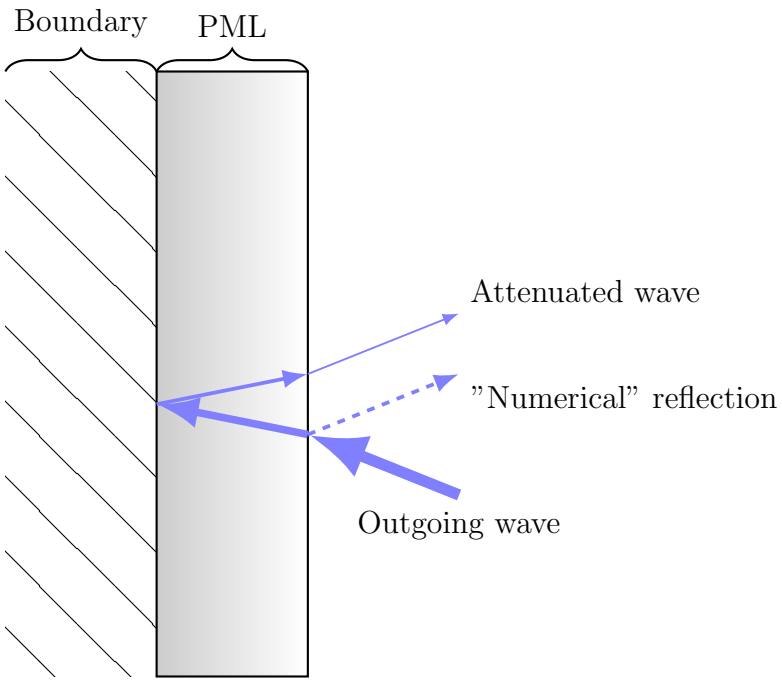

Figure 2.5: Illustration of the PML's basic operating principle: an outgoing wave from within the computational domain strikes the PML boundary at some angle, experiencing a small amount of reflection due to a wave equation discretisation and proceeds to be damped before reflecting from the computational domain's boundary back into the PML and experiencing another round of damping, emerging back within the domain of interest sufficiently attenuated. The detailed implementations vary, ranging from defining a PML as an anisotropic material with appropriately chosen ϵ and μ for a given direction (uniaxial PML[27]) within the existing material discretisation framework, requiring no alterations to the Maxwell's equations, to analytic continuation of the Maxwell's equations that directly incorporate a damping factor which is zero everywhere but within the PML[28, 29, 30].

Truncation of the computational domain necessitated by the finite amount of memory required to represent an open boundary EM problem results in reflections arising at the domain's boundary that skew the intended solution. The issue can be remediated by cladding the computational region with a perfectly matched layer (PML), which is an artificial construct exhibiting a (near) non-reflective, near-perfect EM absorption[31]. PML's operating principle is illustrated in Fig. 2.5: an incident EM wave enters the PML with some reflection arising from the discretisation of the EM problem and starts being damped, and upon reaching the back wall of the PML is reflected back owing to the boundary condition, experiencing another round of damping before emerging again within the domain of interest. Given a proper choice of the PML thickness, the appropriate damping rate increase throughout it, and the size of the computational volume the PML encases, it is possible to ensure the initial reflection and the subsequent damping is sufficient for the re-emerged wave to have a negligible effect on the expected solution.
Since its original conception by Beringer in the form currently known as split PML[32], numerous implementations of the PML have been developed[28, 27, 29, 30], with con-

volutional PML (CPML)[30] being the current state-of-the-art approach for realising the absorbing boundary condition in the time domain computations. The method builds upon the stretched coordinate formalism, which achieves the reflectionless absorption of the incoming waves by means of analytic continuation of the Maxwell's equations[28, 29].

2.3 Magnetic resonance

2.3.1 Nuclear magnetic resonance

Magnetic resonance is a quantum mechanical phenomenon describing the cycling between the energy states (ground and excited) of a magnetic dipole irradiated by an electromagnetic wave at a specific (Larmor) frequency in the presence of an external magnetic field[33, 34]. Suspension of a magnetic dipole within a static magnetic field creates a two-level system through the Zeeman effect[35]. The cyclic transition between the two quantum states of such a system influenced by an external oscillating electromagnetic field is then described by a Rabi cycle. The transition (Rabi) frequency will depend on the amplitude of the excitation field and can also occur off-resonance, but the probability of the event is greatly diminished the further away the excitation frequency is from the Larmor frequency,

$$\omega = \gamma B_0 \tag{2.26}$$

, where B_0 is the magnitude of the external static magnetic field and γ is the gyromagnetic ratio, describing the ratio of the magnetic dipole moment to the angular momentum. Larmor frequency thus reflects the energy separation between the excited and ground states and defines the energy of a photon necessary to maximise the state transition probability. The atomic nuclei with an odd number of nucleons possess a non-zero spin, imparting to them an intrinsic magnetic dipole moment and making such nuclei susceptible to the magnetic resonance phenomenon, leading to a special case of nuclear magnetic resonance which forms the basis of the magnetic resonance imaging.

2.3.2 Magnetic resonance imaging

Magnetic resonance imaging (MRI)[36] is a technique for capturing and processing a signal (known as free induction decay or FID signal) induced in the RF receiver as a result of the nuclei transition back to the ground state following a magnetic resonance excitation. Any atomic nuclei with an odd number of either of the nucleons comprising it can be used to form an MR signal with the resulting signal intensity being proportional to their gyromagnetic ratio. Abundance of the imaged nucleus within the sample of interest is of another practical consideration, as the total signal intensity will also depend linearly on the number of nuclei contributing to signal formation. Conveniently, a protium (^1H) nucleus (comprising a single proton) is one of the most abundant nuclei within the human body as it is a constituent of water and most organic compounds found in every tissue

type, whilst simultaneously possessing the second highest (only surpassed by a nucleus of its isotope tritium) gyromagnetic ratio. For these reasons, proton imaging forms the basis of most clinical MR examinations. Other candidate nuclei for clinical MR (colloquially dubbed x-nuclei) include ^{13}C, ^{31}P, ^{19}F, ^{19}Na[37].

$$\Delta E = \gamma h B_0 \tag{2.27}$$

Magnitude of the static magnetic field B_0 affects the MR signal intensity in two ways. Since the oscillation frequency is proportional to B_0, the energy of the photon is likewise proportional to B_0. The second contribution due to the B_0 comes from its effect on the fraction of the spins contributing to the signal formation. The energy difference between the ground and excited states produced by the Zeeman splitting at the fields typically employed in human imaging are modest compared to the average kinetic energy of the nuclei at body temperature, meaning that some nuclei will be constantly undergoing an energy state transition without the EM excitation, creating noise. Abstracting away from the microscopic world of atoms and molecules, and prolonging the observation timescales, the energy states of the system in question at any practically relevant instance of time within the context of MRI will obey the Boltzmann distribution (2.28), where N^+ and N^- are the numbers of spins aligned parallel and anti-parallel to the external static magnetic field B_0, T is the sample temperature and δE is the energy difference due to the Zeeman splitting, given by (2.27), where h is Planck's constant and γ is the gyromagnetic ratio of the nucleus being examined. At a body temperature and in the presence of the commonly employed B_0 field magnitudes, the number of nuclei occupying the ground and excited states will thus be roughly equal, with a very small preference given to the ground (parallel-aligned) state. This small excess in the number of parallel-aligned spins is what ends up contributing to the MR signal.

The B_0-aligned component μ_z of the magnetic moment of the nucleus is given by (2.29), where m is the magnetic spin quantum number. The net magnetisation M_0 is given by the sum of μ_z from the excess of parallel-aligned spins within the sample (2.30).

$$\frac{N^-}{N^+} = e^{-\frac{\Delta E}{kT}} \tag{2.28}$$

$$\mu_z = \hbar \gamma m \tag{2.29}$$

$$M_0 = \sum \mu_z = (N_+ - N_-)\mu_z = \frac{\hbar^2 \gamma^2 B_0 m}{2 k_b T} \tag{2.30}$$

Whilst the use of quantum mechanics is unavoidable when discussing the magnetic resonance on microscopic scales, classical electromagnetism is an adequate substitute for quantifying the phenomenon in bulk matter. Instead of dealing with individual spins, the classical description of NMR operates with a bulk magnetisation vector $\vec{M}$, corresponding to a sum of all the magnetic moments within a unit volume. At the start of the experi-

ment, the bulk magnetisation vector is aligned along the direction of the static magnetic field $\vec{B_0}$ with an angular frequency expressed by (2.26). Applying an oscillating EM field at the Larmor frequency in the direction perpendicular to $\vec{B_0}$ tips the magnetisation vector, resulting in a transverse magnetisation. Upon the cessation of the application of the external oscillating field, the magnetisation vector $\vec{M}$ returns to an equilibrium at a certain rate, emitting an EM wave of the same frequency in the process, which is then detected. The behaviour of the magnetisation vector $\vec{M}$ is described by Bloch equations (2.31)[33], which model the restoration of the system's equilibrium as a relaxation process with decay times constants T_1 and T_2, corresponding to the relaxation times of the longitudinal and transverse components of $\vec{M}$ respectively. The T_1 relaxation is associated with the exchange of energy of the excited nucleus with its surroundings (molecules), whilst T_2 relaxation, in addition to the exchange of energy with the surroundings, also arises from the nuclei in different molecules experiencing slight variations in the net static magnetic field due to the local shielding effect of the electron clouds of the molecules the nucleus resides in, leading to the nuclei precessing at slightly different frequencies, resulting in a loss of phase coherence and a reduction in the net transverse magnetisation. The T_2 relaxation can occur in the absence of T_1 relaxation in the case of a dipolar interaction of spins.

$$\begin{aligned}
\frac{dM_x}{dt} &= \gamma\left(\vec{M}\times\vec{B}\right)_x - \frac{M_x}{T_2},\\
\frac{dM_y}{dt} &= \gamma\left(\vec{M}\times\vec{B}\right)_y - \frac{M_y}{T_2},\\
\frac{dM_z}{dt} &= \gamma\left(\vec{M}\times\vec{B}\right)_z - \frac{M_z - M_0}{T_1}
\end{aligned} \tag{2.31}$$

MR excitation of spins occurs as a result of their irradiation by a rotating component of the EM field oscillating at the Larmor frequency in the transverse plane (relative to the $\vec{B_0}$ direction), denoted as $\vec{B_1}+$ and given by (2.32a). The receive sensitivity, discussed in more detail in Sec. 2.4, is determined by the component $\vec{B_1}-$ (2.32b), rotating in the opposite direction to $\vec{B_1}+$.

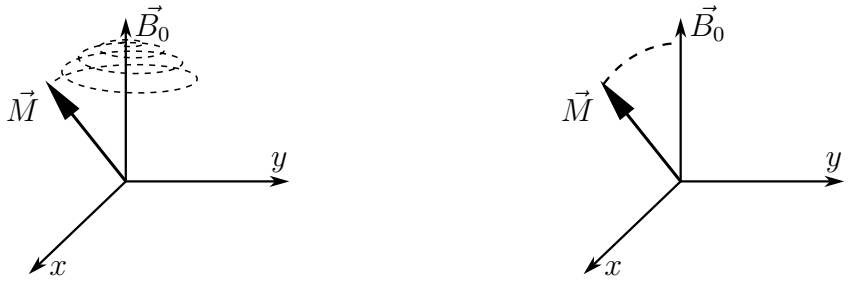

(a) Laboratory frame (b) Rotating frame

Figure 2.6: In the laboratory reference frame, $\vec{M}$ appears to precess along the direction of the $\vec{B_0}$ field when the rotating $\vec{B_1}+$ field is applied in the transverse plane. In the rotating frame, the $\vec{B_1}+$ is aligned with the x-axis, and the magnetisation vector $\vec{M}$ is simply tipped with respect to the $\vec{B_0}$ field.

The set of equations given in (2.31) described the magnetisation vector behaviour in the laboratory reference frame. However, the relaxation of the magnetisation in an MR experiment can also be described in a frame rotating at the Larmor frequency with the $\vec{B_1}+$ for convenience, in which case the Bloch equations simplify to (2.33). The graphic representation of the behaviour of $\vec{M}$ is shown in Fig. 2.6.

$$\vec{B_1}+ = \frac{B_1^x + iB_1^y}{2} \tag{2.32a}$$

$$\vec{B_1}- = \frac{(B_1^x - iB_1^y)^*}{2} \tag{2.32b}$$

$$\begin{aligned} \frac{dM_{xy}}{dt} &= -\frac{M_{xy}}{T_2}, \\ \frac{dM_z}{dt} &= \frac{M_0 - M_z}{T_1} \end{aligned} \tag{2.33}$$

When a $\vec{B_1}+$ field is applied, the magnetisation vector $\vec{M}$, initially aligned with a z-axis, is rotated into the transverse plane, resulting in a non-zero transverse magnetisation. The angle by which the magnetisation vector is rotated is known as the flip angle α, and is proportional to the duration of the application of $\vec{B_1}+$ (2.34). The $\vec{B_1}+$ itself can be time-varying.

$$\alpha = 2\pi\gamma \int_0^T tB_1(t)dt \tag{2.34}$$

2.3.3 Spatial encoding

2.3.3.1 k-Space

A spatial distribution function $I(\boldsymbol{r})$ in a three-dimensional Euclidian space has associated with it a unique reciprocal space $Q(\boldsymbol{k})$ of the same dimensionality - also known as k-space - that is a Fourier transform of $I(\boldsymbol{r})$ given by (2.35) with $\boldsymbol{k}$ a complex vector[38, 39]. The Fourier inversion theorem states that the function $I(\boldsymbol{r})$ can be recovered from its k-space via an inverse Fourier transformation given by (2.36).

$$Q(\boldsymbol{k}) = \int_V I(\boldsymbol{r}) e^{i2\pi f \boldsymbol{k}\cdot\boldsymbol{r}} d\boldsymbol{r} \tag{2.35}$$

$$I(\boldsymbol{r}) = \int_K Q(\boldsymbol{k}) e^{-i2\pi f \boldsymbol{k}\cdot\boldsymbol{r}} d\boldsymbol{k} \tag{2.36}$$

If $I(\boldsymbol{r})$ denotes a spatial signal magnitude distribution related to some quantity of interest being measured in an MR experiment at a frequency f_0, the total signal $S(t)$ observed at an instant in time is given by (2.37)[40, 41], which in Fourier analysis terms constitutes the magnitude of the zeroth order harmonic of the Fourier expansion of $I(\boldsymbol{r})$ located at the origin of its k-space.

$$S(t) = \int_V I(\boldsymbol{r}) e^{i2\pi f_0 t} d\boldsymbol{r} \tag{2.37}$$

The task of computing higher order harmonics to reconstruct $I(\boldsymbol{r})$ is equivalent to resolving the individual contributions to $S(t)$ from $I(\boldsymbol{r})$, which can be achieved by introducing a distinct phase shift to the signals emanating from each location $\boldsymbol{r}$. This can be achieved by introducing a spatial variation in the static magnetic field strength, or a gradient. If $\boldsymbol{G}(t)$ describes a gradient of the main magnetic field $\vec{B}_0$, then the instantaneous Larmor precession angular frequency $\omega(\boldsymbol{r})$ will be given by (2.38). The discrepancy between the precession angular velocities will lead to dephasing of the signal coming from $\boldsymbol{r}$, with the magnitude of dephasing given by a time integral (2.39) over a gradient application duration.

$$\omega(\boldsymbol{r}, t) = \omega_0 + \gamma \boldsymbol{G}(t) \cdot \boldsymbol{r} \tag{2.38}$$

$$\Phi(\boldsymbol{r}, t) = \gamma \int_0^t \boldsymbol{G}(t) \cdot \boldsymbol{r} dt = \boldsymbol{k}(t) \cdot \boldsymbol{r}, \text{ where } \boldsymbol{k}(t) = \gamma \int_0^t \boldsymbol{G}(t) dt \tag{2.39}$$

The total signal $S(t)$ will then be expressed as (2.40). The signal can be referenced to the central experiment frequency, further simplifying the expression by discarding the $e^{i2\pi f_0 t}$ component, yileding $S_0(t)$ given by (2.41). $S_0(t)$ modulated in this manner is thus a Fourier transform of $I(\boldsymbol{r})$ with respect to the vector $\boldsymbol{k}(t)$ describing a trajectory within the domain of spatial frequencies. The $I(\boldsymbol{r})$ itself can be recovered through an application of the inverse Fourier transform, resulting in (2.42).

$$S(t) = \int_V I(\boldsymbol{r}) e^{i2\pi[f_0 t + \Phi(\boldsymbol{r}, t)]} d\boldsymbol{r} = e^{i2\pi f_0 t} \int_V I(\boldsymbol{r}) e^{i2\pi \boldsymbol{k}(t) \cdot \boldsymbol{r}} d\boldsymbol{r} \tag{2.40}$$

$$S_0(t) = \int_V I(\boldsymbol{r}) e^{i2\pi \boldsymbol{k}(t) \cdot \boldsymbol{r}} d\boldsymbol{r} \tag{2.41}$$

$$I(\boldsymbol{r}) = \int_{-\infty}^{\infty} S_0(t) e^{-i2\pi \boldsymbol{k}(t) \cdot \boldsymbol{r}} dt \tag{2.42}$$

Accurate reconstruction of the signal distribution therefore requires an infinite observation time, or equivalently, sampling the signal from every infinitismal location in k-space, which is impossible, as not only would the trajectory $\boldsymbol{k}(t)$ have to cover the entirety of k-space, but the signal digitiser used to resolve the contents would need to posses inifinite resolution. A discrete version of the Fourier transform is therefore employed in practice to reconstruct the k-space up to a desired resolution. The k-space possesses conjugate symmetry, suggesting that it can be reconstructed accurately by mapping out at least half of it. The presence of noise, however, implies a trade-off in SNR, proportional to $\sqrt{N}$, where $N \geq 0.5$ is a fraction of the k-space that was sampled during the acquisition.

2.3.3.2 Phase encoding

Phase encoding utilises a magnetic field gradient to produce a spatially-dependent phase offset along the desired direction. The initial application of the gradient leads to a spatially-varying Larmor frequency distribution and a phase offset Φ after time t as described by (2.39). Upon the cessation of the phase encoding gradient application, the resultant dephased monofrequent signal is recorded, corresponding to a single point in k-

space. Resolving N locations within the k-space would require procuring N measurements with a different phase offset, as the task can be regarded as resolving an equation with N unknowns, which requires a system of N equations to guarantee a unique solution.
Since phase offset is cyclic, if the imaged sample stretches outside the phase encoding region, the external signal will be incorrectly interpreted as if coming from within the encoded domain, leading to a phase wrap artefact. Phase wrapping can be resolved with oversampling (extending the phase encoding region to include the outer parts of the sample).

2.3.3.3 Frequency encoding

Frequency encoding utilises a magnetic field gradient (referred to as a read out gradient) to produce a spatially-dependent Larmor frequency distribution along the chosen direction. The one-dimensional spatial distribution of the measured quantity along the gradient application direction can then be recovered using a Fourier transform. The steepness of the gradient along with the number of partition steps determines the breadth of frequency contents per partition, known as receiver bandwith.
Frequency encoding assumes an identical central Larmor frequency throughout the imaged sample, which may not hold true in practice within a heterogeneous sample containing a variety of molecules whose shielding effect can cause a wide range of Larmor frequencies to be present, leading to chemical shift artefacts. The artefact is caused by an inability to distinguish between the precession frequency offset caused by a gradient application and the offset brought upon by a chemical shift. It manifests as an offset of the chemically shifted compound along the frequency encoding direction relative to its intended position, with the magnitude of the shift being proportional to the chemical shift and inversely proportional to the receiver bandwith.

2.3.3.4 Slice-selective imaging

Slice-selective imaging seeks to discretise the three-dimensional space into a set of two-dimensional slices that can be analysed by the means of a two-dimensional Fourier transform. The partitioning of the imaged space along a specified direction is achieved by assigning to each partition a unique Larmor frequency band, which is accomplished with an application of a magnetic field gradient, leading to a spatial variation of the precession frequency given by (2.38). The desired slice can then be excited with an RF pulse containing a corresponding frequency band, whilst avoiding the excitation elsewhere. The excited slice is then subjected to phase and frequency encoding steps to recover the two-dimensional distribution of the imaged quantity.
The ideal RF pulse used to excite a slice would have a perfect rectangular response over the desired frequency range, which corresponds to a *sinc* pulse in the time domain, impossible to produce in practice. Truncating the *sinc* pulse removes the higher order oscillation in the time-domain, which produces an excitation pulse with a frequency response outside

the desired excitation band.

2.3.3.5 Volume excitation

Volume excitation tackles the three-dimensional signal localisation head on by using a frequency encoding step for one of the dimensions in a combination with two phase encoding steps for the remaing orthogonal directions. Assuming N and M are the numbers of partitions along each phase encoding direction, the total number of unknowns is $N \times M$, requiring $N \times M$ measurements to uniquelylarmour resolve the imaged quantity distribution.

2.3.4 Spin echo

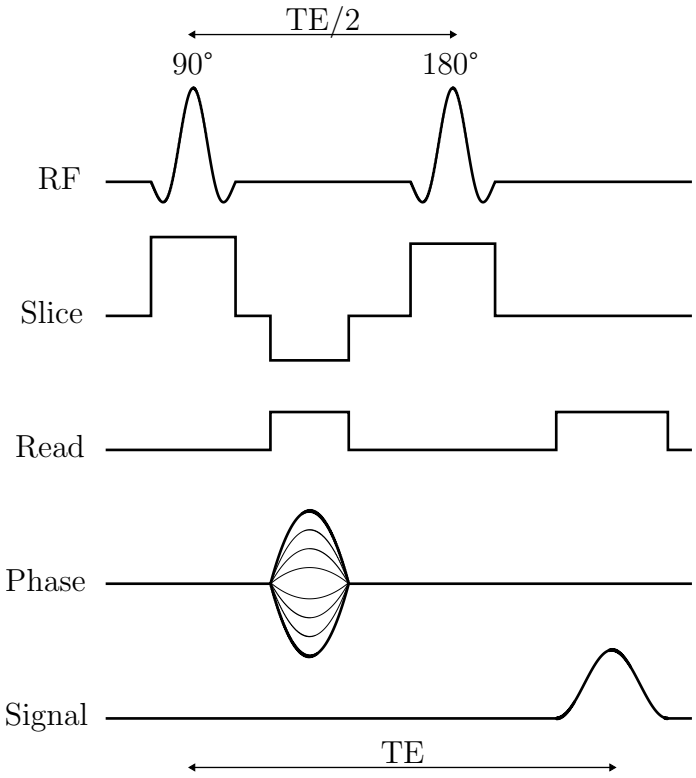

Figure 2.7: A diagram of the conventional spin echo sequence.

A spin echo (SE)[42, 43] sequence diagram is depicted in Fig. 2.7. An excitation pulse is applied, creating a transverse magnetisation. T2 relaxation (described in 2.3.2) leads to the loss of phase coherence, which is recovered after an application of the second refocusing pulse at the time TE/2. Restoration of the phase coherence leads to a formation of an echo signal at the echo time TE. After a time TR, the sequence repeats.

If slice-selective imaging is used, the excitation and refocusing pulses are played out when the slice selective gradients are active. A phase encoding gradient is applied in between the first and second excitation pulses to introduce dephasing used for spatial localisation along the gradient's application direction. The readout (frequency) gradient is played out

at TE. A turbo spin echo (TSE) sequence uses multiple refocusing pulses with varying phase encoding gradients to acquire multiple echoes within the same TR.

2.3.5 Gradient echo

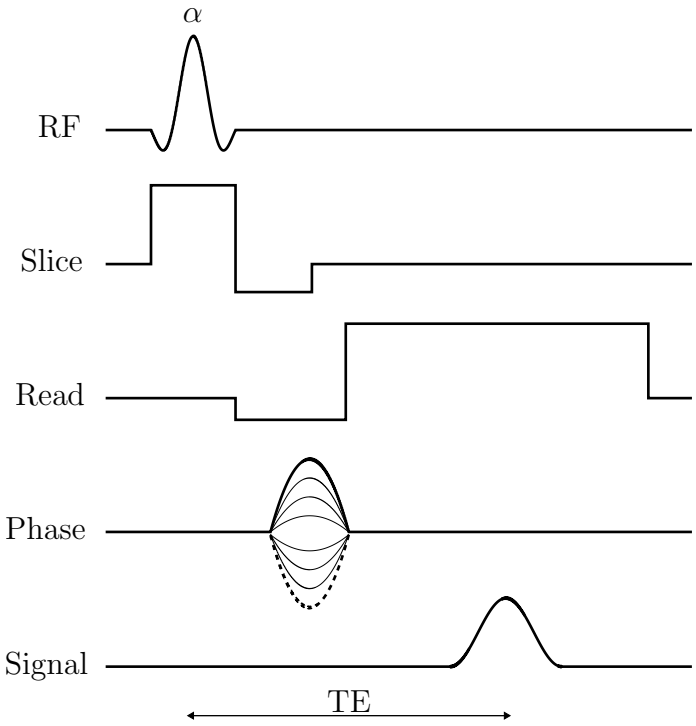

Figure 2.8: A diagram of the gradient echo sequence.

A gradient echo (GRE) sequence diagram is depicted in Fig. 2.8. An excitation pulse is followed by an application of the dephasing gradient (along the frequency encoding direction) together with the phase encoding gradient, followed by a rephase (readout) gradient with a reverse polarity to restore the phase coherence, resulting in a signal at the echo time TE.

2.3.6 Magnetic resonance signal noise

Noise is an important consideration in a MR signal analysis[8], as contributions from random, non-systematic processes do not convey meaningful information. Performance of an MRI system is therefore dependent on its signal-to-noise ratio (SNR) rather than the nominal amount of signal that can be extracted in an MR experiment. Thermal noise is the dominant dominant noise contributor in MRI, present in both the imaged sample and the hardware components, pertinent to the resistive losses within the conductors. Whilst the final SNR depends on the imaging protocol parameters as well as the choice of reconstruction algorithms, the thermal noise associated with the RF coil-sample interaction defines the maximally realisable, intrinsic SNR (ISNR), discussed in more detail in Sec. 2.4.The summary of the protocol parameters and their effect on SNR, along with a brief explanation, are presented in Table 2.1.

Parameter	Impact on SNR	Description
Voxel size	Increases with voxel size	Bigger voxels contain more spins, resulting in a higher net magnetisation available per voxel. The voxel size is determined by the field view, receiver bandwidth, number of phase encoding steps and slice thickness.
Number of excitations (NEX)	Increases with the number of excitations	Acquiring multiple images under identical conditions improves statistical confidence.
TR	Increases with TR	Increasing the TR allows the net magnetisation to return to equilibrium (co-aligned with the B_0), increasing the amount of signal available for the subsequent acquisition.
TE	Decreases with TE	Acquiring the signal before it decays significantly.
Acceleration factor	Decreases with acceleration factor	The acceleration factor is only applicable to parallel imaging. The higher the acceleration factor, the lower the SNR, as the k-space becomes more undersampled. The magnitude of the SNR penalty depends on the coil's geometry factor g, discussed in more detail in Sec. 2.4.

Table 2.1: Summary of the fundamental MR pulse sequence parameters and their effect on the resulting SNR within the image.

2.4 MRI coils

2.4.1 Overview

MRI coil is a key component of an MR experiment responsible for the spin excitation and subsequent signal MR signal reception. It is an antenna (or an array of antennas) operating in the near-field region that couples to the human body. Many different types of resonant structures are employed for this purpose, ranging from an arrangement of loops[44, 45, 46, 47, 48], dipoles[12, 49] or transmission line resonators[50, 51, 52] (and their variations and combinations[13, 15, 14, 53]) to birdcage[54] or transverse electromagnetic resonators (TEMs)[55, 56]. A coil can either be used exclusively to induce magnetisation (Tx), purely as a receiver (Rx) in conjunction with another transmitter, or combine these functions (either using the same resonant structures to transmit and receive, or having dedicated elements for each task), requiring a dedicated circuitry to switch between the two operating modes during an MR examination[57]. The coils vary in the number of channels they can accommodate. Transmission coils used in clinical ≤ 3

T scanners employ single or dual channels, whilst the Tx coils built for modern UHF systems (main magnetic field strengths ≥ 7 T) can use as many as 16 channels (but with 8 currently being the standard) to accommodate parallel transmission used to address the excitation inhomogeneity at higher field strengths. Dedicated multi-channel receive arrays employ the receive elements' spatial localisation (and thus their unique sensitivity profiles) as an additional source of information to increase SNR and minimise the SNR penalty when used in conjunction with parallel imaging (PI)[58].

A coil can either be a general purpose volume array (as is typical of lower B_0 field systems) or made exclusively for applications within a specific anatomic region (such as elbow, knee, abdomen, chest, head etc.). Whilst ^1H imaging is the primary nucleus used in human MRI owing to its abundance within the body and a high gyromagnetic ratio, the interest in functional imaging using other nuclei (termed x-nuclei) is on the rise amongst the scientists and clinicians due to the introduction of the UHF systems that partly address the inherently low SNR (compared to ^1H) limitation of x-nuclei imaging modality[37]. This creates a demand for coils with multi-nuclei imaging capabilities, realised either by inciting multiple resonances within the same structure or featuring separate elements for each nucleus of interest[59, 60].

The antenna's feed is preceded by a matching network in order to minimise the reflected power. Additionally, an antenna is typically fed with a balun for stability and prevention of the radiated losses from a feed line[61]. A pre-amplifier is needed to boost the received signal, as the electromotive force (EMF) induced within the coil during an MR experiment is on the order of microvolts. For a coil element used in both transmission and reception, a transmit-receive (TR) switch is introduced to isolate the receive chain from the transmit chain during the transmission in order to safeguard the pre-amplifier: whilst the transmit voltages can reach a few hundred volts per channel, the voltage induced by the FID within the coil element during the reception is on the order of microvolts, and the low-noise pre-amplifiers available for MR applications can typically withstand between 20-30 dBm (2.2-7 V RMS at 50 Ohms) of input RF power. Dedicated receive elements feature an active detuning circuit to decouple them from the transmitted fields to protect the pre-amplifiers and maximise the coupling of the transmit elements to the imaged subject.

2.4.2 Coil performance metrics

The coil's overall performance is determined by the performance of its transmit and receive chains. By the principle of reciprocity outlined by Hoult[18], the transverse (relative to the direction of the applied main magnetic field $\vec{B_0}$) rotating components $\vec{B_1}+$ and $\vec{B_1}-$ (rotating clock-wise and counter clock-wise, respectively, assuming a right-hand co-ordinate system with respect to a positive $\vec{B_0}$ direction) of the magnetic field $\vec{B}_1$ produced by the coil and oscillating at the Larmour frequency ω are responsible, respectively, for producing the transverse magnetisation by flipping the net magnetisation vector $\vec{M}_0$ by a tip angle θ, and determine the voltage that will be induced in a coil by a magnetisation

vector returning to an equilibrium. The $\|B_1+\|$ the coil can induce per unit time is limited by the RF power supply output P_{in} weighted by the efficiency η_{B_1+} with which the coil can convert the supplied power (or the applied voltage at its input) to $\|B_1+\|$ within the region of interest, yielding (2.43) for the expression of coil B_1+ efficiency.

$$\eta_{B_1+} = \frac{\|B_1+\|}{\sqrt{P_{\text{in}}}} \tag{2.43}$$

The efficiency η_{B_1+} is fundamentally related to the coil's geometry, but in practice, when the coil is built, is also determined by the resistive, reflective and radiative losses: resistive losses arise from a finite conductivity of the conductors used in coil construction at room temperature, further exacerbated by the skin effect; reflective losses are a consequence of an impedance mismatch between the antenna and the feed line; radiative losses can arise when a balanced and unbalanced lines are interfaced (such as when feeding a loop element with a coaxial cable), leading to the feed line acting as a transmitter[61]. Additional circuitry necessary in practice (TR switch, balun) introduces its own set of resistive and mismatch losses. In arrays with many tightly-packed channels, the interaction between the array elements and the accompanying cables and circuits becomes significant, leading to a poorer transmission efficiency and skewed B_1+ profiles[62]. Given the influence of the coil's build on its realised performance, the coil's efficiency can be defined with respect to the accepted or even dissipated power within the imaged sample instead of the input power to decouple the design's fundamental, geometric contribution to B_1+ from the practicalities of the design implementation.

The existence of the electric fields alongside the magnetic fields, and the consequent resistive and dielectric losses within the biological tissue that are converted into heat compromise the imaged subject's safety. The MRI RF safety guidelines define safety limits in terms of the rate of the E-field energy deposition within the tissue per unit mass, a metric known as specific absorption rate (SAR)[63, 64], whose more detailed treatment is provided in subsection 2.5.2. At UHF frequencies, the localised SAR becomes significant. As a result, $\|B_1+\|$ produced by the coil is constrained by the peak local SAR (pSAR), providing another metric for the coil's transmit performance evaluation known as SAR efficiency η_{SAR}, which is defined as a ratio of the $\|B_1+\|$ to the square root of pSAR as given by (2.44). The square root dependence arises as a consequence of the E-field energy W being proportional to the square of its magnitude, and a linear relationship between the induced E-field and the B_1+ oscillation owing to the Faraday's law, resulting in $\text{pSAR} \propto \|B_1+\|^2$.

$$\eta_{\text{SAR}} = \frac{\|B_1+\|}{\sqrt{\text{pSAR}}} \tag{2.44}$$

The coil's receive performance can be characterised by its contribution to SNR within the context of the coil's application (imaged subject's shape and size, target anatomy, intended acceleration factor and acceleration directions). The SNR of the MR experiment depends on many factors other than the coil, such as the choice of sequence parameters

and image reconstruction algorithms, as mentioned in subsection 2.3.6. Nevertheless, it is possible to summarise the factors contributing to SNR attributed to the coil within a given experimental setup in a concept known as intrinsic SNR (ISNR) as described by (2.45)[65, 66]. The $\|B_1-\|$ introduced earlier is also known as the sensitivity profile. The expression in the quotient denotes a noise power spectral density, where k_b term is the Boltzmann constant, and $T_{c,s}$ and $R_{c,s}$ are the temperatures and the resistances of the coil and equivalent sample resistance, respectively. The significance of R_s is its indication of the degree of coupling of the coil to the sample and depends on the coil design (in addition to being related to B_0). It is similar in concept to a radiation resistance of antenna operating in the far-field region.

$$\text{ISNR} \propto \frac{\omega M_0 \|B_1-\|}{\sqrt{4k_b(T_cR_c+T_sR_s)}} \tag{2.45}$$

If the coil is used in conjunction with PI, the SNR is degraded by a square root of the acceleration factor A weighted by the coil's geometry factor g, yielding a generalised expression (2.46) for the SNR in PI[67, 68]. The g-factor is related to the sensitivity profile (B_1-) correlation between the receive array elements. The g-factor is by definition ≥ 1, with unity corresponding to completely decorrelated array element sensitivity profiles, resulting in no aliasing introduced by the image reconstruction.

$$\text{SNR}_{\text{PI}} = \frac{\text{SNR}}{g\sqrt{A}} \tag{2.46}$$

The pre-amplifier's noise figure (NF) is another factor responsible for the receive array's SNR degradation, typically on the order of 0.3-0.4 dB (relative to the SNR at the pre-amplifier input).

Another metric useful at certain coil construction stages is the quality factor Q and the ratio Q_r between the unloaded and loaded Q-factors[69]. A quality factor is a measure of how (under)dampened an oscillator is at a given frequency, or, alternatively, the system's maximal energy storage capacity relative to how much energy is dissipated per cycle of oscillation, and for an ideal RLC circuit is given by (2.47). The unloaded Q_u is a coil's Q-factor in the absence of sample loading (no series R_s is present), whilst a loaded factor Q_l is its Q-factor when the coil is loaded (with an equivalent series resistance R_s of the sample for a given coil configuration). The importance of the ratio Q_r is that it is indicative of the proportionality between R_s and R_c, providing an indirect measure of R_s and, consequently, how well the coil couples to the sample. The Q-factor can be readily measured using an overlapped pair of the coaxial H-field probes (with one probe transmitting) and calculating the ratio of the S_{21} peak to its full-width half-maximum

bandwidth (FWHMBW).

$$Q = \frac{\omega L}{R} \tag{2.47a}$$

$$Q_r = \frac{Q_u}{Q_l} = \frac{R_c + R_s}{R_c} \tag{2.47b}$$

2.4.3 Surface coils for 7T prostate imaging

Surface arrays comprising multiple resonators (ranging from eight in a typical TxRx body array to 128 receive elements within the head coils[62]) placed closely against the imaged subject have been the coils of choice for maximising the SNR within the target anatomy. Each channel's received sample noise is likewise limited to the reception pattern of the element in question, given a sufficient between-element decoupling. High channel count serves to accommodate both, a higher number of sampling locations and a possibility to cover a large surface area to provide sufficient anatomical coverage. At the same time, the amount of additional cabling and electronics, as well as increased inter-element coupling, associated with physical implementation of the high-density receive arrays, and the subsequent noise increase and skewed sensitivity profiles, lead to a more modest SNR gain than what could be theorised.

Whilst loops have served as the elements of choice for the surface body arrays at 3T, the dipole and their variations were consistently demonstrated to provide a more favourable performance to loops in the context of prostate imaging, owing to their higher receive sensitivity and a stronger induced B_1+ at depth. Whilst in isolation the dipoles produce a higher SAR compared to a loop, they have been shown to outperform the loops when arranged into an array and using a static prostate shim. Whilst offering a superior performance in the context of prostate imaging using a static shim and being easy to manufacture and implement as semi-rigid arrays, the use of dipoles faces numerous challenges. Strong inter-element coupling and a lack of efficient decoupling techniques limits the practically realisable element density, and a lower sample loading stability can lead to a significant performance variation between the subjects and various anatomical regions (if the array is to be utilised as a general purpose body array).

Currently, the highest SNR and SAR performance within the context of 7T prostate imaging is demonstrated by the arrays combining both dipoles and loops[13, 15]. The loops are introduced to counter the low realisable element density of the pure dipole arrays, as the two elements are readily decoupled by a central placement of the dipole along the loop's central axis, allowing the number of elements to be doubled, with the only significant interaction remaining between the adjacent pairs. On the transmit side, the simultaneous excitation of such a loop and dipole pair was shown to result in an increased SAR performance in comparison to a pure dipole or loop excitation. An I-MARS array introduced in 2022 by Destruel et al.[14] demonstrates an excellent sample loading stability and SAR performance, but the latter comes at a cost of a significantly

reduced transmit efficiency within the prostate.

2.4.4 Pre-amplifier decoupling

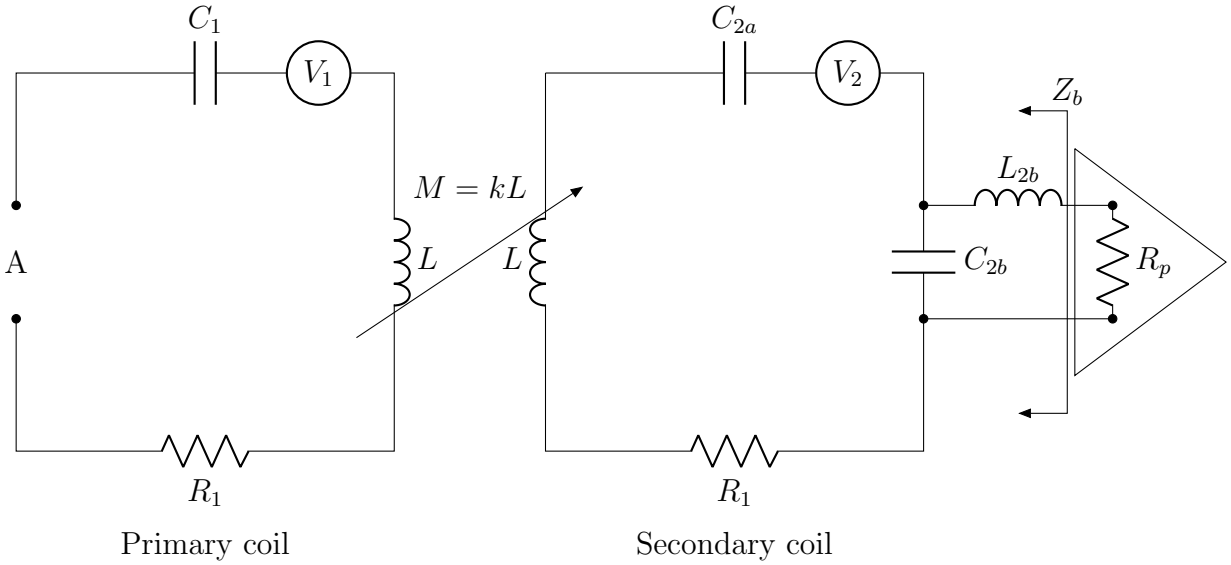

Figure 2.9: Equivalent circuit representation of a pair of receive loops in a phased array. Diagram reproduced from Roemer et al.[44]

Pre-amplifier decoupling is a technique for minimising the interaction between the elements of the loop array during the MR signal reception[44]. The decoupling is achieved by minimising the current flowing in the loop through the use of a low input impedance pre-amplifier (but noise-matched to 50 Ohms). An equivalent circuit representation of a pair of receive loops in a phased array is shown in Fig. 2.9. The impedance Z_A, as viewed from the terminal A of the primary loop, is given by (2.48), where R_p is the input impedance of the preamplifier, L is the inductance of the loops, k is the coupling coefficient, ω is the angular frequency, R_1 is the load (sample) and X_2 is the impedance of the matching circuit comprising a feed capacitor C_{2b} and an inductor L_2b. When either the coupling coefficient k or the preamplifier input impedance are null, there is no current contribution to the primary loop due to the nearby loop (and vice-versa). Pre-amplifier decoupling can be implemented in the transmit-receive elements for the receive chain.

$$Z_A = R_1 + \frac{(\omega L k)^2}{R_1 + \dfrac{X_2^2}{R_p}} \tag{2.48}$$

2.4.5 Active detuning

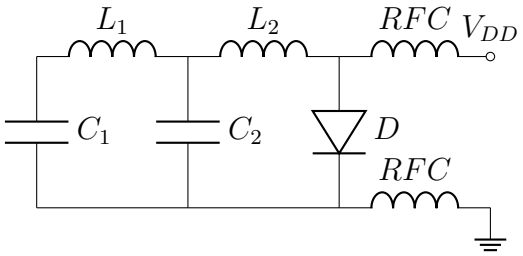

Figure 2.10: An active detuning circuit on a transmit loop.

Active detuning is used for preventing the coil elements from receiving in the coils with dedicated receive arrays. In transmit elements, active detuning is used during reception to prevent the transmit elements from coupling to the receive elements. On the receive side, active detuning is used to stop the receive elements from coupling to the transmitters during transmission and syphoning power intended from spin excitation, whilst also simultaneously protecting the pre-amplifiers. The switching between the two operating modes is realised with a PIN diode. An example implementation of the active detuning circuit on a loop transmit element is shown in Fig. 2.10. When the PIN diode is powered, the reactances X_{C_2} and X_{L_2} cancel each other out, leaving the X_{L_1} floating and the coil's tuning unchanged. When the PIN diode is unpowered (or reverse biased), the reactances X_{C_1}, X_{L_1} and X_{C_2} form a circuit, detuning the loop.

2.5 Radiofrequency safety

2.5.1 Overview

The main danger of non-ionising EM radiation associated with frequencies employed in MRI in vivo is the heating of biological tissues that can result in a local burn or disruption of its normal function.[63, 70] Heating occurs as a result of an interaction of the electric field component of the MR excitation signal with the tissue's bound (polar molecules) and free charges (ions), resulting in dielectric and resistive losses that are converted into heat. However, the actual temperature increase is determined by the RF energy deposition in conjunction with tissue's thermoregulatory response and its environment (such as ambient temperature, airflow and humidity). Whilst the extent of the tissue damage is a consequence of the temperature rise, a different metric known as specific absorption rate (SAR) is used to quantify the thermal effect of the RF exposure. SAR defines the rate of RF energy deposition within the tissue. The SAR cannot be measured directly and has to be continuously estimated from a mathematical model during a scan to ensure the regulatory limits (given by the IEC 60601-2-33 standard in the UK[63, 64]) are not exceeded. Since SAR does not take into account the heat dissipation processes occurring within the tissue, it is only crudely related to the temperature rise[71].

2.5.2 Specific absorption rate

Specific absorption rate (SAR) is a measure of RF energy deposition rate per unit mass of the tissue defined by (2.49), where W is the absorbed RF energy, m is mass, V is volume, ρ is density, σ is the tissue's conductivity and E_{RMS} is the root-mean square electric field (averaged over a chosen time period) within it.

$$SAR = \frac{d}{dt}\left(\frac{dW}{dm}\right) = \frac{d}{dt}\left(\frac{dW}{\rho dV}\right) = \sigma\frac{E_{\mathrm{RMS}}^2}{\rho} \tag{2.49}$$

The RF-induced heating occurs as a result of both dielectric and resistive losses (interaction of the E-field with polar molecules and ions, respectively). SAR as a measure of the thermal effect of RF exposure is only crudely related to the temperature increase, as it does not take into account the tissue's thermoregulatory functions, neither passive (thermal diffusion) nor active (perfusion). Within the context of Pennes bio-heat equation[71] given by (2.50) - where T is the tissue temperature, c is its specific heat capacity, k is its thermal conductivity, and ρ_b, c_b, w_b and T_a are the blood's density, specific heat capacity, perfusion rate and arterial temperature, respectively, and q_m is heat generated by the metabolic processes - the product ρSAR represents the external heat source.

$$\rho c\frac{\partial T}{\partial t} = k\Delta T + \rho_b c_b \omega_b (T_a - T) + q_m + \rho\mathrm{SAR} \tag{2.50}$$

SAR is determined entirely by the design of the RF coil in question and its excitation pattern, the imaged subject's anatomy and their position relative to each other, as well as other conductive surfaces in a sufficient proximity to produce a significant interaction, such as the scanner's gradient coils or the subject's implants. Measuring SAR directly from its definition in (2.49) is impossible, as it requires an E-field map and a knowledge of the tissue conductivity, neither of which can be acquired *in-vivo* during a scan. SAR thus has to be estimated, rather than measured, from the numeric simulations that precisely reproduce the experimental setup. Local SAR is typically averaged over some small mass of tissue (SAR limits during an MR examination in the UK are defined in terms of the 10 g averaged SAR) enclosed in a cube. The ways in which simulation results are incorporated within the SAR supervision framework vary from defining a scaling factor (k-factor) that relates total coil input power to SAR (in the case of a fixed shim configuration) and hard per-channel voltage limits determined from the worst-case SAR performance of the coil (in the case of parallel transmission with arbitrary shims), to real-time SAR monitoring using a compressed Q-matrix, which is an array of per-voxel square matrices derived from the simulation results that map an arbitrary coil's excitation vector to SAR within a given voxel[72].

2.5.3 Q-matrix formalism

Local heating is the primary RF safety concern of the MRI[70, 63]. The use of pTx requires a computationally quick way of estimating the local SAR for an arbitrary excitation vector. Local SAR estimation requires the knowldege of the per-channel E-field patterns alongside the tissue conductivity within a given voxel. Since SAR is proportional to $|\vec{E}|^2$, the SAR within the voxel can be treated as a quadratic form of a square matrix (2.51), termed the Q matrix in the MRI community.

$$\mathrm{SAR} = \mathbf{u}^H \mathbf{Q} \mathbf{u} \tag{2.51}$$

Given an RF coil with N transmit channels, $Q \in \mathbb{C}^{N \times N}$ is a complex positive semi-definite matrix with respect to a coil excitation vector $u \in \mathbb{C}^N$ defined to satisfy the expression (2.51), where the superscript H denotes a Hermitian transpose.

$$\begin{aligned} q_{nn} &= \mathrm{SAR}_n, \\ q_{nm} &= \frac{1}{2}\left[\mathrm{SAR}^r_{nm} - (q_{nn} + q_{mm}) - i\left(\mathrm{SAR}^i_{nm} - (q_{nn} + q_{mm})\right)\right], \\ q_{mn} &= q^*_{nm} \end{aligned} \tag{2.52}$$

The entries of Q are defined according to (2.52)[73]. The diagonal entries $q_{nn} \in Q$ correspond to real SAR_n produced by the coil when only the nth channel is excited with 1 V (peak) of input (the input voltage uniquely determines the current distribution within the transmit element and consequently, the E-field and SAR distribution within the subject for a given simulation setup). The complex off-diagonal elements $q_{nm|n\neq m} \in Q$ describe the pair-wise interaction of the channels n and m following their combined excitation.

Naively setting $q_{nm} = q_{nn} + q_{mm}$ neglects the superposition principle of the E-fields produced by the transmit elements n and m when they are driven simultaneously, therefore there is no way of inferring their combined SAR influence without looking at their simultaneous excitation. However, a single simultaneous excitation produces a single equation with two unknowns, which can be determined uniquely by assessing another combined excitation when the channels are driven at a different phase: $\mathrm{SAR}^{r,i}_{nm}$ thus denote SAR value produced by the coil when n and m are driven in phase and with a $\pi/2$ offset. The choice of $\pi/2$ phase offset, corresponding to $(0+i)$ excitation weight in the complex plane, is thus a matter of convenience, but not necessity, and any other phase offset could have been used to produce the second excitation pattern to uniquely determine the system of equations with two unknowns.

Any higher order interactions (more than two channels excited simultaneously) can be decomposed in terms of the pair-wise interaction of its constituents (owing to the superposition principle) and are thus not unique. Another corollary is that $q_{ij} = q^H_{ji}$ (only relative phase matters). The SAR produced by the coil for a given setup can thus be

uniquely determined by $N \times N$ excitations: N excitations of the channels driven individually in addition to $2 \times N!/\left(2!(N-2)!\right)$ excitations to uniquely determine the pair-wise interactions.

The spectral radius of the Q-matrix provides the worst-case SAR for a fixed total input power. Given that the Q-matrix is defined for each voxel within the model, the size of the array needed to describe the SAR within the digital human body model (often, within multiple models in order to account for the coil's positioning degrees of freedom as well as inter-subject anatomical variations) is unfeasibly large for any form of real-time SAR monitoring using an average desktop system to perform the computations. Therefore in practice, the array of Q-matrices is compressed by trading the number of entries within it for SAR overestimation: instead of each voxel having an individual representation within the Q-matrix, the Q-matrix entries instead describe groups of voxels termed virtual observation points (VOPs).

2.5.4 Q-matrix compression

The number of voxels used to represent a digital human body model (or part of it) is typically on the order of 10^5, making fast SAR computations using the Q-matrix formalism unfeasible on a standard computer equipment. To facilitate quick SAR computations, the Q-matrix array is instead modified to describe the behaviour of clusters of voxels termed virtual observation points (VOPs), at the same time providing an upper bound on the SAR overestimation as a result of aliasing of the voxel Q matrices under a single virtual observation point, and guaranteeing no underestimation.

The algorithm described by Eichfelder and Gebhardt[74] achieves compression by constructing a set P_Ω of non-dominated matrices with respect to a set Ω of all the Q-matrices (meaning that $\forall A \in P_\Omega \wedge \forall S \in \Omega$, $(A - S)$ is positive semi-definite). The algorithm first iteratively clusters the matrices $S \in \Omega'$ - where Ω' denotes a set of remaining matrices after each iteration - into a subset $C \subset \Omega'$ such that $S \in C \iff (S - B^*)$ is ϵ-psd, where $B^* \in \Omega'$ termed the core matrix denotes a matrix with the largest spectral norm within Ω', and ϵ-psd stands for a relaxed positive semi-definite condition up to some $\epsilon \geq 0$ i.e. $\forall u \in \mathbb{C}^N$, $u^H(S - B^*)u \geq -\epsilon$, where u is a complex normalised excitation vector.

The VOP $A \in P_\Omega$ for each cluster C is then constructed by setting $A = B^* + Z^*$, where the matrix $Z^* = \min\{\|Z\| \mid (B^* + Z) - S \text{ is psd } \forall S \in C\}$ is computed from solving an optimisation problem. No SAR underestimation is guaranteed from the way the VOPs were constructed. The SAR overestimation upper bound is solely determined by $\|Z^*\|$, which in turn depends on the choice of ϵ. The upper bound can thus be guaranteed by imposing an additional constraint during the VOP generation by either keeping the $\|Z^*\|$ below - or ϵ above - a certain threshold.

2.5.5 MR Coil SAR validation

$$\rho c \frac{\partial T}{\partial t} = k\Delta T + \rho \mathrm{SAR} \tag{2.53}$$

Validity of the simulated SAR behaviour can be determined to a reasonable degree of accuracy within a dosimetry phantom by comparing the measured and simulated temperature changes. If the simulated coil's behaviour agrees with measurements within a given setup, it is assumed the simulated behaviour is also valid for other setups, up to the simulation setup reproduction accuracy. Temperature rise and SAR are related via a heat transfer model, which in the simplest case (homogeneous, thermally isolated solid) can be given by a heat equation that only considers thermal diffusion (2.53). For a sufficiently small k, the relationship reduces to a definition of the specific heat capacity. The temperature rise maps can therefore be simulated by numerically solving a heat transfer problem (or computing the temperature rise from the definition of heat capacity). The temperature rise in practice can be measured using a proton resonance frequency shift (PRF) thermometry, with the temperature increase being given by (2.54), where $\Delta\phi$ denotes a phase a shift, α is a temeprature-dependent chemical shift coefficient, B_0 is the main magnetic field strength, γ is the ^1H gyromagnetic ratio and t_E is the echo time[75].

$$\Delta T = \frac{\Delta\phi}{\alpha\gamma B_0 t_E} \tag{2.54}$$

2.5.6 Regulatory SAR safety limits

Operation mode	Trunk SAR_{10g}
Normal	10 W/kg
1st	20 W/kg

Table 2.2: Summary of the IEC 60601-2-33 standard limits for local 10 g averaged SAR over 6 minutes in the trunk during an MR examination.

The regulatory SAR limits in the UK for the RF exposure during an MR examination are set out by the Medicine and Healthcare Products Regulatory Agency (MHRA), which itself follows the IEC 60601-2-33 standard[63, 64]. The up-to-date local trunk 10 g averaged SAR limits over 6 minutes for the normal and 1st level operating modes at below 25 °C ambient temperature are summarised in Table 2.2.

Chapter 3

Coil simulations

3.1 Design considerations

The array design began with a formulation of the criteria it has to meet and the imposed limitations. The number of transmit channels on the Siemenes Magnetom Terra 7T scanner on the QEUH site is limited to eight. From the PIRADS guidelines for the prostate imaging using 1.5-3T clinical systems, it was determined that the coil should be capable of providing a good SNR within the $20 \times 20 \times 20$ cm FOV surrounding the prostate. The coil should provide adequate B_1+ and SAR performance in the middle of the pelvis, roughly where the prostate gland resides. For a subject of average size, this corresponds to approximately 10 cm anteriorly or posteriorly. The DWI and DCE protocols used in prostate examination would particularly benefit from a low g-factor. Pursuing the ability to accommodate subjects with a wide range of pelvis circumferences, it was decided to have the coil comprise two halves: anterior and posterior. The cushions used to line the scanner's table are about 5 cm in height, and to facilitate the coil's seamless integration into the clinical routine it was decided to limit the posterior half's thickness to that value. The anterior half must be as thin as reasonably possible to provide enough room for fitting larger patients into the bore. The anterior half must also be light to minimise pressure on the patient, as it is not unreasonable to assume that patients with some pathologies in the pelvic/abdominal region might experience pain from excess compression caused by a heavy object.

It was decided that the posterior half would be made rigid to simplify the construction and provide a comfortable patient rest. The decision to make the anterior half rigid was motivated by a reduction in the degrees of positioning freedom. The latter is beneficial at the coil safety approval stage and can yield a smaller safety factor related to the positioning uncertainties.

The loop sensitivity at depth is proportional to its circumference. The number of channels covering the anatomy of interest therefore has to be balanced against the loop dimensions. Two arrangements were been considered: a single row of large loops and a dual row of

smaller loops. Three 20x12.5 cm chamfered rectangular loops were considered for a single row arrangement. Assuming a decoupling overlap on the order of 20-30%, three 20x12.5 loops are sufficient to cover the width of the average person's abdomen. Smaller 15x12 cm loops were used for a dual row arrangement of three to four columns. The number of capacitors, distributed symmetrically and as uniformly as possible along the loops, was decided to be kept on the order of a dozen as a compromise between the imparted resistive losses (equivalent series resistance of the capacitor and the added solder joint resistance) and sample loading stability.

It was hypothesised that keeping the array elements further away from the subject would result in a reduced capacitive coupling, lowering the SAR and increasing the SAR performance at depth. For this reason, an air gap was introduced between the subject and the loops. An additional benefit of the inclusion of an air gap is a guarantee on the spacing between the electronics and the subject, requiring no additional padding for the subject placement. A local shield was introduced to improve the tuning stability, as it ensured the elements were unaffected by the coupling to the gradient coils.

3.2 Simulation procedure

3.2.1 Simulation setup

The project simulations were performed in a commercial EM simulation software CST Studio Suite 2019-2022 running on an HP Z8 G4 workstation. A finite-difference time-domain (FDTD) solver was used to acquire the RF coil frequency response over the 275-325 MHz range in a single simulation run. GPU acceleration was used to speed up the computations.

The simulation setup comprised a coil, load (phantom or a digital body model) and the scanner bore. The bore was modelled as a rectangular block of PEC with a cylindrical hole the size of the Siemens Magnetom Terra's gradient shields (650 mm diameter, 1500 mm lengths) to enable the use of PEC boundary along the x and y axes. This allowed for a reduction in size of the computational domain as the PML along these directions was no longer needed. If the bore was omitted from the simulations, a PML was specified for all directions to avoid the reflection from the computational domain boundary.

The coil elements were modelled as 2 mm thick round silver wires. The local coil shield was modelled as a 1 mm thick copper sheet. The capacitors on the loops were modelled as lumped elements in between the 6.35 mm gaps. The feed points were realised as fixed 50 Ohm impedance discrete ports. Discrete ports were additionally used to define the tuning capacitors on the loops, and the decoupling transformers. Discrete ports are constructs defined between the two points in space to serve as the power injection points for the simulation in CST. Discrete ports are used to realise ideal voltage and current sources, as well as fixed impedance inputs. A fixed 50 Ohm impedance port models feeding the

antenna with a 50 Ohm coaxial cable. The voltages and currents are monitored at discrete ports to build the setup's transfer function, allowing the setup to be treated as a black box in circuit co-simulation. For this reason, the number of excitations is equal to the number of discrete ports. L-networks with a series inductance followed by a parallel capacitance were used to match the coil elements to 50 Ohms in circuit co-simulation.

Tissue parameters of the digital human body models (5 mm Duke, 5 mm Hugo and 2 mm Rosalind) were re-calculated for the central operating frequency of 297.2 MHz at the import stage using a built-in CST macro that fits the data to a four-pole Cole-Cole model. All the performance assessments at the simulation stage were done on the Duke digital body model, with Hugo and Rosalind being used at the safety assessment stage of the final configuration to gauge the inter-subject SAR variability. Assessing the performance on multiple digital body models is redundant at the simulation stage. A coil configuration exhibiting superior performance in one digital body model will still exhibit a superior performance in other body models (compared to other configurations). The mesh resolution of the coil elements varied between 0.5 mm and 1 mm, depending on the local geometry. The digital body model mesh resolution was set to the model's voxel size (either 2 mm or 5 mm). However, the finer mesh of the surrounding coil elements would result in a finer mesh within the digital body model.

Only the posterior half of the loop configurations was simulated at the prototyping stage to save time. It was assumed that the electromagnetic interaction between the two halves would be weak due to the shielding from the tissue, and an improvement in the performance of one half of the array will produce an improvement in the performance of the full array.

The optimal decoupling overlap for the loop configurations was determined by varying it between the simulations. For both the single-row and dual-row arrangements, the starting overlap was chosen to be 2.5 cm along the row direction, and 3.5 cm along the column direction for the dual-row arrangement. The overlap was varied by 1 mm either way in the first two simulations to determine a trend in the transfer parameter (S_{21}) change between the input ports of the neighbouring loops. Afterwards, the overlap was varied in the direction that minimised the transfer parameter until the trend reverses, suggesting that the optimum was found. In dual-row arrays, the procedure was initially performed separately for rows and columns using pairs of loops. A second pair was added once the optimal overlap was determined for an isolated pair, starting another round of optimisation to fine-tune the overlaps that were determined for the isolated case. A single port excitation would typically take between 30 and 60 minutes to process, depending on the number of mesh cells in the model. The excitation time could reach 105 minutes for setups that used whole body models. The steady state accuracy limit was set to -60 dB. The number of ports per loop varied between 2 and 4 for different configurations: 2 were reserved for the loop feed and the tuning capacitor, whilst additional 1 to 2 ports would be added to implement transformer decoupling (such as in the dual row

configurations where the transformers are needed to decouple the diagonal neighbours). A single optimisation run, starting from two loops and totalling 6 excitation ports, would thus take between 3 and 6 hours. It would typically take 3-6 runs in total to find an optimal overlap along one of the directions (row-wise or column-wise). The preliminary optimisation steps thus required between 9 and 36 hours. A full configuration can then be assembled and fine-tuned with around 3 additional runs, but with a greater number of ports. The 4x2 arrangement of loops counted 28 ports in total and took 60 minutes per port to simulate. Doing 3 additional runs would therefore take 3.5 days, bringing the total number of hours up to 120. Varying the shield and load distance required simulation with the whole configuration assembled, averaging 2 runs per parameters update (the additional run would sometimes be required to fine-tune the overlap). The discussed timings only take into account the simulation time, and do not account for troubleshooting that was sometimes required.

3.2.2 B1 and SAR data generation

The SAR maps used in Q matrix array generation were computed from the CST's power loss monitors using a built-in *'General SAR result'* macro from CST's MRI Toolbox. The averaging was performed over a 10 g cube of tissue using CST C95.3 algorithm, which is a modification of IEEE C95.3 standard that discards the voxels with an air fraction of more than 20%. Initially, the SAR maps were exported from CST using the programme's generic field export method. However, because the method enforces linear interpolation, it was discarded later in the project as it was serving as an unnecessary source of error. Instead, the SAR results were later on read into MATLAB directly from the outputted binary m3d file, which store in the sequential order the SAR values for every mesh grid point.

The per-channel B_1+ maps were computed from their respective H-field results for 1 V of input using a built-in *'Calculate B1+ and B1-'* macro from CST's MRI Toolbox, which sets $B = H$ since the human tissue is non-magnetic and follows the definition of B_1+ and B_1-. Due to a difference in the phase sign convention between CST and physics, the B_1 fields were computed assuming an opposing B_0 direction to what is in the scanner to maintain a physically accurate definition of the B_1+ and B_1- fields. The computed B_1 maps were exported on a 2 mm resolution uniform grid using a generic CST field export method [1]. The exported B_1 maps were packaged into structured MAT files for convenience, containing 4-D arrays of B_1+ and B_1- fields, and a coordinates grid.

[1] Although raw B_1 data could be accessed from the m3d file in a similar fashion to the SAR results, the file structure was not as straight-forward for the vector field. There is padding between the component values that could be determined, but due to time limitations this was left to be addressed later.

3.2.3 Prostate mask generation

In order to focus the shimming on the prostate gland, a mask was generated using a built-in *FlagByMaterial()* method in CST, which flags the mesh grid if the queried material is defined on it. The functionality was not documented and was discovered by analysing the built-in macro that computes field statistics based on criteria such as the name of the solid or material. The resulting mask was exported using a generic CST field export method, using the same sub-volume and resolution (2 mm) as the B_{1+} exports.

3.2.4 Q matrix generation

The diagonal entries $q_{ii} \in \mathbf{Q}$ correspond to the SAR produced by the ith element (SAR_{ii}). The off-diagonal entries $q_{ij} \in \mathbf{Q}$ can be derived using two methods. The first method involves defining fictitious squared electric field amplitudes $a_{ij} = e_i e^*_{j>i}$ that are substituted into (2.49) to compute the entries above the matrix diagonal. The entries below the matrix diagonal are computed by taking a complex conjugate of the elements above the diagonal. The second method involves computing the off-diagonal coefficients from the known SAR results by working backwards. A pair of transmitters i and j have associated with them a sub-matrix $\mathbf{Q}_{ij}$.

$$\mathbf{Q}_{ij} = \begin{pmatrix} q_{ii} & q_{ij} \\ q_{ji} & q_{jj} \end{pmatrix}$$

The off-diagonal entries are linked by a conjugate symmetry $q_{ij} = q^*_{ji}$, meaning that the only unknowns are $\mathrm{Re}\{q_{ij}\}$ and $\mathrm{Im}\{q_{ij}\}$. Both $\mathrm{Re}\{q_{ij}\}$ and $\mathrm{Im}\{q_{ij}\}$ can be found by solving a system of two linear equations, which are constructed by considering the SAR produced by two distinct excitation vectors $\mathbf{w}_1$ and $\mathbf{w}_2$ involving only the channels i and j.

$$\begin{cases} \mathbf{w}_1^H \mathbf{Q}_{ij} \mathbf{w}_1 = \mathrm{SAR}_{ij} \\ \mathbf{w}_2^H \mathbf{Q}_{ij} \mathbf{w}_2 = \mathrm{SAR}_{ji} \end{cases}$$

A convenient choice of $\mathbf{w}_1$ and $\mathbf{w}_2$ is the in-phase $\begin{pmatrix} 1 & 1 \end{pmatrix}$ and quadrature $\begin{pmatrix} 1 & i \end{pmatrix}$ excitation. The convenience of multiplying by unity, coupled with the first coefficient being shared between the two excitation vectors, simplifies the algebraic manipulation. Assuming this choice of excitations, the expression for q_{ij} is given by (3.1), where SAR_{ij} is the SAR induced by a pair of elements i and j driven in-phase, and SAR_{ji} is the SAR induced by a quadrature excitation of the same pair. CST uses the engineering convention for the sign of the phasor. The complex excitation weight in CST is computed by multiplying the amplitude with $\exp\{i\phi\}$. This is the opposite of what is done in the Siemens Magnetom Terra scanner on the Glasgow site, where the amplitudes are multiplied by $\exp\{-i\phi\}$. The two $\mathbf{Q}$ matrices constructed using these two different conventions are related via a regular transpose (or, equivalently, its conjugate, due to $\mathbf{Q}$ being Hermitian) $\mathbf{Q}(-i\phi) = \mathbf{Q}^T(i\phi)$. The quadrature excitation definition can be flipped from $\begin{pmatrix} 1 & i \end{pmatrix}$ to $\begin{pmatrix} i & 1 \end{pmatrix}$ in CST to produce a $\mathbf{Q}$ matrix from the CST results that is valid on the scanner without the need

to transpose or conjugate it as the last processing step.

$$q_{ij} = \frac{1}{2}\left(\mathrm{SAR}_{ij} - (q_{ii} + q_{jj}) - i\left[\mathrm{SAR}_{ji} - (q_{ii} + q_{jj})\right]\right) \tag{3.1}$$

In total, N^2 SAR results are required to reconstruct the $\mathbf{Q}$ matrix in this manner, as every pair of elements has to be considered.

Because the SAR computation API in CST uses the scalar power loss density (PWD) maps to compute the SAR, the first method cannot be used as it relies on complex coefficients to express the fictitious $|\mathbf{E}|^2$. The second method is used instead.

The PWD maps required for the outlined N^2 SAR computations in CST are computed using the "AC, Combine Result" task. This module updates the 3D fields results based on the circuit excitation. The excitation vector on the Siemens Magnetom Terra system has the units of volts. The SAR results needed for the $\mathbf{Q}$ matrix generation must be scaled accordingly. The amplitude and phase settings used within the "AC, Combine Result" task to realise the required excitations are listed in Table 3.1.

Excitation	A_i, $\sqrt{\mathrm{W}}$	A_j, $\sqrt{\mathrm{W}}$	ϕ_i	ϕ_j
$i = j$	0.2	0	0	0
$i < j$	0.2	0.2	0	0
$i > j$	0.2	0.2	90°	0

Table 3.1: Amplitude (peak-to-peak) and phase settings used to define the excitations required to produce the PWD maps used in N^2 SAR computations needed for the $\mathbf{Q}$ matrix reconstruction. The "Excitation" tab describes the relationship between a pair of port indices. The quadrature excitation is flipped such that no transposition is required to make the Q matrix valid with the scanner's phasor sign convention.

The 10 g averaged SAR is computed using CST's SAR method. The settings used to compute the SAR are listed in Table 3.2.

Parameter	Value
Averaging mass, g	10 (default)
Volume accuracy, %	0.0001
Averaging method	CST95.3
Computational grid	Simulation mesh

Table 3.2: Settings used for SAR calculation using the CST's built-in SAR method.

The output of a SAR computation result is a binary m3d file. The computed SAR results are not explicitly exported. Instead, the SAR values are read directly from the outputted m3d files as single-precision floats. This method is chosen in place of a built-in field export macro due to the interpolation error introduced by the latter.

3.2.5 VOP generation

The arrays of Q matrices were compressed using a compression tool supplied by Siemens which implements the Eichfelder and Gebhardt algorithm to produce an array of VOPs. The compression ratio was controlled by setting a limit to the worst-case SAR overestimation of the associated Q matrix cluster. An overestimation of 3% was used to generate the VOPs used to compute the shims (discussed in detail in the following section). VOPs were used in place of uncompressed Q matrices to speed up the computation times, as the resulting VOP matrix array was on the order of 10^3 smaller that the original Q matrix array.

3.2.6 Shimming procedure

Shimming in the context of B_1+ fields refers to a process of finding an excitation vector of the coil that produces a desired B_1+ field distribution. A "shim" thus refers to an excitation vector that produces the desired B_1+ field distribution. Each channel has associated with it a driving amplitude and phase. Either or both can be adjusted. If only the channel phase is adjusted, the shimming is referred to as phase shimming. In the simulated performance discussion to follow, a "B_1+ efficiency" shim refers to a shim that maximises the mean B_1+ field within the prostate gland, whilst an "SAR shim" refers to a shim that maximises the SAR efficiency when mean B_1+ field within the prostate is considered.

The shimming for the project was carried out in MATLAB using the per-channel B_1+ maps and compressed arrays of Q matrices (VOPs) generated from the simulation results. A constrained optimisation with a built-in MATLAB function *fmincon()* was used to derive the B_1+ and SAR efficiency shims using a sequential quadratic programming (SQP) algorithm. The B_1+ maps were scaled by a factor of 10^6 to be in the units of μT in order to approximate the scaling of the SAR result. This was made to ensure that the target metrics (B_1+ and SAR efficiencies) would be on the order of 10^-1. The variables being optimised were N (total number of transmit channels) per-channel amplitudes and $N-1$ phase values in radians. The amplitudes were bound to the range $[0; 10]$ and the phases were bound to the range $[-2\pi; 2\pi]$. The arguments were converted into a normalised excitation vector ($w = a\exp\{i\phi\}$, where w is the excitation weight, a is amplitude and ϕ is phase)for computing the SAR and the mean B_1+. When optimising for B_1+ efficiency, the target function being minimised was the negative of the mean B_1+ value within the prostate voxels. When optimising for SAR efficiency, the target function being minimised was the inverse of the SAR efficiency ($B_{1+}^{\text{mean}}/\sqrt{\text{pSAR}}$). The number of function evaluations was set to 10^5 for each run. A uniformly-sampled random set of parameters was used as the initial guess. The phase values were normalised to the range $[-\pi; \pi]$ each time, but rescaling the amplitudes was unnecessary due to the excitation vector undergoing normalisation before the target function evaluations. The number of initial guesses for which the optimisation was run varied between 10 and 1000, but 10 was

found to be sufficient most of the time.

3.2.7 Transmit performance evaluation

The transmit performance was defined with respect to the mean B_1+ magnitude produced per square root of input power within the prostate gland.

3.2.8 SAR performance evaluation

The SAR performance was defined as a ratio of the mean B_1+ magnitude produced within the prostate gland to peak 10 g SAR observed for the model. The worst-case performance of the array was computed by finding the largest spectral norm out of all the Q matrices.

3.3 Loop configurations

3.3.1 Phased 4x2 array

3.3.1.1 Configuration

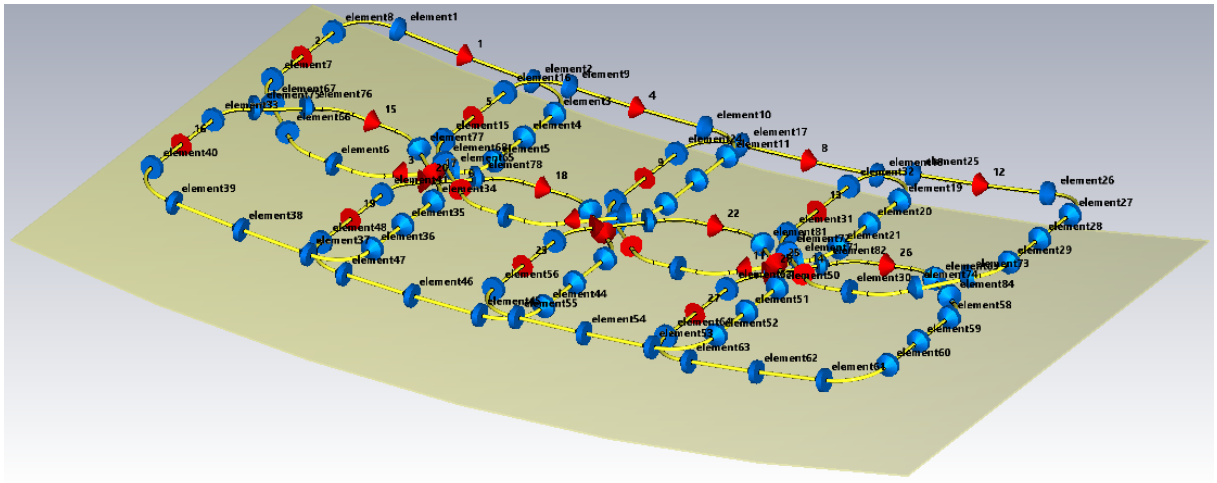

Figure 3.1: A CST view of the 4x2 loop array configuration. The discrete ports are shown in red, the lumped capacitors are shown in blue.

The 4x2 posterior loop array comprised a shielded phased array of eight loops arranged in two rows. A CST view of the configuration is shown in Fig. 3.1. The summary of the array dimensions is shown in Table 3.5. The neighbouring elements were decoupled with an overlap. The diagonal elements were decoupled with a transformer in circuit co-simulation. Decoupling for the next-neighbouring elements was not necessary, as the decoupling was better than -16 dB for the whole array. The column-wise pairs of loops formed a single transmit element that was driven in-phase through a 3 dB power splitter in circuit co-simulation.

Parameter	Value
Loop width	12 cm
Loop length	15 cm
Number of capacitors	13
Capacitor value	9.1 pF
Row overlap	2.6 cm
Column overlap	4.2 cm
Distance to load	2 cm
Distance to shield	3 cm
Shield length	33.5 cm
Shield width	42 cm
Curvature radius	120 cm

Table 3.3: Summary of the 4x2 posterior loop array dimensions.

3.3.1.2 Simulated performance

The simulated combined B_1 and SAR maps of the 4x2 posterior loop array within the Duke digital body model are shown in Fig. 3.2. The summary of the array performance is provided in Table 3.4.

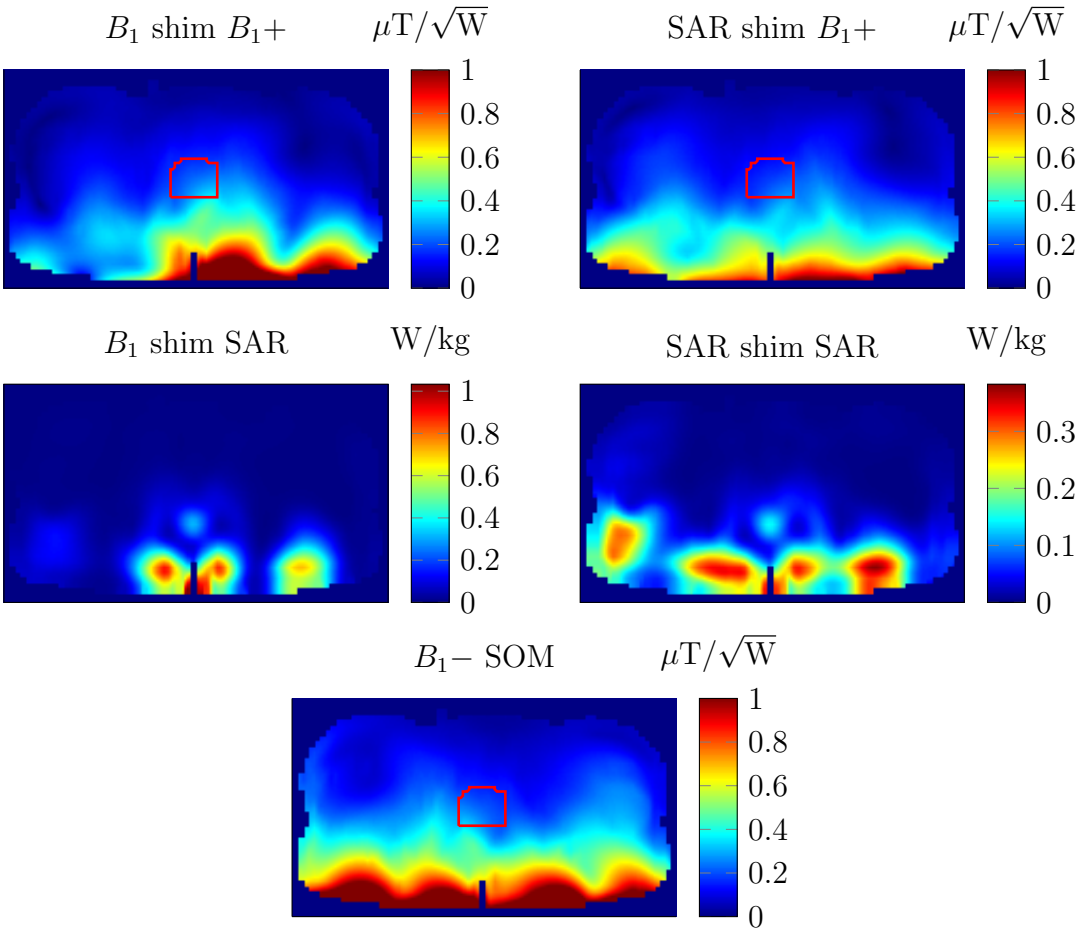

Figure 3.2: Performance summary of the 4x2 loop configuration posterior half within the Duke digital body model using the numerically derived prostate B_1+ and SAR efficiency shims. The peak SAR values are provided for 1 W of input power. The SAR map is given for an axial slice where the hotspot occurs for the corresponding shim. Also included is the mean B_1- sum of magnitudes (SOM) within the prostate.

Shim	Mean B_1+, $\mu T/\sqrt{W}$	SAR, W/kg	SAR eff., $\mu T/\sqrt{pSAR}$	Mean B_1- SOM, $\mu T/\sqrt{W}$
B_1+	0.230	1.033	0.226	0.217
SAR	0.184	0.383	0.297	

Table 3.4: Performance summary of the 4x2 posterior loop array within the Duke digital body model using the numerically derived prostate B_1+ and SAR efficiency shims. The peak SAR values are provided for 1 W of total input power. Also included is the mean B_1- sum of magnitudes (SOM) within the prostate.

3.3.2 Phased 3x2 array

3.3.2.1 Configuration

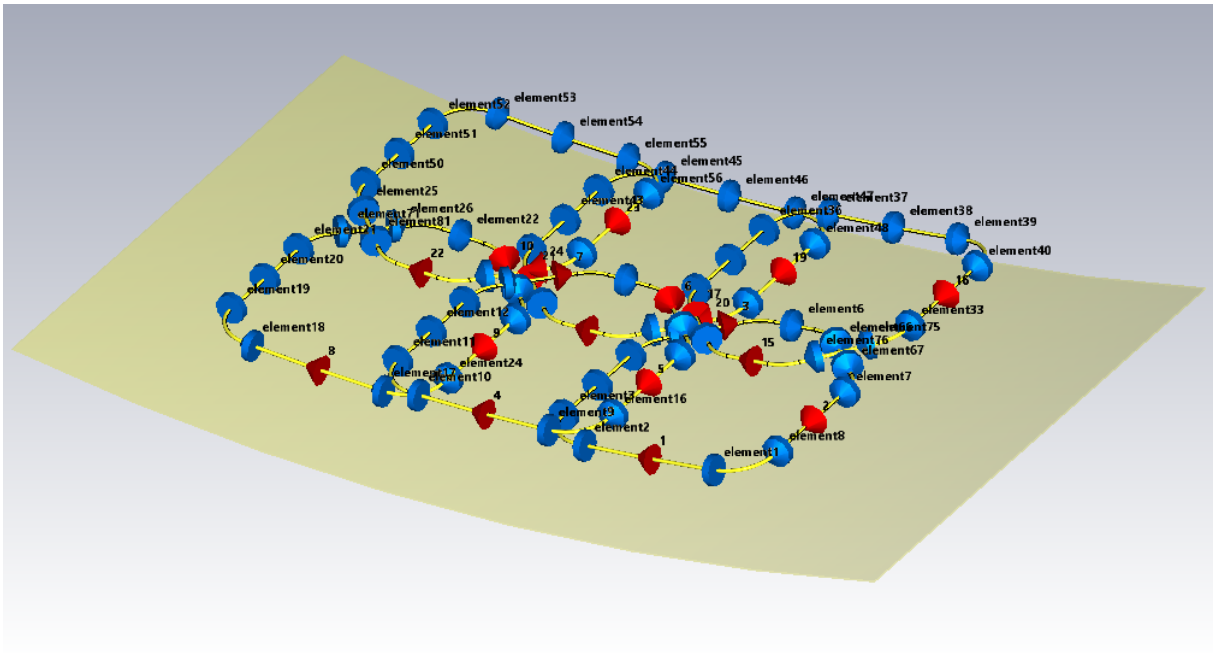

Figure 3.3: A CST view of the 3x2 loop array configuration. The discrete ports are shown in red, the lumped capacitors are shown in blue.

The 3x2 posterior loop array comprised a shielded phased array of six loops arranged in two rows. A CST view of the configuration is shown in Fig. 3.3. The summary of the array dimensions is shown in Table 3.5. The neighbouring elements were decoupled with an overlap. The diagonal elements were decoupled with a transformer in circuit co-simulation. Decoupling for the next-neighbouring elements was not necessary, as the decoupling was better than -16 dB for the whole array. The column-wise pairs of loops formed a single transmit element that was driven in-phase through a 3 dB power splitter in circuit co-simulation.

Parameter	Value
Loop width	12 cm
Loop length	15 cm
Number of capacitors	13
Capacitor value	9.1 pF
Row overlap	2.6 cm
Column overlap	4.2 cm
Distance to load	2 cm
Distance to shield	3 cm
Shield length	33.5 cm
Shield width	42 cm
Curvature radius	120 cm

Table 3.5: Summary of the 3x2 posterior loop array dimensions.

3.3.2.2 Simulated performance

The simulated combined B_1 and SAR maps of the 3x2 posterior loop array within the Duke digital body are shown in Fig. 3.4. The summary of the array performance is provided in Table 3.6.

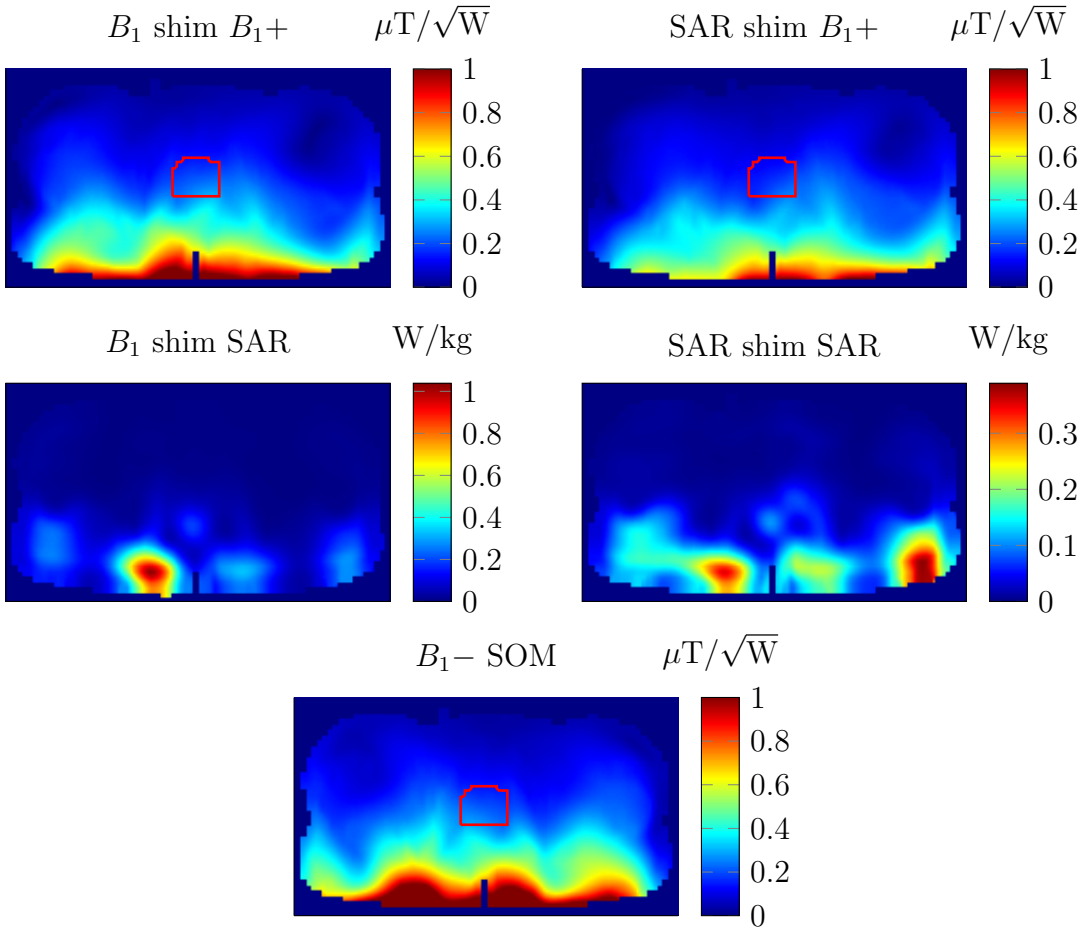

Figure 3.4: Performance summary of the 3x2 loop configuration posterior half within the Duke digital body model using the numerically derived prostate B_1+ and SAR efficiency shims. The peak SAR values are provided for 1 W of input power. The SAR map is given for an axial slice where the hotspot occurs for the corresponding shim. Also included is the mean B_1- sum of magnitudes (SOM) within the prostate.

Shim	Mean B_1+, $\mu T/\sqrt{W}$	SAR, W/kg	SAR eff., $\mu T/\sqrt{pSAR}$	Mean B_1- SOM, $\mu T/\sqrt{W}$
B_1+	0.207	1.039	0.203	0.208
SAR	0.166	0.389	0.266	

Table 3.6: Performance summary of the 3x2 posterior loop array within the Duke digital body model using the numerically derived prostate B_1+ and SAR efficiency shims. The peak SAR values are provided for 1 W of total input power. Also included is the mean B_1- sum of magnitudes (SOM) within the prostate.

3.3.3 Phased 3x1 array

3.3.3.1 Configuration

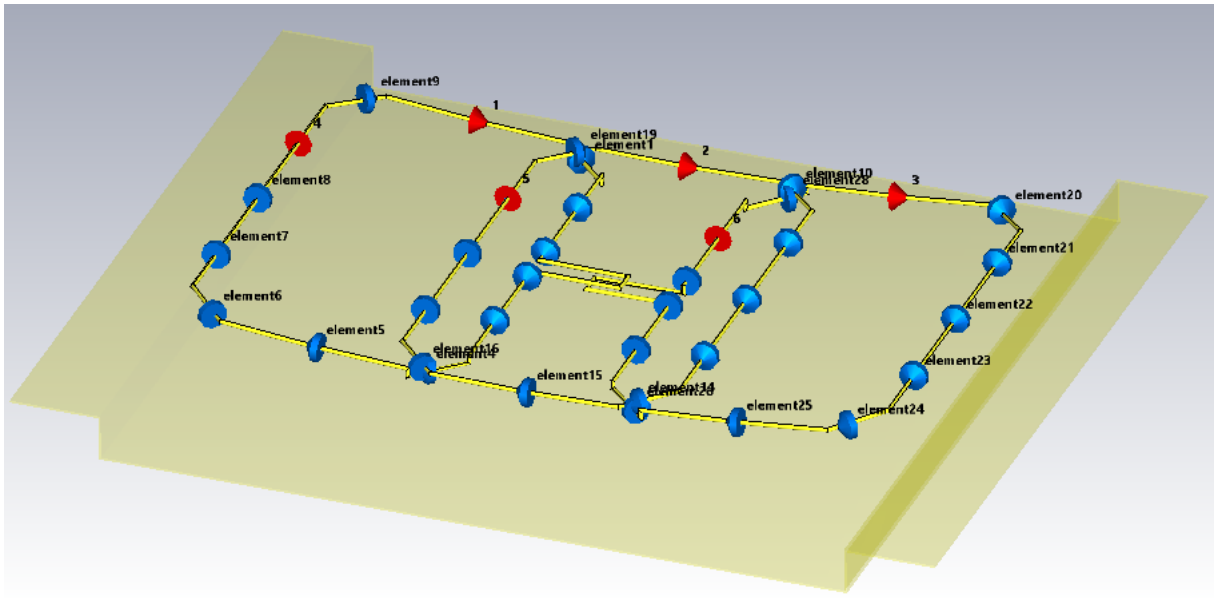

Figure 3.5: A CST view of the overlapped 3x1 loop array configuration. The discrete ports are shown in red, the lumped capacitors are shown in blue. The ports 1, 2, 3 are the feed points and the ports 4, 5, 6 are the tuning capacitors.

The 3x1 posterior loop array comprised a shielded phased array of three loops. A CST view of the configuration is shown in Fig. 3.5. The summary of the array dimensions is shown in Table 3.7. The neighbouring elements were decoupled with an overlap. Two variants of the array were considered with regards to the next-neighbouring decoupling: (1) without any additional decoupling, and (2) featuring overlapped protrusions.

Parameter	Value
Loop width	12.5 cm
Loop length	20 cm
Loop overlap	3 cm
Number of capacitors	12
Capacitor value	6.8 pF
Distance to load	2 cm
Distance to shield	3 cm
Shield length	33.5 cm
Shield width	42 cm
Curvature radius	120 cm

Table 3.7: Summary of the 3x1 posterior loop array dimensions.

3.3.3.2 Simulated performance

The simulated combined B_1 and SAR maps of the two 3x1 posterior loop array variants within the Duke digital body model are shown in Fig. 3.6. The summary of the array

performance is provided in Table 3.8.

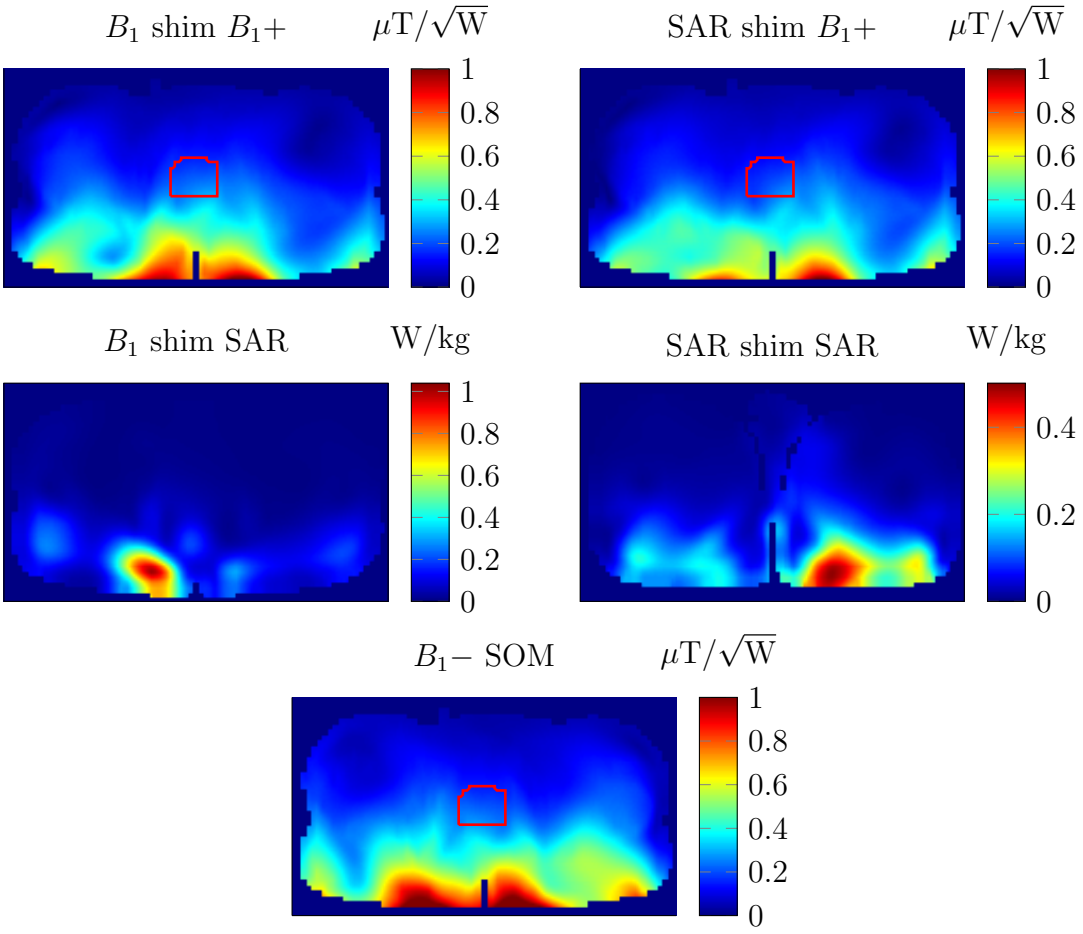

Figure 3.6: Performance summary of the 3x1 loop configuration (without the next-neighbouring decoupling) posterior half within the Duke digital body model using the numerically derived prostate B_1+ and SAR efficiency shims. The peak SAR values are provided for 1 W of input power. The SAR map is given for an axial slice where the hotspot occurs for the corresponding shim. Also included is the mean B_1- sum of magnitudes (SOM) within the prostate.

Configuration	Shim	Mean B_1+, $\mu T/\sqrt{W}$	SAR, W/kg	SAR eff., $\mu T/\sqrt{pSAR}$	Mean B_1- SOM, $\mu T/\sqrt{W}$
No overlap	B_1+	0.216	1.039	0.212	0.210
	SAR	0.192	0.502	0.271	
Overlapped	B_1+	0.215	1.035	0.211	0.210
	SAR	0.189	0.496	0.269	

Table 3.8: Performance summary of the overlapped and non-overlapped 3x1 posterior loop array configurations within the Duke digital body model using the numerically derived prostate B_1+ and SAR efficiency shims. The peak SAR values are provided for 1 W of total input power. Also included are the mean B_1- sums of magnitudes (SOM) within the prostate.

3.3.3.3 Discussion

The configuration with the next-neighbouring decoupling demonstrates a slightly decreased performance. However, the performance of the two variants is virtually identical.

3.3.4 Comparison

The table comparing the simulated performance of the 4x2, 3x2 and 3x1 loop array configurations is presented in Table 3.9. The 4x2 configuration demonstrated the highest performance of the four configurations. The difference in performance between the overlapped and non-overlapped variants of a 3x1 configuration were negligible. The worst performance was demonstrated by the 3x2 configuration.

Shim	Configuration	Mean B_1+, $\mu T/\sqrt{W}$	SAR, W/kg	SAR eff., $\mu T/\sqrt{pSAR}$	Mean B_1- SOM, $\mu T/\sqrt{W}$
B_1+	4x2	0.230	1.033	0.226	0.217
	3x2	0.207	1.039	0.203	0.208
	3x1 non-overlapped	0.216	1.039	0.212	0.210
	3x1 overlapped	0.215	1.035	0.211	0.210
SAR	4x2	0.184	0.383	0.297	0.217
	3x2	0.166	0.389	0.266	0.208
	3x1 non-overlapped	0.192	0.502	0.271	0.210
	3x1 overlapped	0.189	0.496	0.269	0.210

Table 3.9: Summary of the performance of the simulated 4x2, 3x2 and 3x1 loop configuration posterior halves within Duke digital body model using the prostate gland as the shim target.

The presented 4x2 configuration results were not available at the time when the decision was made on which coil configuration to construct. The 4x2 configuration was the first configuration simulated as part of this project. The initial results did not favour this configuration, because the tissue parameters were not re-calculated for the frequency of 297.2 MHz. By default, the tissue parameters of Duke body model are specified for 900 MHz. The tissue conductivity is considerably higher at this frequency, leading to a decrease in penetration depth, and consequently weaker B_1 fields within the prostate region. The 3x1 configuration demonstrated the best performance at the decision making point, and was chosen for further development. In the coming sections, the simulated performance results of the six-channel loop array derived from the 3x1 configuration are presented. Also considered is an eight-channel shortened dipole array.

3.4 Six-channel loop array

3.4.1 Configuration

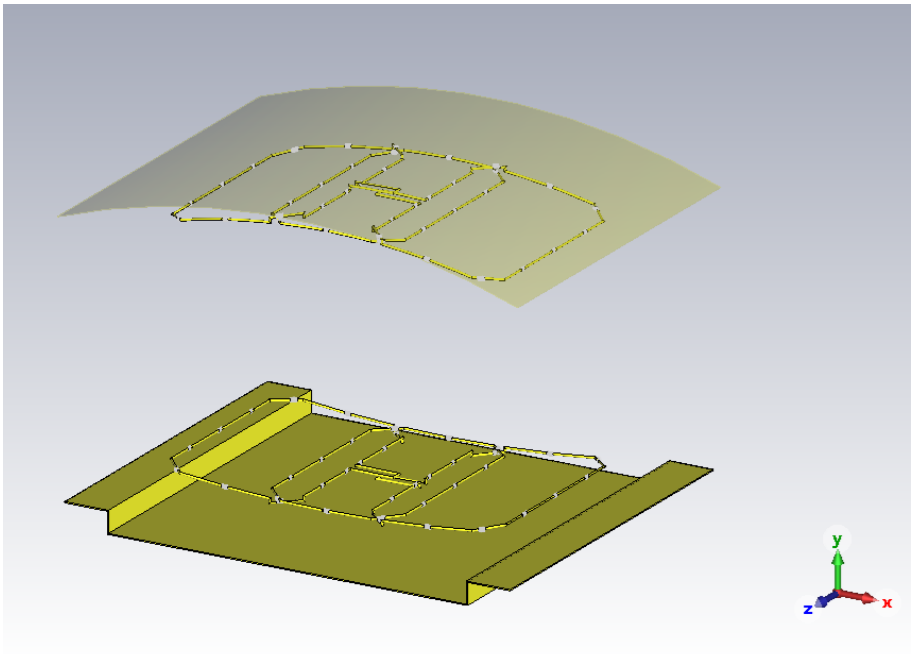

Figure 3.7: A CST view of the six-channel loop array.

The six-channel loop array comprised an anterior and posterior half housing the next-neighbour-decoupled 3x1 loop configuration discussed in the previous section. The anterior half's curvature radius was reduced from 120 cm to 90 cm to better follow the shape of the abdomen. A CST view of the configuration is shown in Fig. 3.7. Despite the adjustment to the anterior half's geometry, the decoupling overlap derived for the posterior half remained optimal. The matching network was changed to an L-network comprising series capacitors followed by a parallel capacitor. Furthermore, an uncompressed array of Q matrices was used to compute the SAR shim instead of the compressed array of the VOPs.

3.4.2 Simulated performance

The simulated combined B_1 and SAR maps of the six-channel loop array within the Duke digital body model are shown in Fig. 3.8. The summary of the array performance is provided in Table 3.10.

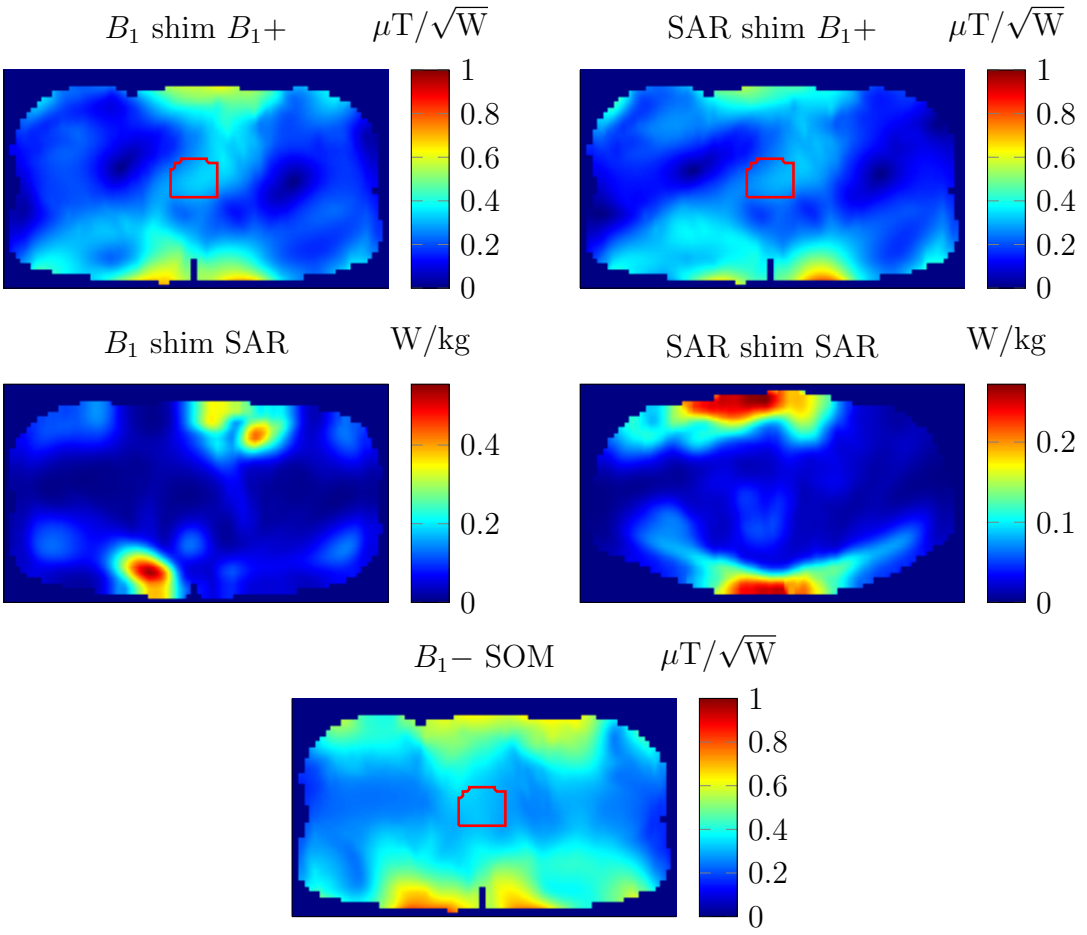

Figure 3.8: Simulated combined B_1 and SAR maps of the six-channel loop array within the Duke digital body model using B_1 and SAR efficiency shims. The B_1 maps are shown for the central axial slice. The B_1- map corresponds to a sum of magnitudes of the per-channel B_1- patterns. The SAR maps are given for 1 W of input power. The SAR map is given for an axial slice where the hotspot occurs for the corresponding shim.

Shim	Mean B_1+, $\mu T/\sqrt{W}$	SAR, W/kg	SAR eff., $\mu T/\sqrt{pSAR}$	Mean B_1- SOM, $\mu T/\sqrt{W}$
B_1+	0.291	0.555	0.390	0.299
SAR	0.261	0.272	0.501	

Table 3.10: Performance summary of the six-channel loop array within the Duke digital body model using the numerically derived prostate B_1+ and SAR efficiency shims. The peak SAR values are provided for 1 W of total input power. Also included is the mean B_1- sum of magnitudes (SOM) within the prostate.

3.4.3 Effect of the B1+ export interpolation on the reported metrics

There exists a small discrepancy between the exported B_1 values and the values computed on the mesh grid due to the interpolation enforced by CST's generic field export method. The B_1 magnitude is therefore always slightly under-reported in the exported

results. When the numerically derived SAR shim was transferred to CST to compute the "ground truth", the actual mean B_1+ within the prostate was shown to be 0.267 $\mu T/\sqrt{W}$. Consequently, the SAR performance is 0.512 $\mu T/\sqrt{pSAR}$ (the SAR result computed with the Q matrix and with CST is identical).

3.4.4 Additional simulation using a 2 mm resolution Duke model

An additional simulation using a 2 mm resolution Duke model was carried out. The nominal efficiency was found to be 0.303 $\mu T/\sqrt{W}$, and the nominal SAR efficiency was found to be 0.520 $\mu T/\sqrt{pSAR}$. When phase-only shimming was used, the nominal B_1+ efficiency was found to be 0.300 $\mu T/\sqrt{W}$, and the nominal SAR efficiency was found to be 0.500 $\mu T/\sqrt{pSAR}$. The results for the 2 mm resolution Duke model will be quoted when discussing the simulated performance outside of the context of comparing the simulated configurations within this study (e.g. when comparing the results to the simulated results published in the literature).

3.5 Eight-channel dipole array

3.5.1 Configuration

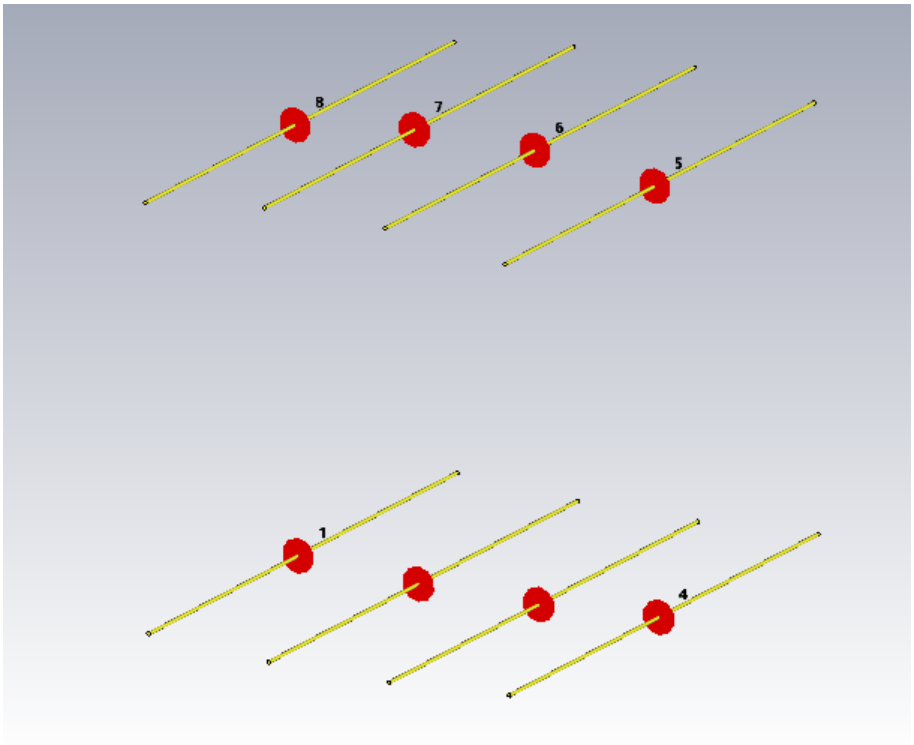

Figure 3.9: A CST view of the shortened dipole array. The feed ports are shown in red

The eight-channel dipole array comprised eight 30 cm long dipoles placed anteriorly and posteriorly. A CST view of the configuration is shown in Fig. 3.9. The summary of the array dimensions is shown in Table 3.11. The dipole feed was realised as a 50 Ohm

impedance discrete port that was connected to the tuning inductors. The matching was done using an LC balun. The tuning constituted offsetting the imaginary part of the dipole's impedance at the feed. The dipole feed diagram is shown in Fig. 3.10, where L_t are the tuning inductors. The required capacitances C and inductances L needed for matching were then computed following (3.2), where Z_0 is the impedance of the feed line (50 Ω) and Z_{in} is the feed point impedance of a dipole. The SAR efficiency shim was derived using an uncompressed Q matrix array.

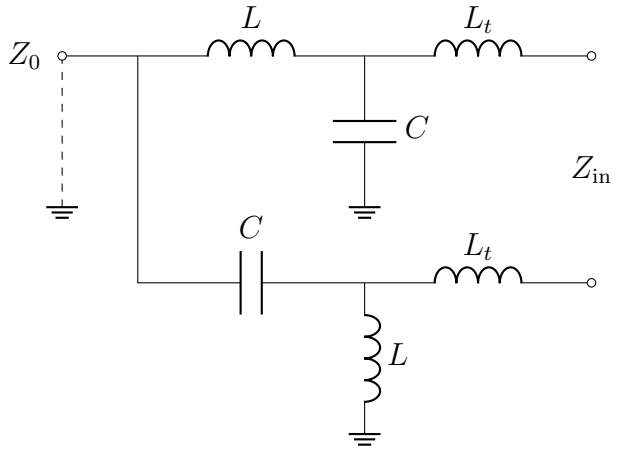

Figure 3.10: Dipole feed circuit diagram featuring the tuning inductors L_t and a lattice (LC) balun.

$$C = \frac{1}{\omega\sqrt{Z_0 Z_{\text{in}}}} \tag{3.2a}$$

$$L = \frac{\sqrt{Z_0 Z_{\text{in}}}}{\omega} \tag{3.2b}$$

Parameter	Value
Total length	30 cm
Feed gap	0.5 cm
Separation	7 cm
Distance to load	2 cm
Tuning inuctors	71-74 nH

Table 3.11: Summary of the dipole array dimensions.

3.5.2 Simulated performance

The simulated combined B_1 and SAR maps of the dipole array within the Duke digital body model are shown in Fig. 3.11. The summary of the array performance is provided in Table 3.12.

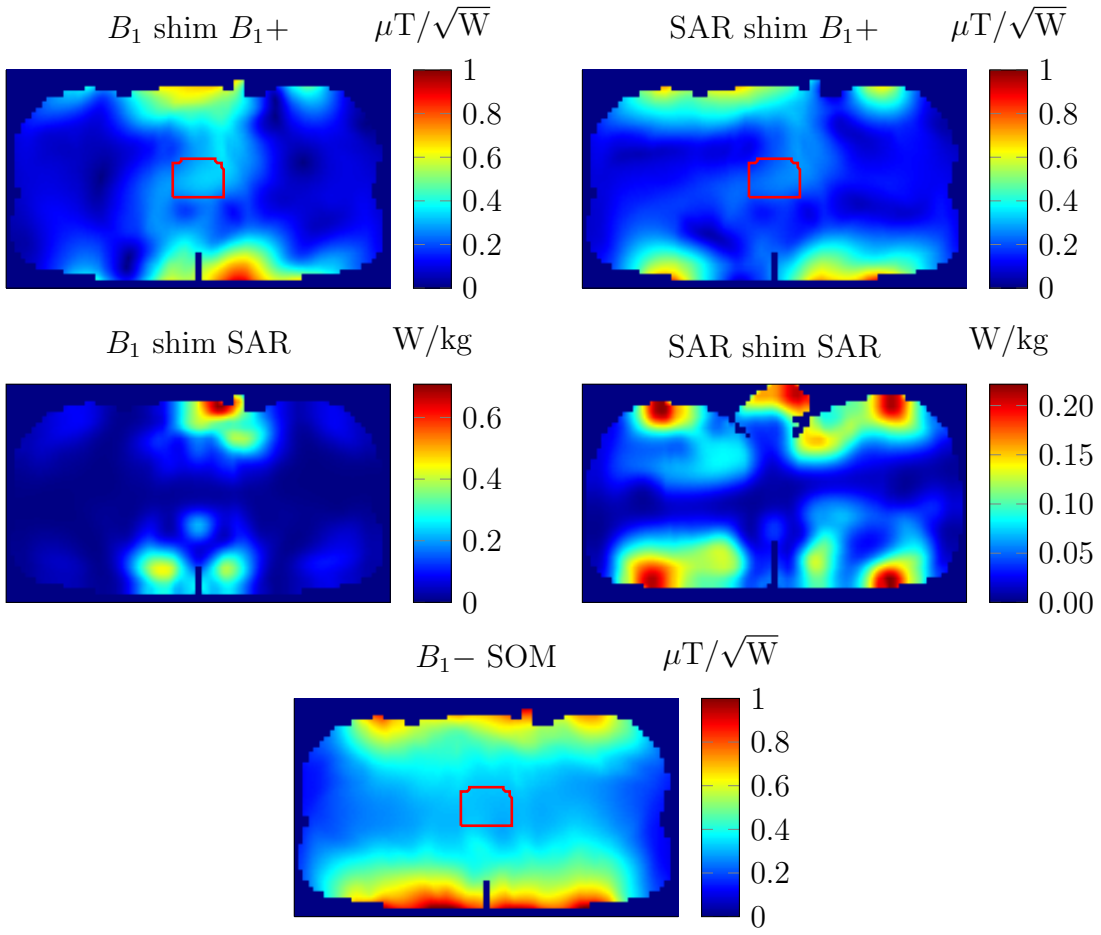

Figure 3.11: Simulated combined B_1 and SAR maps of the eight-channel shortened dipole array within the Duke digital body model using B_1 and SAR efficiency shims. The B_1 maps are shown for the central axial slice. The B_1- map corresponds to a sum of magnitudes of the per-channel B_1- patterns. The SAR maps are given for 1 W of input power. The SAR map is given for an axial slice where the hotspot occurs for the corresponding shim.

Shim	Mean B_1+, $\mu T/\sqrt{W}$	SAR, W/kg	SAR eff., $\mu T/\sqrt{pSAR}$	Mean B_1- SOM, $\mu T/\sqrt{W}$
B_1+	0.285	0.708	0.339	0.298
SAR	0.217	0.222	0.461	

Table 3.12: Performance summary of the eight-channel shortened dipole array within the Duke digital body model using the numerically derived prostate B_1+ and SAR efficiency shims. The peak SAR values are provided for 1 W of total input power. Also included is the mean B_1- sum of magnitudes (SOM) within the prostate.

3.6 Loop and shortened dipole comparison

A comparison of the simulated performance of the six-channel loop and eight-channel dipole arrays using a B_1+ efficiency and SAR shims is shown in Table 3.13.

Array	Shim	Mean B_1+, $\mu T/\sqrt{W}$	SAR, W/kg	SAR eff., $\mu T/\sqrt{pSAR}$	Mean B_1- SOM, $\mu T/\sqrt{W}$
6-channel loop	B_1+	0.291	0.555	0.390	0.299
	SAR	0.261	0.272	0.501	
8-channel dipole	B_1+	0.285	0.708	0.339	0.298
	SAR	0.217	0.222	0.461	

Table 3.13: Performance summary of the six-channel loop and an eight-channel shortened dipole arrays within the Duke digital body model.

The six-channel loop array demonstrated superior performance to the shortened dipole array in terms of both, B_1+ and SAR efficiencies. The receive sensitivity of both arrays within the prostate gland was nearly identical. Of note is the loop array's ability to maintain high B_1+ efficiency even when shimming for SAR reduction. The loop array is able to retain 89.6% of its nominal B_1+ efficiency when used with an SAR shim. In contrast, dipole's transmit efficiency falls off by 23.8% between the two shims.

3.7 Comparison with the arrays reported in the literature

The current state-of-the-art body arrays for 7 T feature dipoles or a combination of dipoles and other transmitter elements[12, 13, 16]. Presented in Table 3.14 is a comparison of the simulated transmit performance in the prostate within the Duke body model of the proposed six-channel loop array (6LA), a 16-channel combined loop and dipole array (16LD)[13], and a 10-channel fractionated dipole array (10DA)[13, 12]. The six-channel loop array surpasses the nominal B_1+ efficiency of both the 16LD array and the 10DA. The loop array SAR efficiency is comparable to 10DA and 16LD when the latter is employing a phase-only shim (the loops were driven at -7 dB power level compared to the dipoles), whilst maintaining a higher transmit efficiency. The nominal SAR performance of the 16LD array employing its full shimming capabilities is unsurpassed. The 6LA continued to offer a competitive performance when a phase-only shimming was used, retaining at least 98% of its nominal B_1+ efficiency in both shims, whilst only losing 4% of its nominal SAR performance. This is attributed to the placement of the loops, as all 6 are able to contribute sufficiently to the RF excitation within the prostate, making the amplitude adjustment unnecessary. This is in contrast to the dipole-based 8-10 element arrays, wherein only centrally positioned elements are able to induce sufficient excitation. Therefore, the amplitude adjustment is required to divert the power away from non-contributing elements to improve performance, resulting in high performance discrepancy between a phase-only and phase and amplitude shimming.

	Shim	Mean B_1+, $\mu T/\sqrt{W}$	SAR, W/kg	SAR eff., $\mu T/\sqrt{pSAR}$
16LD	B_1+	0.291	0.400	0.46
	SAR	0.237	0.122	0.678
16LD, phase-only	B_1+	0.251	0.236	0.518
10DA	B_1+	0.246	0.401	0.388
	SAR	0.202	0.142	0.536
10DA, phase-only	B_1+	0.217	0.265	0.421
6LA	B_1+	0.303	0.526	0.418
	SAR	0.275	0.279	0.520
6LA, phase-only	B_1+	0.300	0.522	0.415
	SAR	0.270	0.291	0.500

Table 3.14: Comparison of the 6LA with 16LD and 10DA. The data for the 16LD and 10DA is taken from Ertürk et al[13].

Chapter 4

Coil implementation

4.1 Housing

A simple housing design was used, comprising a hollow fibreglass box housing a bent fibreglass plate serving as a rest for the loops and TR switches. The CAD model with the requested tolerances was prepared and sent to Dr. Gunamony's contact in Germany for manufacturing. The interface box CAD was prepared and sent to Ogle Models (Birds Hill, Letchworth, Hertfordshire, United Kingdom) for 3D printing. The shape of the posterior half of the array followed the scanner's table profile. An interface box was devised for joining the two halves of the array. The complete coil arrangement, including an interface box, is shown in Fig. 4.1.

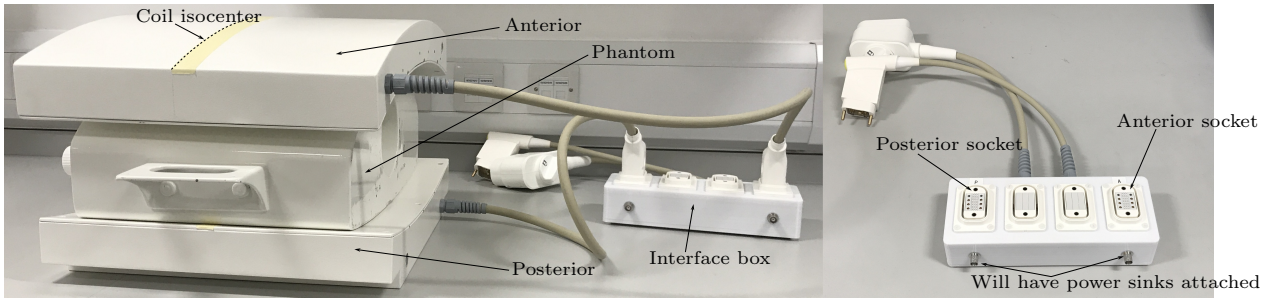

(a) Coil setup

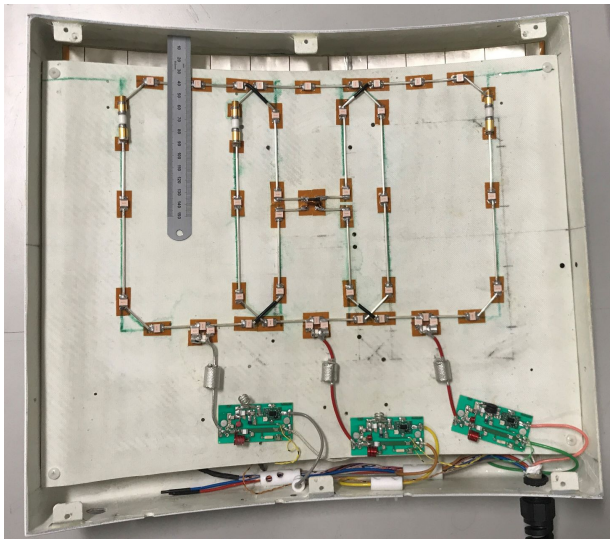

(b) Inside the anterior half

Figure 4.1: The array along with its interface box.

4.2 Electronics

4.2.1 Baluns

The baluns are necessary for preventing the outer layer of the coaxial cable's outer conductor from radiating by suppressing the common-mode currents. The baluns were realised as cable traps, whose schematic representation in shown in Fig. 4.2. A cable trap comprised a 3.5 mm diameter, three-turn solenoid made out of a piece of coaxial cable that was encased in a Teflon tube. The Teflon tube was then covered with PCB caps from both sides and wrapped in a conductive foil that was soldered to the PCBs. A capacitor was soldered between the foil and the coaxial cable's shield (outer conductor) to tune the trap. The capacitor values were determined empirically. The cable trap performance was determined by measuring the S_{21} parameter with a vector network analyser (VNA) between the capacitor terminals.

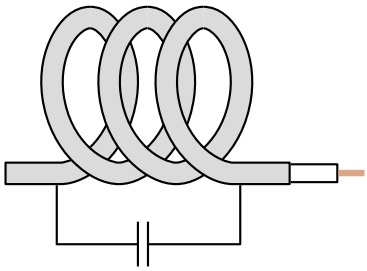

Figure 4.2: A schematic representation of a cable trap. A coaxial cable is wound to form an inductor and a capacitor is soldered onto its shield to create a parallel LC resonance circuit.

4.2.2 Local shield

The local shield featured a slotted design to suppress the eddy currents generated by the transmitting loops. The shield was realised as double-sided flexible PCB. The sheets available in the coil laboratory were not big enough to cover the required area, necessitating the use of two sheets. The shields were glued to the housing using a double-sided adhesive tape. The seam was covered with a silver strip and soldered.

4.2.3 Loops

The loops were built out of a 2 mm thick silver-coated copper wire. A loop-shaped cardboard cut-out was made to use as a contour for quick marking of the loop layout. Kapton soldering pads intended to hold the capacitors were glued to the fibreglass plate with a double-sided adhesive tape. The 7.5 pF capacitors along with a trimmer capacitor were then soldered onto the solder pads, and connected with pieces of silver wire that were shaped to follow the loop contour.

Upon finishing the construction of the loops, an L-network was soldered to each loop's feed, comprising 100 pF capacitors placed in series either side of the feed, followed by a parallel trimmer capacitor. The reflection (S_{11}) parameter of each loop was measured when the other loops were terminated with a 50 Ω load. The loop was then tuned and matched to 50 Ω by adjusting the tuning and matching trimmer capacitors. The S_{21} parameter measurements between the loop pairs were used to fine-tune the decoupling overlap. The tuning and matching procedures were performed with the phantom resting on the coil.

4.2.4 TR switches

The TR switch uses Dr. Shajan Gunamony's design[57]. The TR switch circuit diagram is shown in Fig. 4.3. The voltage DC_{IN} is supplied when the coil is transmitting, powering the diode D_R and creating a short (presenting a very low impedance) at A at 297.2 MHz, which looks like an open circuit following a transformation by a quarter-wavelength segment 6. The receive signal is blocked from reaching the RF power supply by a circuit comprising the diode D_T in parallel with a series LC circuit. The TR switches were assembled following the specification provided by Dr. Gunamony. The isolation of the receive and transmit paths was measured with a VNA. An S_{21} reading was taken between the coil input terminal and the RF power output terminal to gauge the transmit isolation. On the receive side, S_{21} was measured between the coil input terminal and the preamplifier input terminal when the diode D_R was powered on. The low-noise preamplifiers were soldered on after the isolation performance of the switches was found to be satisfactory.

The WMA7RD (Wantcom, Chanhassen, MN, USA) low-noise preamplifiers were then soldered onto the switch boards. The preamplifier gain was measured from an S_{21} parameter between the loop input terminal and the pre-amplifier output. The working DC voltage

of 10 V was supplied to the preamplifier at its output terminal using a bias tee. Bias tee is a circuit that is used to introduce a DC bias to an RF signal. The preamplifier gain measurement results are shown in Table 4.1. The pre-amplifier decoupling was measured with an overlapped H-field probe.

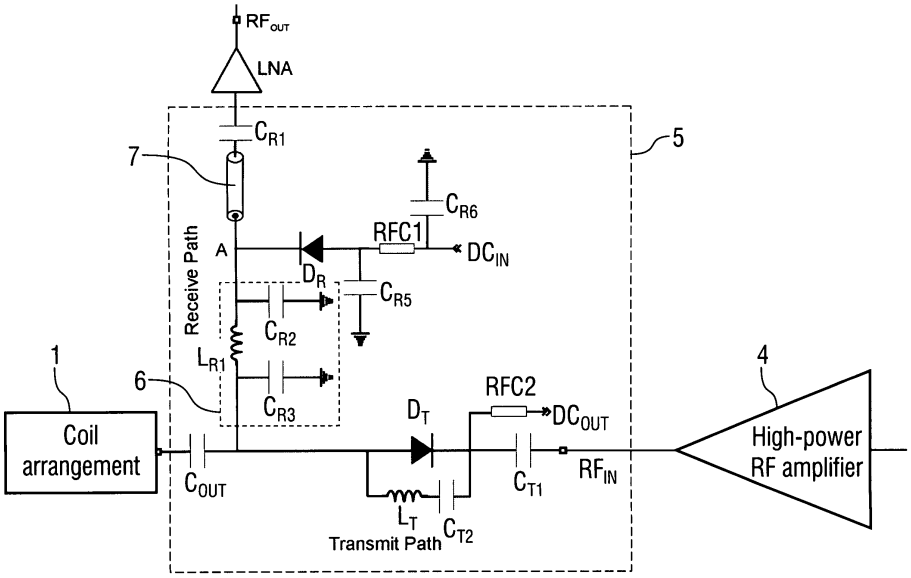

Figure 4.3: TR switch circuit diagram[57].

Channel	Gain, dB
Rx1	27.8
Rx2	27.6
Rx3	27.6
Rx4	27.6
Rx5	27.5
Rx6	27.6

Table 4.1: Preamplifier gain measurement result.

4.3 Cabling

The interface box was meant to be connected to the scanner using two cable assemblies: one connected to the transmit path, and the other connected to the receive path. The cables were affixed to the interface box by tightening them with the appropriately-sized cable strain reliefs. The interface box and the two arrays halves were interfaced with ODU-MAC Whilte Line modular connectors (ODU GmbH & Co. KG, Mühldorf am Inn, Germany). The sockets were populated with DC and RF receptacles that were crimped onto the DC wires and RF cables. The coaxial cables used in the receive chain were not of standard gauge. In order to connectorise them, their ends were soldered onto the pieces of standard-gauge coaxial cables that could be connectorised. The connections were checked with a multimeter to ensure the receptacles were put into the right spots.

The same procedure was repeated for the plugs that were attached to the cables going into the posterior and anterior halves of the array. The cables going into the housing were affixed to it with cable strain reliefs. The coaxial cables on the transmit path were trimmed incrementally to have the same phase going into a TR switch. The measurement of the transmit path phase and insertion loss are shown in Table 4.2.

Channel	Phase	Loss, dB
Tx1	0°	1.32
Tx2	-3.9°	1.39
Tx3	0.2°	1.31
Tx4	2.0°	1.32
Tx5	0.8°	1.40
Tx6	3.7°	1.35

Table 4.2: Per-channel transmit path phase and insertion loss measurements.

4.4 Scanner integration

Interfacing the coil to the scanner required preparing a set of configuration files along with a VOP file for SAR supervision in pTx mode. The VOP refers to the concept of virtual observation points, which was covered in-depth in subsection 2.5.4. The Q matrix array generation followed the same procedure as outlined in subsection 3.2.2, with the exception that a much finer export resolution was used to minimise the aliasing. The final Q matrix array contained the Q matrices from three different body models (Duke, Hugo and Rosalind), and from different anterior half positions. The Q matrix was compressed using a compression script provided by Siemens, which uses the compression algorithm outlined in subsection 2.5.4.

The VOP file generation is closely intertwined with the safety validation. Additional information about the VOP file generation is provided in Sec. 5.4, which deals with safety factor derivations.

Chapter 5

Coil validation

5.1 Phantom preparation

5.1.1 Phantom solution mixing

Equipment: hot plate with a stirrer, 2.5L conical flask, phantom, sugar, agar, salt (NaCl), benzoic acid, distilled water.

The phantom solution was mixed following a recipe described in Duan, Q. et al.[76], using the calculator hosted by the Advanced MRI (AMRI) laboratory of the National Health Institute (NIH) to procure the required ingredient quantities as well as the corresponding thermal and mechanical properties[77]. The phantom's volume measured 20 L. Due to a lack of an appropriately sized container, the mixing was done in batches of 2.5L in a conical flask sitting on a hot plate and using a magnetic stirrer. The water was heated up to 60 degrees as measured by a thermometer before the ingredients were added, sugar was added gradually. Each batch was mixed until the liquid appeared clear, with no visible residue suspended. Upon completing each batch, it was immediately poured into the phantom.

5.1.2 Phantom solution validation

Equipment: R&S ZND VNA, SPEAG DAK 12 open-ended coaxial probe, DAK analysis software, probe stand, 1.5L glass measuring pot filled with 1L of phantom solution, 1.5L glass measuring pot filled with 1L of distilled water, copper calibration strip, 99.7% isopropyl alcohol cleaner, tissues, thermometer, copper foil, nitrile gloves.

The phantom mixture's dielectric properties were measured with an open-ended coaxial probe connected to the VNA, which is a well-established non-destructive measuring technique for homogeneous samples in a tight contact with the probe[78, 79]. An open-ended coaxial line connected to the VNA is placed in a tight contact with material under

test (MUT) and the reflection coefficient (S_{11}) of the setup is measured and converted to permittivity using a suitable model[80, 81]. The VNA readings are calibrated with respect to the probe aperture before the measurements are taken, which is performed using a sample with known dielectric properties to serve as the load condition. The open condition is calibrated in air and a short is measured when the inner and outer conductors of the probe are shorted with a patch of highly conductive metal.

Sweep range	290-309.9 MHz
Samples	100
Averages	10

Table 5.1: VNA measurement parameters.

Before setting up the probe, the VNA was let to warm up for 30 minutes as per manufacturer's recommendations[81]. The VNA was then connected to the local area network (LAN) via an Ethernet cable to enable data transfer to the laboratory computer hosting DAK analysis software. Once the VNA was interfaced to the analysis software, measurement parameters were defined as provided in Table 5.1. The equipment was handled wearing nitrile gloves to avoid grease stains on the probe. The probe was cleaned with an IPA and positioned on the holder, and calibrated as instructed by the probe manufacturer[80]. An open circuit condition was measured in air, a short was measured by terminating the probe with a copper strip that was cleaned with an IPA. The temperature of the distilled water was measured and entered into the DAK software before positioning the pot such that the probe end is fully submerged. The surface of the probe was inspected for the presence of air bubbles before taking the load measurement. The distilled water container was then removed and the probe was gently pat-dried with a tissue. A temperature of the phantom mixture was recorded and entered into the software before commencing the measurements. Adequacy of the container's dimensions was assessed by placing a copper foil on the side of the container and noting that the measurement is not significantly affected. After moving the foil out of the way, the sample measurement was recorded. The sample's homogeneity was assessed by taking three additional measurement at different locations within the sample, which was done by adjusting the container's position. The measurements were exported into an Excel sheet for use in defining the phantom material within the EM simulation software.
The measured dielectric properties of the small body phantom solution at 297.2 MHz are summarised in Table 5.2.

σ	0.6 S/m
ϵ'	55.8
ϵ''	35.9
$\tan\delta$	0.64

Table 5.2: Dielectric properties of the small phantom solution measured at 297.2 MHz.

5.2 B1+ mapping

5.2.1 Mapping procedure

The initial B_1+ mapping was performed using a *tfl_b1map* sequence[82]. The resulting FA map was converted into a B_1+ efficiency map ($\mu T/V$) using the flip angle equation (5.1), where τ is the duration of the reference pulse and V_{ref} is the reference voltage used to produce the map. Single channel maps were acquired using a *tfl_rfmap* sequence[83].

$$B_1+ = \frac{\alpha}{\gamma \tau V_{\text{ref}}} \tag{5.1}$$

Later in the project, the combined B_1+ mapping was done using an actual flip angle (AFI) mapping technique[84], which is considered a "gold standard" approach for B_1+ mapping. The methods utilises a ratio of the two GRE signals acquired at different repetition times to compute the flip angle. The AFI is a generalisation of the B_{1+} mapping method described by Pan et al.[85]

The method described by Pan et al. assumes the repetition time between the two signal acquisition TR_1 to be $<<\text{T}_1$, and further assumes that TR_2 is long enough for the magnetisation vector $\vec{M}_0$ to return to the equilibrium. Following the initial flip by an angle θ, the available GRE signal is given $S_1 = M_0 \sin\theta$. Since the TR_1 is negligible compared to the T_1 relaxation constant, the available net magnetisation for the next signal acquisition is $M_0 \cos\theta$, determined entirely by the initial flip. Consequently, the second GRE signal acquired following the second excitation is given by $S_2 = M_0 \cos\theta \sin\theta$. The flip angle θ can then be inferred from the ratio $S_2/S_1 = \cos\theta$, and is given by $\theta \approx \arccos S_2/S_1$. After the time TR2, the sequence is repeated.

Meanwhile, the AFI considers the case where the relaxation effects are non-negligible $\text{TR}_1 <\text{TR}_2 <\text{T}_1$, but assumes that the sequence is spoiled after each $\text{TR}_{1,2}$. Instead of relying on full relaxation, the method analyses the established pulsed steady state. The available magnetisation M_{z1} following TR_2 is given by

$$M_{z1} = M_0 \frac{1 - E_2 + (1 - E_1)E_2 \cos\theta}{1 - E_1 E_2 \cos\theta} \tag{5.2}$$

, whilst the available magnetisation M_{z2} following TR1 is

$$M_{z2} = M_0 \frac{1 - E_1 + (1 - E_2)E_1 \cos\theta}{1 - E_1 E_2 \cos\theta} \tag{5.3}$$

, where $E_{1,2} = \exp\{-\text{TR}_{1,2}/\text{T}_1\}$. Since the transverse phase coherence is destroyed between each $\text{TR}_{1,2}$, the resulting GRE signals are given by

$$S_{1,2} = M_{z1,2} \exp\{-\text{TE}/\text{T}_2^*\} \sin\theta \tag{5.4}$$

, and the signal ratio is expressed as

$$r = S_2/S_1 = \frac{1 - E_1 + (1 - E_2)E_1 \cos\theta}{1 - E_2 + (1 - E_1)E_2 \cos\theta} \tag{5.5}$$

If the TR_1 and TR_2 are short relative to T_1, the first-order Taylor expansions around 0 of the exponent terms can be used to produce the approximate expression for the signal ratio r:

$$r \approx \frac{1 + n\cos\theta}{n + \cos\theta} \tag{5.6}$$

Here, $n = TR_2/TR_1$. Rearranging the approximate expression for r yields the flip angle:

$$\mathrm{FA} \approx \arccos\frac{rn - 1}{n - r} \tag{5.7}$$

A series of the GRE magnitude and phase images acquired at their respective TR values were first combined to produce complex maps and then converted into a flip angle map using (5.7). The FA map was then converted into a B_1+ efficiency map (per volt) using (5.8), where τ is the duration of the reference rectangular pulse and α_n is the nominal prescribed flip angle.

$$B_1+ = \frac{\frac{\pi}{\gamma\tau}}{\frac{\alpha_n}{\mathrm{FA}}V_{\mathrm{ref}}} \tag{5.8}$$

The S-parameters acquired from the scanner were used to set the matching within the simulation setup. The per-channel B_1+ maps were then exported and scaled down by their respective cable attenuation factors before combining.

5.2.2 Results and discussion

Channel	Amplitude	Phase
Tx1	0.4082	-163°
Tx2	0.4082	86°
Tx3	0.4082	-7°
Tx4	0.4082	-158°
Tx5	0.4082	30°
Tx6	0.4082	-4°

Table 5.3: Shim used to acquire the AFI data.

The shim that was used to acquire the B_1+ data is presented in Table 5.3. The measured and simulated combined and per-channel B_1+ maps are shown in Fig. 5.1. The measured combined B_1+ within the ROI centred around the central shimming voxel was found to be 6.82% weaker relative to the simulations (mean values of 35.1 and 32.9 nT/V, respectively). There is a phase mismatch in the single channel maps further away from

the centre of the phantom. The likely reason is a lack of signal due to the B_1+ pattern of the employed shim.

The measured combined B_1+ maps presented in this section appear weaker than the results presented in subsection 5.5.2, which were reacquired as part of the coil's safety re-approval process which sought to make the safety factors less conservative. The most likely reason for this is the coil's tuning, as the maps presented in this section were acquired on a phantom when the coil was tuned on the body, contrasted with the combined map presented in, where the coil was tuned to the phantom. The torso phantom on the Glasgow site doe not approximate well how the body loads. The thesis author was also unaware that the $S-$parameters reported by the scanner did not take into account the scanner cable losses.

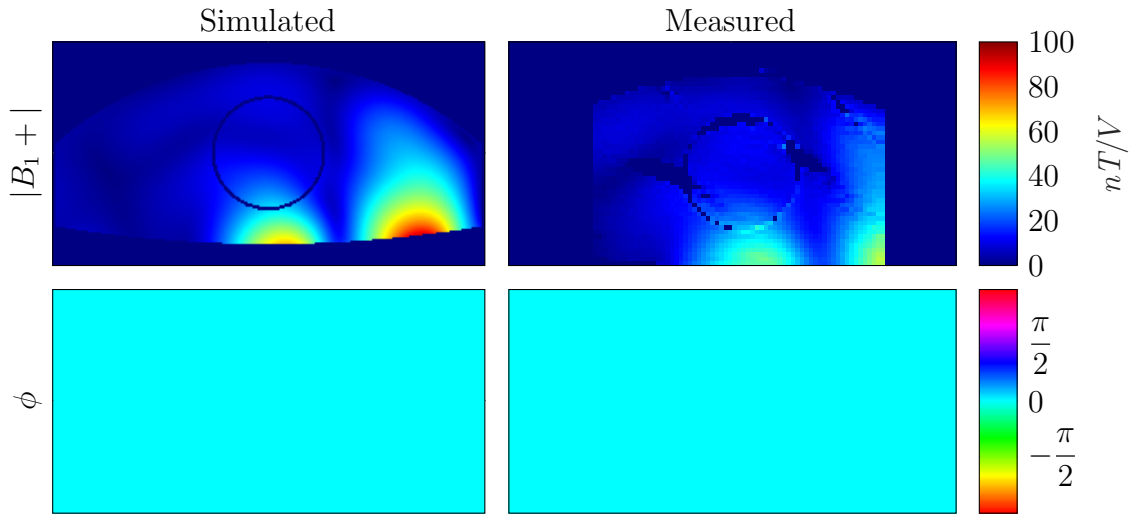

(a) Tx1

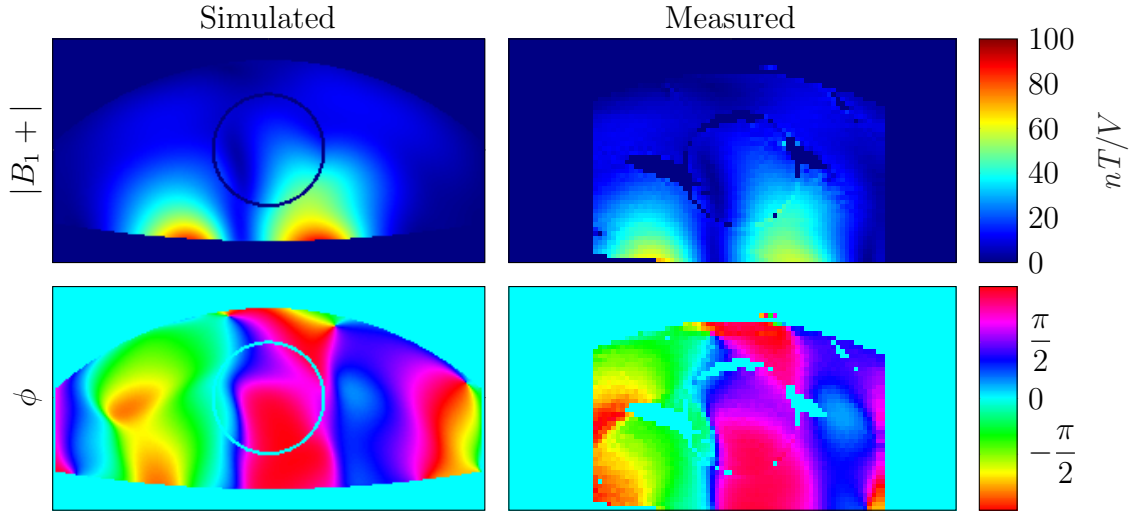

(b) Tx2

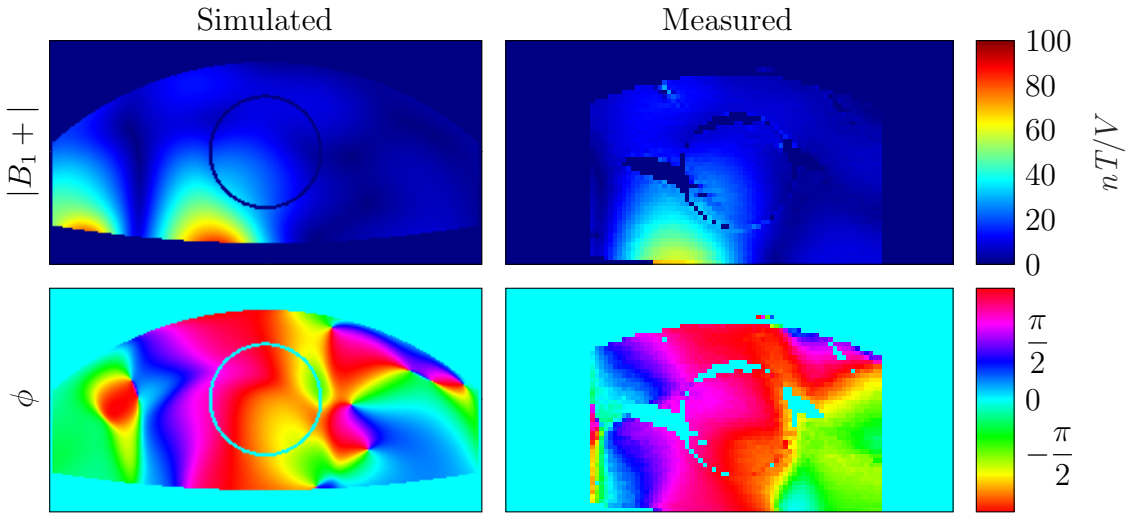
Simulated
Measured
$|B_1+|$
ϕ
100
80
60
40
20
0
nT/V
$\frac{\pi}{2}$
0
$-\frac{\pi}{2}$

(c) Tx3

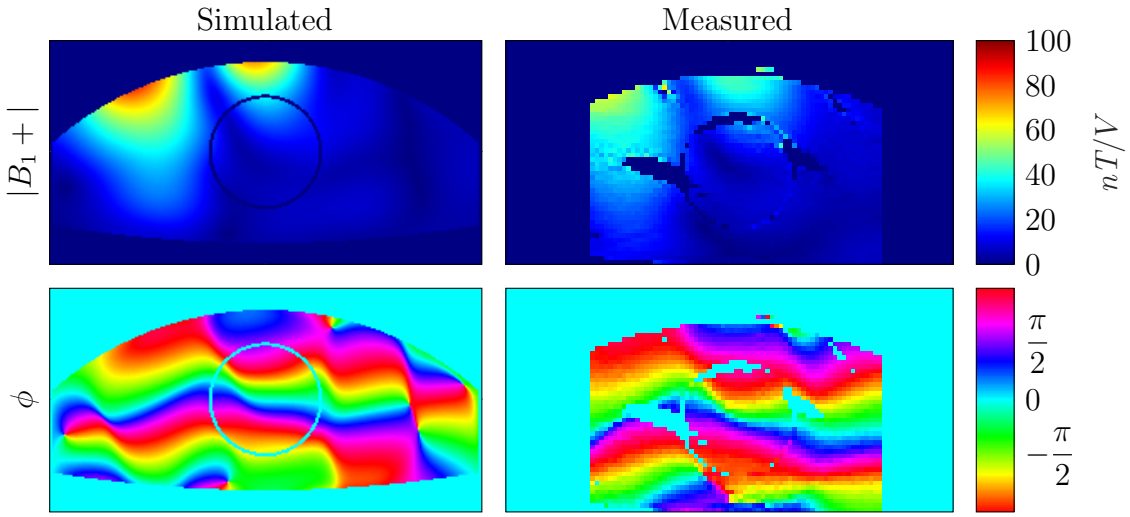
Simulated
Measured
$|B_1+|$
ϕ
100
80
60
40
20
0
nT/V
$\frac{\pi}{2}$
0
$-\frac{\pi}{2}$

(d) Tx4

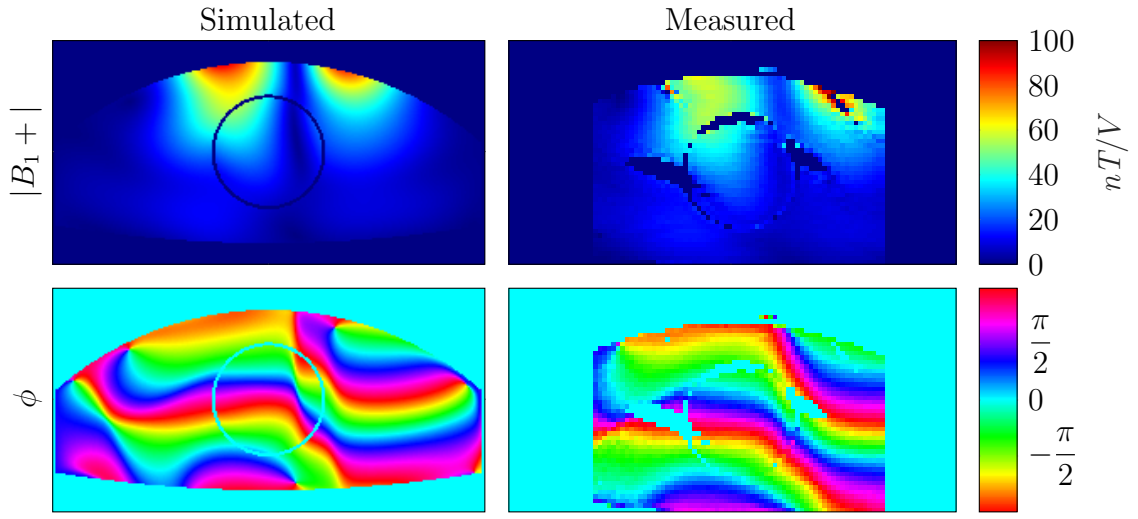

(e) Tx5

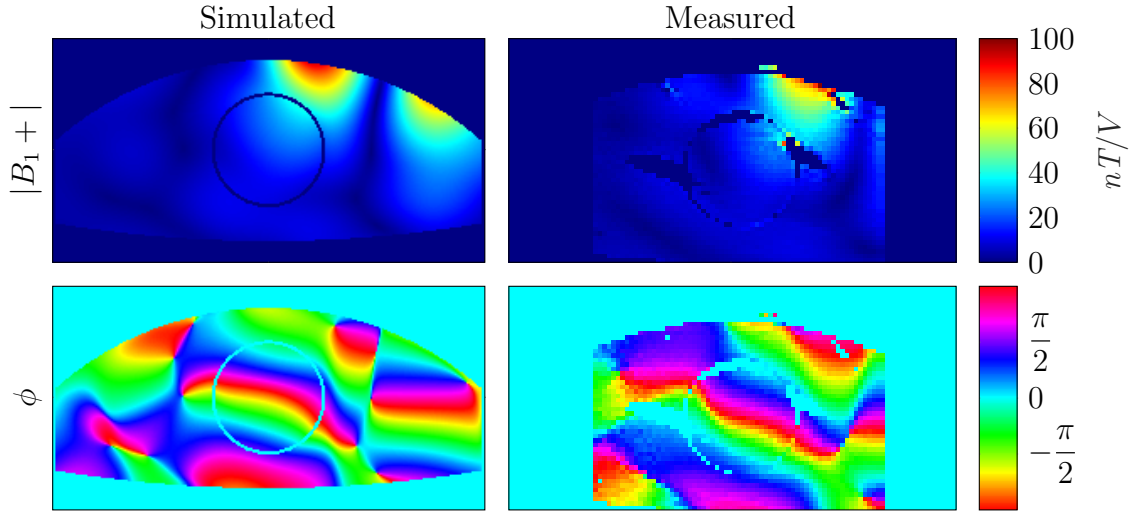

(f) Tx6

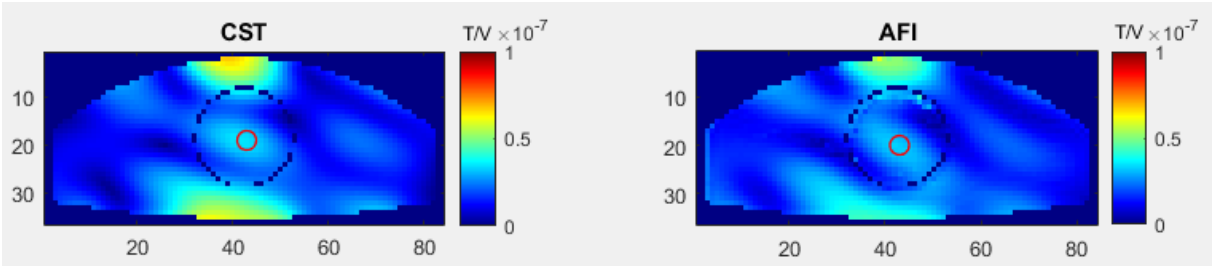

Figure 5.1: Phantom B_1+ data comparison between the simulations and the measurements. Single channel phase maps are referenced to Tx1. Scanner's combined B_1+ map was reconstructed from the AFI data. Encircled in red is the region where the mean and maximal B_1+ magnitude values were compared.

5.3 Temperature mapping

5.3.1 Measurement procedure

The temperature mapping of the array (data acquisition and results post-processing) was performed by an on-site principal MR safety expert, with the aid of the thesis author

(measurement setup and provision of the simulated temperature change maps). The temperature mapping was performed using the methods of PRF thermometry, mentioned in subsection 2.5.5. Additionally, two optic fibre temperature probes were positioned anteriorly and posteriorly for the PRF measurement correction. Two holes were drilled in the phantom to accommodate the probes that were then sealed with a hot glue. At the start of the experiment, a T_2-based probe localiser sequence was run to pinpoint the probe position, and a phase map was acquired with a GRE sequence as a baseline measurement before any heating took place. Afterwards, a sequence was run to induce the heating, and another phase map was acquired with a GRE sequence. The SAR conversion factor was considerably reduced for this experiment to not be limited in the amount of power that can be used for heating.

5.3.2 Temperature change simulation

ρ	1263.04 kg/m^3
C	2838.19 J/(kg×K)
k	0.415907 W/K/m

Table 5.4: Summary of the large phantom's thermomechanical properties taken from the NIH phantom recipe calculator webpage.

The large phantom's thermomechanical properties (taken from the NIH phantom recipe calculator webpage) are provided in Table 5.4. The simulated temperature change maps were produced from the SAR maps per 1W of input and did not take into account the thermal diffusion. The conversion was done according to (5.9), where SAR denotes the SAR per 1W of input power with cable and mismatch losses taken into account, and P and t are the heating sequence power and duration. The mismatch losses were taken from the S-parameters values reported by the scanner.

$$\Delta T = \frac{\mathrm{SAR} \cdot Pt}{C} \tag{5.9}$$

5.3.3 Results and discussion

The simulated and measured temperature change maps for 22.73 kJ of total applied energy (33.4 W applied over the course of 340 seconds) are shown in Fig. 5.2. The simulated and measured maps are in a good agreement. The simulated results show a slightly increased temperature rise of 1.15 K, compared to a measured rise of 1 K.

The measurement results are affected by the coil positioning uncertainty and partial volume effect associated with the chosen voxel size. The measurement in the anterior half was skewed by the presence of an air gap within the phantom from a spillage that was not refilled (the spillage occurred months prior to the experiment and is not related to it). On the simulation side, the effects of thermal diffusion were not accounted for. There

is an additional uncertainty with respect to the phantom's thermomechanical properties, as those values were acquired from the estimations and were not measured.

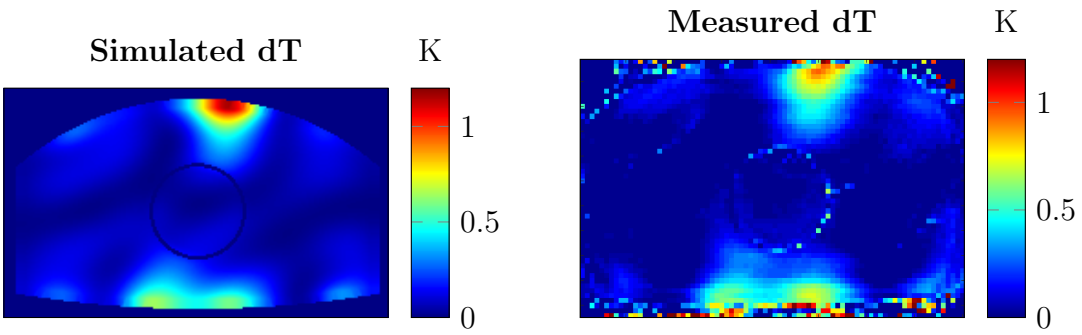

Figure 5.2: Simulated and measured temperature rise maps within the central axial slice of the phantom.

5.4 Safety assessment

5.4.1 Subject variability

The influence of subject variability on SAR was studied by simulating the coil loaded with three different digital body models: Duke, Hugo and Rosalind. For Duke, additional simulations were performed with a varying anterior half position. The assessment used the shim given in Table 5.3. A summary of the digital body models is provided in Table 5.5. The subject SAR variability was only assessed for a prostate shim (derived for the Duke digital body model). The loop elements were tuned and matched to better than -40 dB in each simulation. The SAR results for the combined excitations were computed in CST.

	Resolution, mm	Sex	Mass, kg	Height, cm	BMI	Age, years
Duke	5	M	70.2	177	22.4	34
Hugo	5	M	103	180	31.7	38
Rosalind	2	F	54	164	20	24

Table 5.5: Duke, Hugo and Rosalind digital body model summary.

The resulting SAR value table is shown in Table 5.6. The lowest SAR was observed within the Hugo digital body model. The highest SAR was observed within the Rosalind digital body model. The subject variability factor was preliminarily found to be 1.56.

	Duke, -10 cm	Duke, -5 cm	Duke, 0 cm	Duke, +5 cm	Duke, +10 cm	Duke, +15 cm	Rosa-lind, 0 cm	Rosa-lind, +10 cm	Hugo, -0 cm
SAR, W/kg	4.88	5.03	5.16	5.20	5.15	5.00	5.72	4.48	3.68
x (L-R)	-41.0	-41.0	-41.0	-41.0	-41.0	-41.0	25.0	30.0	46.0
y (P-A)	45.0	45.0	45.0	45.0	45.0	45.0	177.5	181.5	257.5
z (F-H)	27.5	27.5	27.5	28.5	28.5	28.5	42.0	81.7	17.5

Table 5.6: Simulated peak local 10 g SAR results summary for different digital body models and positions. Also included are the hotspot x,y,z-coordinates (with an equivalent subject reference frame: (L)eft-(R)ight, (P)osterior-(A)nterior, (F)eet-(H)ead).

The SAR hotspot containing peak SAR values are shown in Fig. 5.3. The highly-conductive muscle tissue and organ contents were shielded by the excess fat layer within the Hugo digital body model. In contrast, the SAR hotspot was localised to the small intestine lumen within the Rosalind digital body model. The conductivity of the small intestine lumen used in the simulation is 2.38 times higher than that of the muscle tissue. The organ was located very close to the transmitters, and ended up dissipating a large amount of RF energy. The SAR within the Rosalind digital body model went down considerably when the coil's anterior half was slid 10 cm towards the head, away from parts of the loop that generate the most SAR. The hotspot within the Duke digital body model was confined to the gluteal muscle tissue.

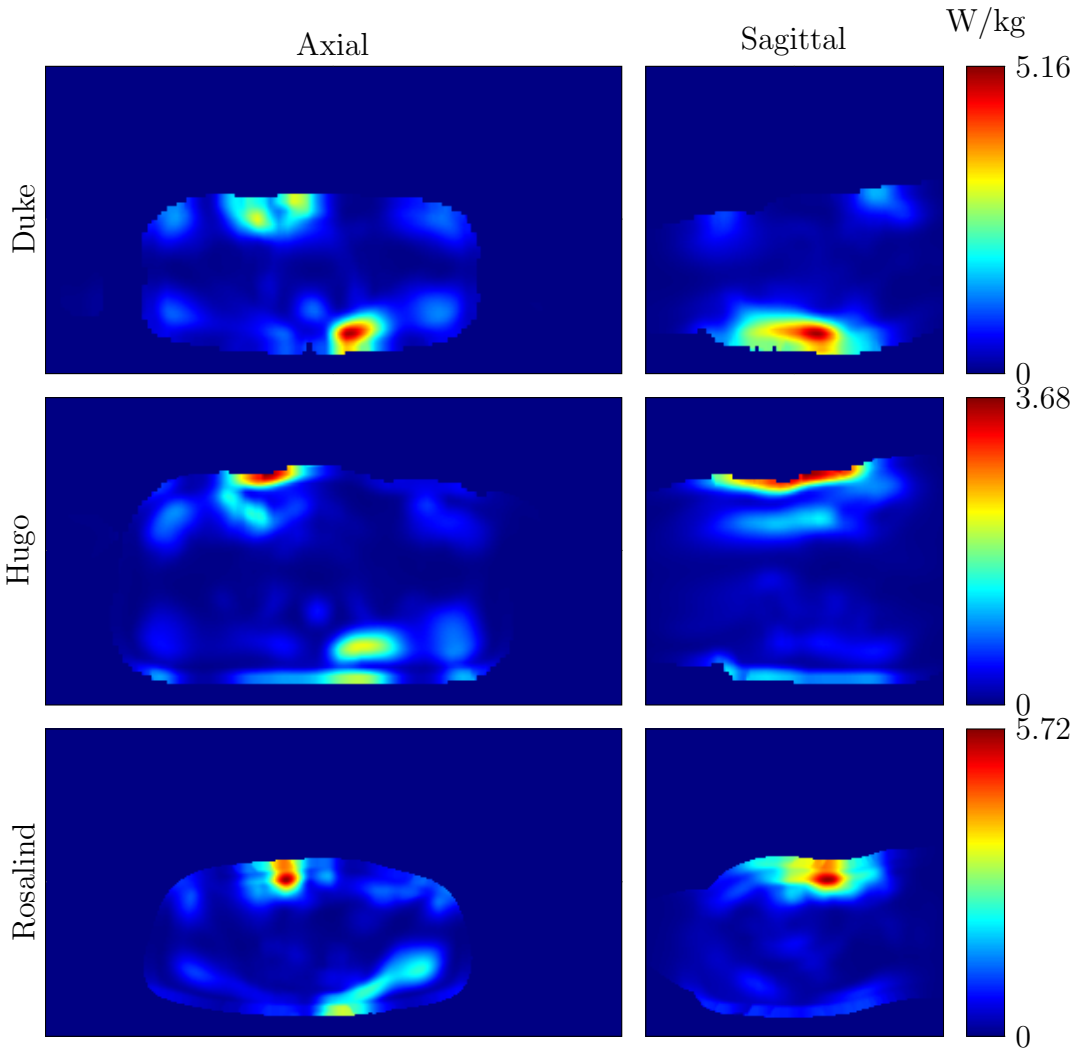

Figure 5.3: Axial and sagittal slices of the simulated SAR maps within the Duke, Hugo and Rosalind digital body models going through the centres of the hotspot. The colour bars are scaled to the peak SAR values of their respective models.

5.4.2 VOP file generation

The SAR data necessary for the Q matrix generation was exported for the nine simulations that were performed to assess the influence of subject and coil position variability on the induced peak local SAR. The necessary exports were done at a resolution that followed the simulation mesh size. The Q matrix generation process otherwise followed the steps outlined in subsection 3.2.4. The difference between the SAR reported in CST for the prostate shim and the SAR computed with the Q matrices was within 1.8%. The Q matrices from the nine simulations were concatenated into a single file and compressed with a Siemens script that uses the compression algorithm outlined in subsection 2.5.4.

5.4.3 SAR conversion factor

The safety factors that were used to make up the final conversion factor between the supplied power to the coil and the resulting peak SAR are listed in Table 5.7. The inter-

subject SAR variability factor k_{sub} was taken from the literature. Although multiple body models and coil positions were simulated, yielding an appreciably lower factor of 1.6, it was deemed best to err on the side of caution due to a lack of experience in dealing with UHF body arrays on the Glasgow 7 T site. The safety factor k_{B_1} of 1.25, although B_1+ is only indirectly proportional to SAR, was introduced as another precaution, with its value corresponding to a discrepancy between the simulated and measured B_1+ magnitude values at the phantom's periphery. Although the temperature maps agree within 15% between the measurements and simulations, the B_1+ discrepancy was used instead as it was more conservative. The cable gain factor k_{cable} was picked to be the lowest measured voltage gain between the coil plug and the matching network. The additional overestimation of 20% was added as per the safety approval board's requirement. The resulting conversion factor (or k-factor) ended up being nearly identical to the worst-case SAR performance (1.95 W/kg for 1 W of input power observed within Rosalind) of all the digital body model simulations that were considered.

Factor	Value	Description
k_{sub}	1.8	Inter-subject variability factor advised to be used by the safety approval board.
k_{cable}	0.85	Coil cable voltage gain.
k_{scanner}	1.16	Scanner-related measurement uncertainty factor.
k_{all}	1.2	General 20% overestimation.
k_{B_1}	1.25	The discrepancy observed between the simulated and measured B_1+ magnitude at the phantom's periphery. Taken in place of a temperature mapping result as it was more conservative.
k_{final}	2.67	The final factor, computed as a product of the above factors.
$\text{pSAR}_{10\text{g}}$	0.72 W/kg	Peak $\text{SAR}_{10\text{g}}$ value at 1 W input power before the application of the final factor.
k	1.93	SAR conversion factor set in the coil file, corresponding to peak $\text{SAR}_{10\text{g}}$ value at 1 W input power after the application of k_{final}.

Table 5.7: Summary of factors used to derive the SAR conversion factor.

The k-factor SAR conversion applies to the case when the coil uses a static, pre-defined shim. The SAR supervision in a pTx mode is done with a VOP file. The safety factors applied to the VOP included a Siemens error term, followed by scaling the resulting VOP such that the SAR computed from the VOP using a pre-defined static shim matched the k-factor estimation.

5.4.4 Discussion

The described safety assessment had numerous flaws. One minor issue is concerned with the CST field export method. The built-in method enforces linear interpolation. Therefore, if the fields are exported on a grid that does not align with the simulation mesh, the exported values are always understated. The export method offers an option to export the results on a grid that follows the mesh density. However, it was discovered that the export takes place on a dual grid, and not the primary grid where the computed simulation results are defined, leaving the interpolation problem unresolved. The discrepancy between the SAR values exported using the built-in CST method and the "ground truth" was in the range of 1-6%. Although negligible, it still constitutes an unnecessary source of error. The application of the subject variability factor to a model which already exhibits the worst-case performance for the shim in question is unnecessarily restrictive when the coil is used in sTx compatibility mode. The cable gain factor was defined as a voltage gain, whilst a power gain (square of the value) should be used instead, since the SAR is dependent on the input power and the k-factor is applied to the supplied power. Determining the subject variability factor for pTx warrants a more thorough investigation.

The revised safety procedure that addresses the shortcomings of the initial assessment is described in the subsequent section. The revised assessment was not implemented until after the project ended.

5.5 Revised safety assessment

5.5.1 Subject variability estimation

The subject variability factor was defined as the largest achievable ratio of peak SAR induced in the examined model with respect to some reference model. The procedure for the determination of the subject variability factor comprised the following steps:

- Coil simulation for a range of digital body models
- Generation of the model Q matrices
- Compression of the model-specific Q matrices into the VOPs with an upper bound of 5% on the overestimation of the worst-case λ_{max} for a given Q matrix cluster.
- Performing constrained optimisation to find a shim for which the peak SAR in the examined model exceeds the SAR induced in the reference model the most:

- Initialise 100 uniformly distributed random shims
- Minimise the function $\mathrm{pSAR}\left(\mathrm{VOP}_{ref}\right)/\mathrm{pSAR}\left(\mathrm{VOP}\right)$ starting from one of the randomly generated shims as the initial guess. VOP_{ref} refers to the VOPs of the reference model and VOP are the VOPs of the models being compared to the reference model.

- Compute the subject variability using the Q matrices for a worst-case variability vector determined from the VOPs

Three digital body models were used to assess the subject variability of the RF coil: Duke, Hugo and Rosalind. The summary of the model parameters is given in Table 5.8.

	Resolution, mm	Sex	Mass, kg	Height, cm	BMI	Age, years
Duke	5	M	70.2	177	22.4	34
Hugo	5	M	103	180	31.7	38
Rosalind	2	F	54	164	20	24

Table 5.8: Duke, Hugo and Rosalind digital body model summary.

Only one coil position corresponding to a prostate scan was simulated in each case. The summary of subject variability results for each model used as a reference is given in Table 5.9. Rosalind was chosen as a reference model for the final VOP compression, as the resulting subject variability is reduced compared to other models due to Rosalind being the most conservative model of the three to start with. The largest SAR variability when using Rosalind as a reference was observed between it in Hugo.

	Duke	Hugo	Rosalind
Variability	4.23	4.62	2.09

Table 5.9: Dependence of the worst-case subject variability factor on the choice of reference model.

5.5.2 Simulation mismatch

The simulation mismatch factor was computed as a relative (positive) per-voxel B_1+ error (5.10) within the central phantom slice that is not exceeded for 99.9% of the voxels within the slice[86]. The assessment was limited to the regions of the phantom where the simulated B_1+ magnitude was no less than 30% of the maximal B_1+ magnitude within the slice.

$$\frac{\left(|B_1^{\mathrm{AFI}}+| - |B_1^{\mathrm{CST}}+|\right)}{\max\{|B_1^{\mathrm{CST}}+|\}} \tag{5.10}$$

The summary of the AFI sequence acquisition parameters used for the comparison is listed in Table 5.10, and the shim amplitude and phase is specified in Table 5.11. The comparison results are shown in Fig. 5.4. The simulated B_1+ maps were scaled down by 2.9 dB to account for the coil cable (1.3 dB) and scanner (1.6 dB) losses. The relative positive difference did not exceed 23.3% for 99.9% of the voxels within the slice. The mean relative difference was found to be $5.5 \pm 0.07\%$.

TR1/TR2	10/100 ms
TE	2.04 ms
FOV	$400 \times 200 \times 192$ mm
Voxel size	$4 \times 4 \times 4$ mm
Phase encoding	AP
Orientation	Sagittal
Flip angle	45°
Ref. voltage	300 V

Table 5.10: Summary of the AFI sequence acquisition parameters.

Channel	Amplitude	Phase
Tx1	0.4082	-163°
Tx2	0.4082	86°
Tx3	0.4082	-7°
Tx4	0.4082	-158°
Tx5	0.4082	30°
Tx6	0.4082	-4°

Table 5.11: Shim used to acquire the AFI data.

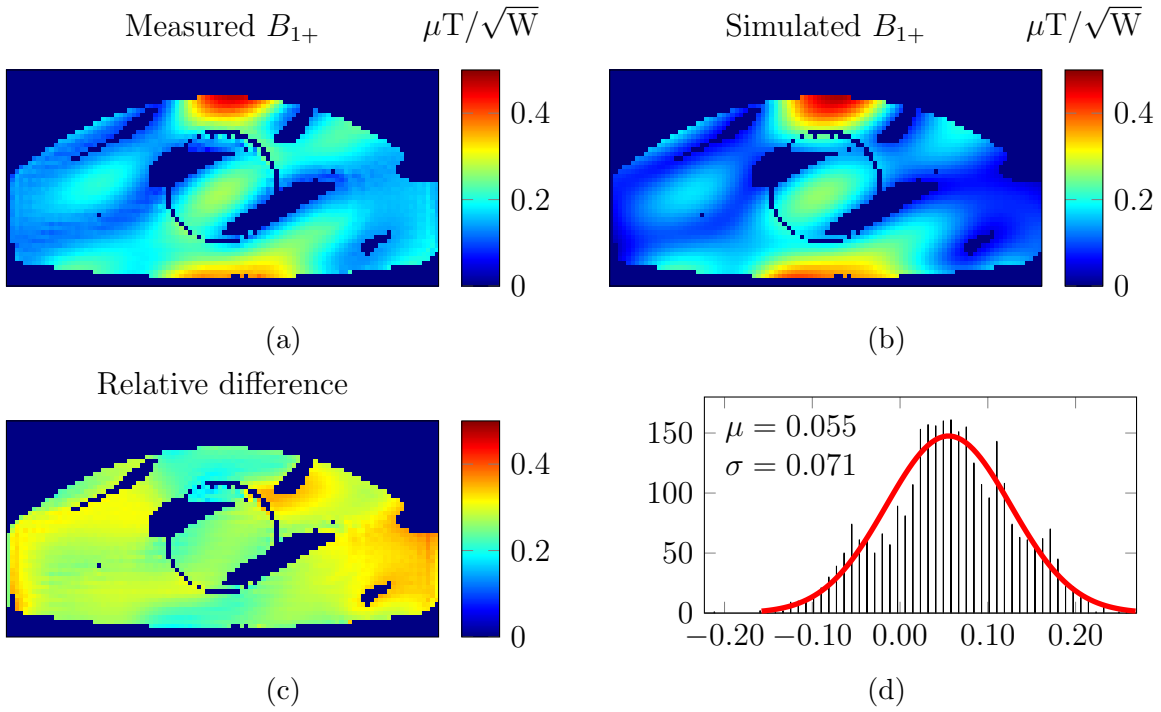

Figure 5.4: (a) Measured and (b) simulated B_{1+} maps within the central phantom slice along with their (c) relative difference map (with respect to the peak simulated B_{1+} within the slice). The assessment was limited to the voxels within the phantom where the simulated B_{1+} was at least 30% of the peak simulated B_{1+} within the slice. The histogram of the difference map is shown in (d).

5.5.3 SAR conversion factor derivation

The SAR conversion factor (or k-factor) is a linear coefficient used to convert the input power to peak SAR when the coil is used with a fixed, pre-defined shim. It was derived by multiplying the subject variability factor, the setup mismatch factor and the cable gain with the CP mode (equal channel amplitudes, 0°, -90°, -180°, 0°, -90°, -180°phase) peak SAR observed in the Rosalind digital body model. The summary of the SAR conversion factor and its constituents is provided in Table 5.12.

Parameter	Value	Description
Subject variability	2.09	Worst-case peak SAR variability numerically derived from for the Hugo, Duke and Rosalind simulations with Rosalind acting as a reference model.
Setup mismatch	1.24	Relative B_1+ error that is not exceeded for 99.9% of the voxels within the central phantom slice.
Cable gain	0.74	Linear power gain factor computed from the coil cable loss of 1.35 dB.
Peak SAR, W/kg	0.66	Peak SAR observed within Rosalind digital body model using a CP shim driven with 1 W of input power.
k-factor	1.27	The final SAR conversion factor computed by multiplying the above factors together.

Table 5.12: Summary of the parameters involved in composing the k-factor.

5.5.4 VOP file generation

To use arbitrary shims on the scanner, a VOP file is needed for real-time SAR estimation. The same factors used to derive the SAR conversion factor (subject variability, simulation mismatch and cable gain) for the sTx compatibility mode were applied to the array of Q matrices belonging to Rosalind digital body model. Two additional factors were incorporated to account for the scanner channel driving phase and amplitude measurement uncertainty, which introduced an additional overestimation of at least 23%. The array of 16 023 688 Q matrices was then compressed using the Eichfelder and Gebhardt algorithm with a 6% upper bound on overestimation of the worst-case SAR for a given Q matrix cluster. This resulted in an array of 191 VOPs. The resulting VOP was validated by checking that for every Q matrix there was a VOP such that the difference $P = (\mathrm{VOP} - Q)$ was positive semi-definite (every eigenvalue of $(\mathrm{VOP} - Q)$ is non-negative). This condition guarantees that the SAR is never underestimated.

5.5.5 Discussion

The safety factors can be reduced further by adopting the sum of squares approach to combining the setup mismatch and subject variability, as the two quantities can be as-

sumed to be uncorrelated[86]. However, because the setup mismatch was only assessed for a single shim, it was decided to retain the multiplicative approach. The subject variability was derived based on the assumption that the observed worst-case variability can potentially occur for all shims. However, for an sTx compatibility mode shim with equal channel amplitudes, the analysis could have been limited to phase-only shims. Furthermore, given that the proposed six-channel loop array demonstrates an ability to retain its nominal performance even when phase-only shims are considered, the coil can be limited to phase-only shimming in pTx without much compromise to its utility (at least as far as the static shimming is concerned, dynamic pTx performance was not assessed at the point the thesis was submitted). Consequently, the phase-only subject variability analysis can be adopted for the pTx regime.

Chapter 6

Comparison with dipoles

6.1 Comparison setup

A B_1+ efficiency comparison with an 8TxRx fractionated dipole array was performed on a 7T Siemens Magnetom Terra site in Oxford using our body phantom. The reported loop array efficiency is lower than the results presented in subsection 5.2.2 due to the coil having been re-tuned to a human subject by the time the visit was organised, losing out on the phantom performance. A B_1+ mapping of both dipole and loop arrays was performed using the following sequences at different reference voltages: *tfl_b1map*, *tfl_rfmap*, and the novel *satTFL*, which allows shorter scan times[87]. To facilitate the comparison, the VOP and coil interfacing files were prepared to enable the dipole array to be used in pTx mode and gain the ability to specify a B_1+ shim. The B_1+ shim that maximised the B_1+ field at the centre of the phantom had to be determined manually and iteratively, as the starting shim configuration (identical phase for all channels) produced a void in the middle of the phantom. At each step, the per-channel phase maps were acquired using a *tfl_rfmap* sequence. Afterwards, each channel's transmit field's phase values in the region as close to the phantom's centre as possible that had enough SNR were noted. These values were then used to define a phase shim for the next iteration, yielding a stronger signal in the middle with each iteration and producing more accurate phase maps.

6.2 Comparison results

The central axial slice flip angle maps acquired with a *tfl_b1map* sequence are shown in Fig. 6.1. The same maps acquired with a *tfl_rfmap* sequence are shown in Fig. 6.2.The S-parameters matrices taken from the scanner are shown in Fig. 6.4. Mean flip angle values for the two arrays at different excitation voltages are shown in Fig. 6.3.

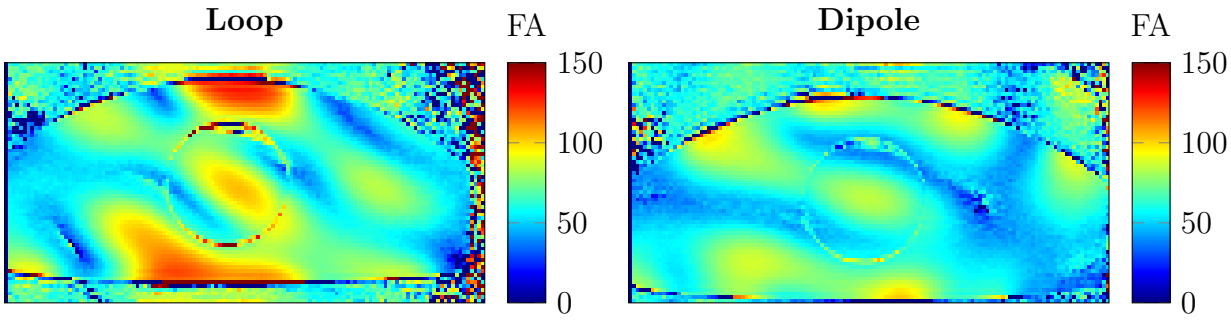

Figure 6.1: Flip angle maps acquired for the loop array and the dipole array at 400 V using a *tfl_b1map* sequence.

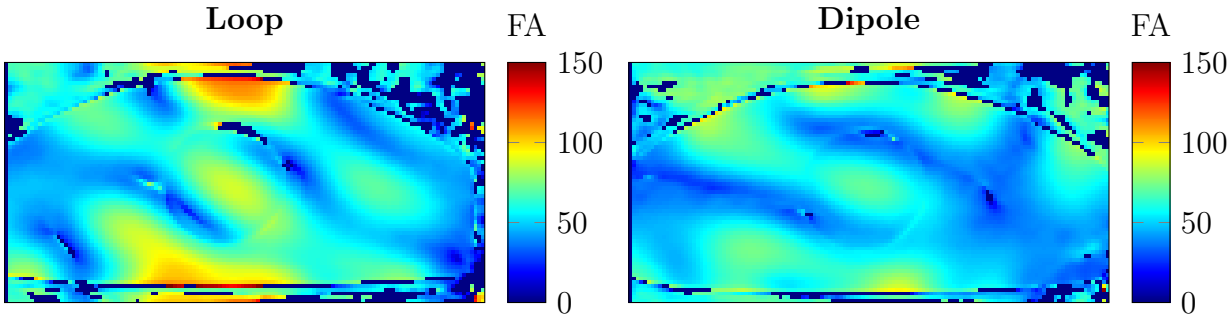

Figure 6.2: Flip angle maps acquired for the loop array and the dipole array at 350 V using a *tfl_rfmap* sequence.

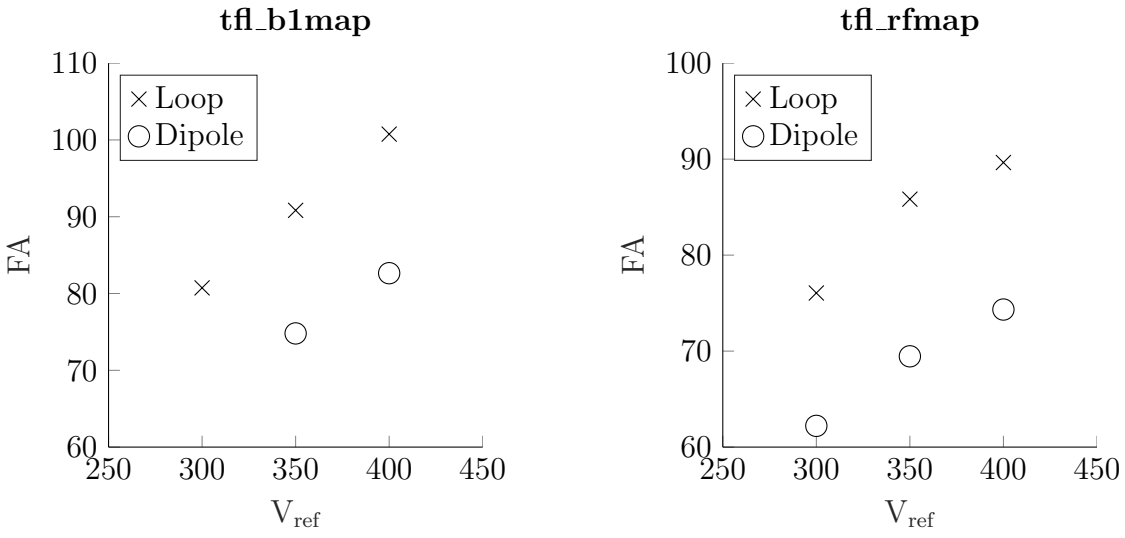

Figure 6.3: Mean flip angle values for the loop array and the dipole array within a small circular ROI in the middle of the phantom acquired at different excitation voltages.

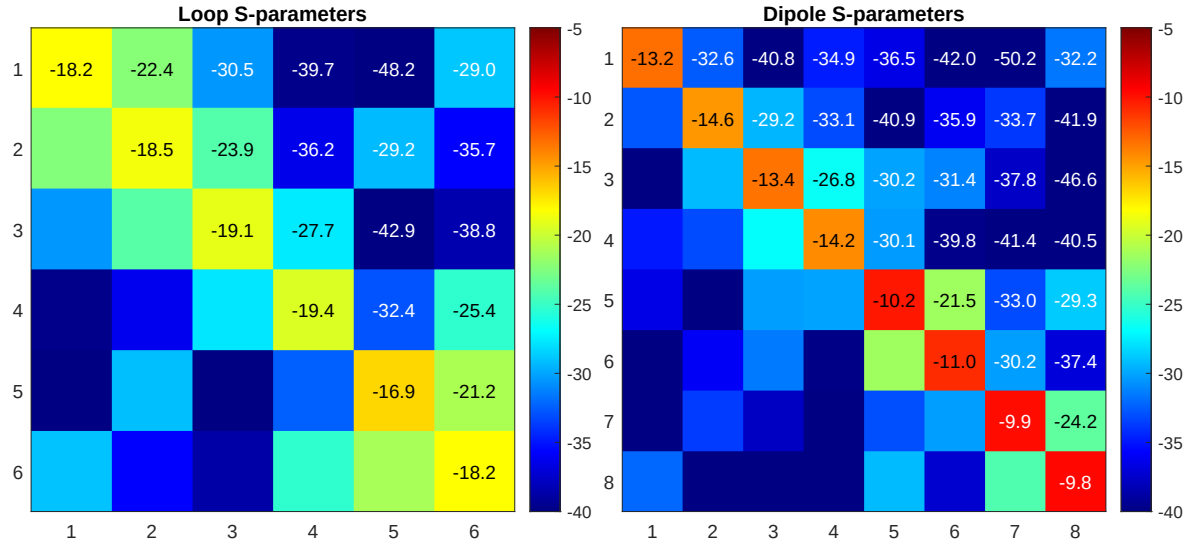

Figure 6.4: S-parameters matrices of the loop array and the dipole array acquired from the scanner.

6.3 Discussion

As shown in Fig. 6.1,Fig. 6.2 and Fig. 6.3, the loop array has demonstrated a markedly higher B_1+ efficiency at the centre of the phantom, however, caution must be taken interpreting the implications of this outcome. The coil's final performance depends as much on its design as it does on the design's implementation in practice, and the favourable outcome for the loop array could have been a result of the discrepancy between the implementations, and not of fundamental advantage of the loops over dipoles in the context of body imaging. More power was reflected back to the scanner with a dipole array, which suggests poor sample loading stability. The loop array was not tuned to the phantom and had no advantage over the dipole array in this respect. Furthermore, the loop array was using a static shim derived for the Duke digital body model, and not tailored to the phantom, unlike the dipole array.

The SAR efficiency of the two arrays was not compared, but the dipole array would have likely demonstrated a favourable performance. The preliminary healthy volunteer scanning with a loop array has shown SAR to be a bottleneck in how much power can be supplied to the coil, although this is partly a consequence of very conservative safety factors.

It is also speculated that another gain in B_1+ efficiency within a dipole array could have come from transmitting with only six dipoles arranged such that the there is a transmitting element at the projection of the central axis of the phantom: the peripheral elements in a 2×4 arrangement barely contribute to the excitation in the middle of the phantom. The dipole array was a lot easier to handle, in contrast to a crude, rigid prototype of the 6TxRx loop array.

Chapter 7

In-vivo results

Preliminary study of healthy subjects received ethical approval from the local NHS Clinical Research Imaging Facility (CRIF) Approval Group. The approval was granted to scan males below the age of 40, as in that age bracket the incidence of prostate pathologies is considered low. The volunteers were attempted to be recruited from the NHS volunteer databank. Unfortunately, no one responded, and the scanning sessions were performed on the colleagues who agreed to volunteer.

The subjects were scanned supine, lying feet first in the magnet. The imaging was performed using the Siemens product pulse sequences. The scan times were long due to being restricted to a normal operating mode and employing conservative safety factors.

A T_2 image of the prostate acquired within a healthy volunteer is shown in Fig. 7.1. A summary of the sequence parameters is shown in Table 7.1. The coil provided a good coverage of the anatomy of interest. Unfortunately, due to being limited by an overly conservative safety factor and scanning in a normal operating mode without the ability to use patient specific shims, any form of meaningful comparison with 3 T systems is impossible.

FOV	20x20 cm
Resolution	0.78x0.78x3 mm
Number of slices	5
Reference voltage	550 V
TE	96 ms
TR	11080 ms
Turbo factor	9
Scan time	10:43 min

Table 7.1: T2 TSE sequence parameters.

Figure 7.1: A T2 TSE image of the prostate in a healthy volunteer.

A DWI image of the prostate within a healthy volunteer acquired with RESOLVE[88] is shown in Fig. 7.2. The imaging parameters are shown in Table 7.2. Multi-shot diffusion-weighted EPI limited spatial distortion due to proximity of air spaces in rectum.

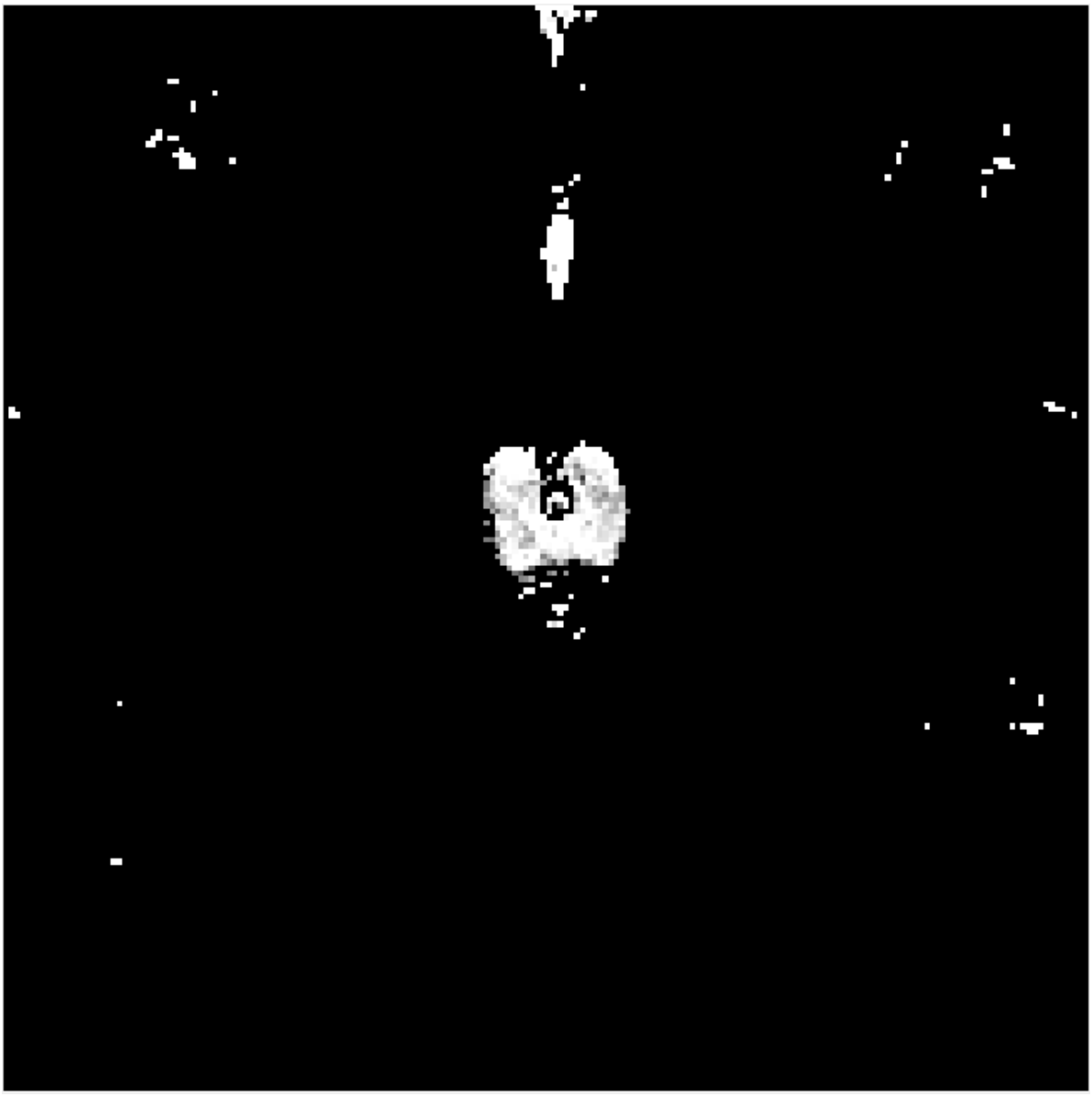

Figure 7.2: An ADC map of the prostate within a healthy volunteer acquired with RESOLVE.

FOV	20x20 cm
Resolution	1x1x3 mm
Number of slices	10
Reference voltage	600 V
Acceleration	GRAPPA 2
TE	74 ms
TR	6020 ms
EPI echo spacing	0.36 ms
EPI factor	116
Readout segments	7
Averages	2
b-values	0, 600 s/mm^2
Diffusion directions	4
Scan time	7:56 min

Table 7.2: RESOLVE sequence parameters used to acquired an ADC map.

Chapter 8

Conclusion

8.1 Summary of the work completed

Four different loop array configurations were simulated along with an eight-channel dipole array to act as reference. The 3x1 loop arrangement was extended into a full six-channel loop array. The design was constructed and its performance was validated in the phantom. Further simulation studies were conducted to acquired the necessary safety approval data. An ethics approval to scan healthy male volunteers under the age of 40 was procured. A handful of healthy volunteer scans were performed, demonstrating promising results. A transmit efficiency study comparing the performance of the loop array and a commercial eight-channel fractionated dipole array within the phantom was conducted, showing a favourable transmit performance of the loop array in producing an excitation at depth.

8.2 Simulation results

Four loop array configurations were simulated within the human digital body model: a 4x2 and 3x2 dual row arrangements, and two variations of a 3x1 arrangement, with and without the next-neighbouring element decoupling. Their transmit performance was assessed based on the static B_1 and SAR efficiency shims. The receive sensitivity of the arrays was analysed based on their mean sum of magnitudes B_1- field within the prostate gland.

The 4x2 configuration demonstrated a superior performance in every metric, followed by a 3x1 arrangement. However, this was not apparent until after the decision to build a 3x1 configuration was made. As such, the 4x2 arrangement was not developed further. The phased 3x1 loop array demonstrated a markedly better SAR performance compared to its dual row counterpart.

The 3x1 configuration was extended into a full six-channel array comprising an anterior and posterior half. The simulated performance of the full loop array was compared to

an eight-channel shortened dipole array. The six-channel loop array demonstrated superior performance to the shortened dipole array in terms of B_1 and SAR efficiency within the prostate. The loop array demonstrated an ability to maintain as much as 89.6% of its nominal B_1+ efficiency when employing an SAR shim, whilst boosting its SAR efficiency by 28.4%. In contrast, the shortened dipole array could only maintain 76.2% of its nominal B_1+ efficiency when shimming for SAR reduction. The simulated nominal SAR efficiency of 0.52 $\mu\mathrm{T}/\sqrt{\mathrm{pSAR}}$ is comparable to the fractionated dipole arrays reported in the literature, whilst offering a markedly higher transmit efficiency. The SAR performance is comparable to the state-of-the-art 16-channel combined loop and dipole array when the latter is used with phase-only shimming. The nominal transmit efficiency of 0.303 $\mu\mathrm{T}/\sqrt{\mathrm{W}}$ surpasses the nominal efficiency of the 16-channel combined loop and dipole array when the latter employs full amplitude and phase shimming. The simulation analysis demonstrated that at least within the context of prostate imaging, the six-channel loop array can match the SAR efficiency of the dipole arrays, whilst producing a much stronger excitation at depth regardless of the shimming objective (transmit or SAR efficiency). The proposed loop configuration is able to retain most of its nominal performance when phase-only shimming is considered.

It is believed by the thesis author that the primary reason behind the exceptional transmit performance of a combined 16-channel loop and dipole array is the realised density of the current paths running parallel to the B_0 field that can be manipulated independently. The reported loop width of 8 cm together with the reported centre-to-centre distance of 11.5 cm between the loop-dipole blocks means there is a current leg present every 4 cm. As such, when all 16 channels are used for shimming, the realised SAR and B_1 efficiencies are exceptionally high. A similar argument can be made about the 16-channel microstrip array: the density of the current paths together with the access to 16 independent channels allow for a high degree of shimming freedom. However, once only 8 channels are used to drive the loop-dipole combination, the advantage of the configuration is greatly diminished. The argument about the importance of the current path density can be applied to the dipole arrays. Due to the inter-element coupling, the existing shortened and fractionated dipole array implementations do not scale effectively to 16 channels, and the distance between the current legs is on the order of 7 to 10 cm. The degree of shimming freedom is therefore greatly reduced.

In contrast, using just 6 independent channels to drive the presented loop configuration was enough to match the SAR performance of the aforementioned state-of-the-art arrays that use 8 to 10 channels whilst surpassing them in terms of transmit efficiency. It is believed this loop arrangement worked well, because of the realised current path density: given that the loops were 12.5 cm wide and featured a 3 cm overlap, the array had current legs running parallel to B_0 every 3 to 6.5 cm. The study demonstrated that loop elements can be used effectively as the transmitters for UHF prostate imaging, requiring only 6 channels to shim effectively.

The study featured a "classical" phased loop array (rectangular loops with uniform capacitance distribution). But there are more ways to manipulate the current running along a closed path, such as by altering the loop geometry or using non-uniform capacitance distribution to create unbalanced currents, as was done in a "loopole" element reported by Lakshmanan et al.[89]

8.3 Coil implementation

The build quality of the array could be improved with respect to the adherence to the simulated geometry. The next-neighbouring decoupling with an overlap can be discarded, given its negligible impact on the coil's performance. The posterior half of the array should be reinforced with some supports to better handle the patient weight. The anterior half has proven to be bulky and unwieldy. However, without changing the overall design, this could be partly alleviated by adding means to strap it to the posterior half or the scanner table. This would also additionally reduce the degrees of positioning freedom. The interface box requires a redesign in its placement of the sockets for the posterior half of the array to keep the profile low when the plugs are connected, which was a source of discomfort for some volunteers as it was digging into their shins.

8.4 Phantom results

The temperature mapping results within the phantom employing a prostate shim were in a good agreement with the simulations. Although the thermal diffusion coefficient is small relative to the duration of the heating experiment, the analysis could have benefited from simulating the thermal diffusion. It would have been useful to perform the temperature mapping using multiple different shims to further build confidence in the degree of correlation between the simulations and observations, particularly using a SAR shim.

The B_1+ mapping results using an AFI sequence showed a good agreement in the mean and maximal magnitude of the B_1+ field produced at the centre of the phantom. However, there was a mismatch in magnitude on the periphery that was not explained.

A comparison with an eight-channel commercial fractionated dipole array carried out in Oxford demonstrated the loop array to be considerably more efficient in producing an excitation in the middle of the phantom. However, it was noted that the B_1+ field patterns were considerably more uniform for the dipole array, with very little difference observed between the flip angles in the immediate vicinity of the elements and in the middle of the phantom. The reflection parameters of the dipole array were considerably degraded compared to the loop array. The transfer parameters of the dipole array were remarkably low. However, this is partly attributed to poor reflection coefficients. In contrast, the loop array demonstrated a good tuning stability, as the reflection coefficients remained high without having to tune the coil to a phantom.

A more complete analysis would have included a temperature mapping session and a volunteer scan for the two arrays. However, this was not possible to accommodate in the time available for this part of the study, which was carried out during the site visit to Oxford.

8.5 In-vivo results

Due to the difficulties in recruiting healthy volunteers only 4 people were scanned in total. The opportunities to optimise the imaging protocols were therefore limited. Whilst the produced T_2 TSE image appeared adequate, the SNR was insufficient for performing DWI. However, it is not possible to draw any conclusions at this stage, given that the DWI was only performed within a single healthy volunteer. Because the ethics approval was only granted for healthy subjects under 40 years of age, the opportunity to scan cancer patients was not present.

The revised safety assessment procedure described in Sec. 5.5 was not implemented at the time the volunteer scanning took place. Consequently, the coil's utility was hampered by a very conservative safety factor given in Sec. 5.4. Furthermore, the scanning was limited to normal operating mode and using a static shim configuration when scanning volunteers.

8.6 Future work

With a new safety and pTx approval in place, an in-vivo performance assessment of the existing coil is pending following imaging protocol optimisation. On the coil development side, immediate future work entails building a second prototype of the coil. The second version of the coil will feature a new housing and a dedicated receive array to enhance the coil's parallel imaging capabilities and SNR. The six-channel transmitter configuration will be kept, but the next-neighbouring overlap will be removed.

One of the major disadvantages of the proposed array is its rigidity. Compared to a dipole array that is inherently flexible and able to be used as a general purpose body coil out of the box, the existing rigid six-channel loop design has limited utility outside of imaging central pelvic and abdominal regions. Figuring out a way to make a semi-rigid loop arrangement without compromising the transmit performance would greatly enhance the utility of loops as transmitters at UHF.

The conducted work only examined a "classical" phased loop array configuration (rectangular loops with a uniformly distributed capacitance). Compared to a dipole, there is more design freedom available for manipulating the current pattern on a loop, such as by adjusting its geometry and capacitance distribution. The principle of increasing the density of current paths to achieve a better performance will be probed further using loops as the primary building blocks. The focus will be on attempting to find a configu-

ration that can surpass the achieved performance whilst still only requiring no more than 8 independent channels to shim efficiently.

One of the biggest challenges of UHF imaging is the local SAR management. Large safety factors arising as a result of reliance on models due to inability to adequately measure temperature increase during the scan are one of the major obstacles in realising the full potential of the UHF systems. Part of the future work will focus on refining the coil safety evaluation procedure to be less restrictive, but without compromising the patient safety. For example, by adopting a sum of squares approach to combining the subject variability and modelling uncertainty for safety factor derivation as proposed by Steensma et al.[86].

Bibliography

[1] R. Berges and M. Oelke. "Age-stratified normal values for prostate volume, PSA, maximum urinary flow rate, IPSS, and other LUTS/BPH indicators in the German male community-dwelling population aged 50 years or older". In: *World Journal of Urology* 29 (2011), pp. 171–178. DOI: https://doi.org/10.1007/s00345-010-0638-z.

[2] Cancer Research UK. *Cancer incidence for common cancers*. http://www.cancerresearchuk.org/health-professional/cancer-statistics/incidence/common-cancers-compared/. 2015.

[3] Cancer Research UK. *Prostate cancer incidence statistics: Prostate cancer incidence by age (2011-2013)*. http://www.cancerresearchuk.org/health-professional/cancer-statistics/statistics-by-cancer-type/prostate-cancer/incidence/. 2015.

[4] Hashim U Ahmed et al. "Diagnostic accuracy of multi-parametric MRI and TRUS biopsy in prostate cancer (PROMIS): a paired validating confirmatory study". In: *The Lancet* 389.10071 (Feb. 2017), pp. 815–822. ISSN: 0140-6736. DOI: 10.1016/s0140-6736(16)32401-1. URL: http://dx.doi.org/10.1016/S0140-6736(16)32401-1.

[5] Baris Turkbey et al. "Multiparametric prostate magnetic resonance imaging in the evaluation of prostate cancer". In: *CA: A Cancer Journal for Clinicians* 66.4 (Nov. 2015), pp. 326–336. ISSN: 1542-4863. DOI: 10.3322/caac.21333. URL: http://dx.doi.org/10.3322/caac.21333.

[6] American College of Radiology. *PI-RADS Prostate Imaging – Reporting and Data System Version 2.1*. 2019.

[7] Bart R. Steensma et al. "Comparing signal-to-noise ratio for prostate imaging at 7T and 3T". In: *Journal of Magnetic Resonance Imaging* 49.5 (Oct. 2018), pp. 1446–1455. ISSN: 1522-2586. DOI: 10.1002/jmri.26527. URL: http://dx.doi.org/10.1002/jmri.26527.

[8] David I. Hoult. "Sensitivity and Power Deposition in a High-Field Imaging Experiment". In: *Journal of Magnetic Resonance Imaging* 12.1 (2000), pp. 46–67. ISSN: 1522-2586. DOI: 10.1002/1522-2586(200007)12:1<46::aid-jmri6>3.0.co;2-d. URL: http://dx.doi.org/10.1002/1522-2586(200007)12:1%3C46::aid-jmri6%3E3.0.co;2-d.

[9] Sydney N Williams, Paul McElhinney, and Shajan Gunamony. "Ultra-high field MRI: parallel-transmit arrays and RF pulse design". In: *Physics in Medicine & Biology* 68.2 (Jan. 2023), 02TR02. ISSN: 1361-6560. DOI: 10.1088/1361-6560/aca4b7. URL: http://dx.doi.org/10.1088/1361-6560/aca4b7.

[10] Francesco Padormo et al. "Parallel transmission for ultrahigh-field imaging". In: *NMR in Biomedicine* 29.9 (May 2015), pp. 1145–1161. ISSN: 1099-1492. DOI: 10.1002/nbm.3313. URL: http://dx.doi.org/10.1002/nbm.3313.

[11] Gregory J. Metzger et al. "Local B1+ shimming for prostate imaging with transceiver arrays at 7T based on subject-dependent transmit phase measurements". In: *Magnetic Resonance in Medicine* 59.2 (Jan. 2008), pp. 396–409. ISSN: 1522-2594. DOI: 10.1002/mrm.21476. URL: http://dx.doi.org/10.1002/mrm.21476.

[12] Alexander J.E. Raaijmakers et al. "The fractionated dipole antenna: A new antenna for body imaging at 7 Tesla". In: *Magnetic Resonance in Medicine* 75.3 (May 2015), pp. 1366–1374. ISSN: 1522-2594. DOI: 10.1002/mrm.25596. URL: http://dx.doi.org/10.1002/mrm.25596.

[13] M. Arcan Ertürk et al. "A 16-channel combined loop-dipole transceiver array for 7 Tesla body MRI". In: *Magnetic Resonance in Medicine* 77.2 (Feb. 2016), pp. 884–894. ISSN: 1522-2594. DOI: 10.1002/mrm.26153. URL: http://dx.doi.org/10.1002/mrm.26153.

[14] Aurelien Destruel et al. "Integrated Multi-Modal Antenna With Coupled Radiating Structures (I-MARS) for 7T pTx Body MRI". In: *IEEE Transactions on Medical Imaging* 41.1 (Jan. 2022), pp. 39–51. ISSN: 1558-254X. DOI: 10.1109/tmi.2021.3103654. URL: http://dx.doi.org/10.1109/TMI.2021.3103654.

[15] Bart R. Steensma et al. "An 8-channel Tx/Rx dipole array combined with 16 Rx loops for high-resolution functional cardiac imaging at 7T". In: *Magnetic Resonance Materials in Physics, Biology and Medicine* 31.1 (Nov. 2017), pp. 7–18. ISSN: 1352-8661. DOI: 10.1007/s10334-017-0665-5. URL: http://dx.doi.org/10.1007/s10334-017-0665-5.

[16] Jan Paška, Martijn A. Cloos, and Graham C. Wiggins. "A rigid, stand-off hybrid dipole, and birdcage coil array for 7 T body imaging". In: *Magnetic Resonance in Medicine* 80.2 (Dec. 2017), pp. 822–832. ISSN: 1522-2594. DOI: 10.1002/mrm.27048. URL: http://dx.doi.org/10.1002/mrm.27048.

[17] David J. Griffiths. *Introduction to Electrodynamics*. 4th ed. Cambridge University Press, 2017.

[18] D. I. Hoult. "The principle of reciprocity in signal strength calculations - A mathematical guide". In: *Concepts in Magnetic Resonance* 12.4 (2000), pp. 173–187. ISSN: 1099-0534. DOI: 10.1002/1099-0534(2000)12:4<173::aid-cmr1>3.0.co;2-q. URL: http://dx.doi.org/10.1002/1099-0534(2000)12:4%3C173::AID-CMR1%3E3.0.CO;2-Q.

[19] S Gabriel, R W Lau, and C Gabriel. "The dielectric properties of biological tissues: III. Parametric models for the dielectric spectrum of tissues". In: *Physics*

in Medicine and Biology 41.11 (Nov. 1996), pp. 2271–2293. ISSN: 1361-6560. DOI: 10.1088/0031-9155/41/11/003. URL: http://dx.doi.org/10.1088/0031-9155/41/11/003.

[20] Dassault Systemes. *CST Studio Suite 2020 documentation*. 2021.

[21] S Gabriel, R W Lau, and C Gabriel. "The dielectric properties of biological tissues: II. Measurements in the frequency range 10 Hz to 20 GHz". In: *Physics in Medicine and Biology* 41.11 (Nov. 1996), pp. 2251–2269. ISSN: 1361-6560. DOI: 10.1088/0031-9155/41/11/002. URL: http://dx.doi.org/10.1088/0031-9155/41/11/002.

[22] C. Gabriel. "Compilation of the Dielectric Properties of Body Tissues at RF and Microwave Frequencies". In: *Report N.AL/OE-TR- 1996-0037, Occupational and environmental health directorate, Radiofrequency Radiation Division, Brooks Air Force Base* (1996).

[23] Thomas Weiland. "A discretization model for the solution of Maxwell's equations for six-component fields". In: *Electronics and Communications AEU* 31.3 (1977), pp. 116–120.

[24] M. Clemens and T. Weil. "Discrete Electromagnetism with the Finite Integration Technique". In: *Progress In Electromagnetics Research* 32 (2001), pp. 65–87. ISSN: 1559-8985. DOI: 10.2528/pier00080103. URL: http://dx.doi.org/10.2528/PIER00080103.

[25] Kane Yee. "Numerical solution of initial boundary value problems involving maxwell's equations in isotropic media". In: *IEEE Transactions on Antennas and Propagation* 14.3 (May 1966), pp. 302–307. ISSN: 1558-2221. DOI: 10.1109/tap.1966.1138693. URL: http://dx.doi.org/10.1109/TAP.1966.1138693.

[26] Holger Spachmann et al. "FIT-formulation for non-linear dispersive media". In: *International Journal of Numerical Modelling: Electronic Networks, Devices and Fields* 12.1–2 (Jan. 1999), pp. 81–92. ISSN: 1099-1204. DOI: 10.1002/(sici)1099-1204(199901/04)12:1/2<81::aid-jnm324>3.0.co;2-l. URL: http://dx.doi.org/10.1002/(SICI)1099-1204(199901/04)12:1/2%3C81::AID-JNM324%3E3.0.CO;2-L.

[27] Z.S. Sacks et al. "A perfectly matched anisotropic absorber for use as an absorbing boundary condition". In: *IEEE Transactions on Antennas and Propagation* 43.12 (1995), pp. 1460–1463. ISSN: 0018-926X. DOI: 10.1109/8.477075. URL: http://dx.doi.org/10.1109/8.477075.

[28] Weng Cho Chew and William H. Weedon. "A 3D perfectly matched medium from modified maxwell's equations with stretched coordinates". In: *Microwave and Optical Technology Letters* 7.13 (Sept. 1994), pp. 599–604. ISSN: 1098-2760. DOI: 10.1002/mop.4650071304. URL: http://dx.doi.org/10.1002/mop.4650071304.

[29] M. Kuzuoglu and R. Mittra. "Frequency dependence of the constitutive parameters of causal perfectly matched anisotropic absorbers". In: *IEEE Microwave and Guided Wave Letters* 6.12 (1996), pp. 447–449. ISSN: 1051-8207. DOI: 10.1109/75.544545. URL: http://dx.doi.org/10.1109/75.544545.

[30] J. Alan Roden and Stephen D. Gedney. "Convolution PML (CPML): An efficient FDTD implementation of the CFS-PML for arbitrary media". In: *Microwave and Optical Technology Letters* 27.5 (2000), pp. 334–339. ISSN: 1098-2760. DOI: 10.1002/1098-2760(20001205)27:5<334::aid-mop14>3.0.co;2-a. URL: http://dx.doi.org/10.1002/1098-2760(20001205)27:5%3C334::AID-MOP14%3E3.0.CO;2-A.

[31] Jean-Pierre Bérenger. *Perfectly Matched Layer (PML) for Computational Electromagnetics*. Springer International Publishing, 2007. ISBN: 9783031016967. DOI: 10.1007/978-3-031-01696-7. URL: http://dx.doi.org/10.1007/978-3-031-01696-7.

[32] Jean-Pierre Berenger. "A perfectly matched layer for the absorption of electromagnetic waves". In: *Journal of Computational Physics* 114.2 (Oct. 1994), pp. 185–200. ISSN: 0021-9991. DOI: 10.1006/jcph.1994.1159. URL: http://dx.doi.org/10.1006/jcph.1994.1159.

[33] F Bloch. "Nuclear induction". In: *Physica* 17.3–4 (Mar. 1951), pp. 272–281. ISSN: 0031-8914. DOI: 10.1016/0031-8914(51)90068-7. URL: http://dx.doi.org/10.1016/0031-8914(51)90068-7.

[34] E. M. Purcell, H. C. Torrey, and R. V. Pound. "Resonance Absorption by Nuclear Magnetic Moments in a Solid". In: *Physical Review* 69.1–2 (Jan. 1946), pp. 37–38. ISSN: 0031-899X. DOI: 10.1103/physrev.69.37. URL: http://dx.doi.org/10.1103/PhysRev.69.37.

[35] R. Feynman. *The Feynman Lectures on Physics*. 1966.

[36] Robert W. Brown et al. *Magnetic Resonance Imaging: Physical Principles and Sequence Design*. Wiley, Apr. 2014. ISBN: 9781118633953. DOI: 10.1002/9781118633953. URL: http://dx.doi.org/10.1002/9781118633953.

[37] Ruomin Hu et al. "X-nuclei imaging: Current state, technical challenges, and future directions". In: *Journal of Magnetic Resonance Imaging* 51.2 (2020), pp. 355–376. DOI: https://doi.org/10.1002/jmri.26780. eprint: https://onlinelibrary.wiley.com/doi/pdf/10.1002/jmri.26780. URL: https://onlinelibrary.wiley.com/doi/abs/10.1002/jmri.26780.

[38] Stig Ljunggren. "A simple graphical representation of fourier-based imaging methods". In: *Journal of Magnetic Resonance (1969)* 54.2 (1983), pp. 338–343. ISSN: 0022-2364. DOI: https://doi.org/10.1016/0022-2364(83)90060-4. URL: https://www.sciencedirect.com/science/article/pii/0022236483900604.

[39] Donald B. Twieg. "The k-trajectory formulation of the NMR imaging process with applications in analysis and synthesis of imaging methods". In: *Medical Physics* 10.5 (1983), pp. 610–621. DOI: https://doi.org/10.1118/1.595331. eprint: https://aapm.onlinelibrary.wiley.com/doi/pdf/10.1118/1.595331. URL: https://aapm.onlinelibrary.wiley.com/doi/abs/10.1118/1.595331.

[40] Donald B. Twieg. "The k-trajectory formulation of the NMR imaging process with applications in analysis and synthesis of imaging methods". In: *Medical Physics*

10.5 (Sept. 1983), pp. 610–621. ISSN: 2473-4209. DOI: 10.1118/1.595331. URL: http://dx.doi.org/10.1118/1.595331.

[41] Stig Ljunggren. "A simple graphical representation of fourier-based imaging methods". In: *Journal of Magnetic Resonance (1969)* 54.2 (Sept. 1983), pp. 338–343. ISSN: 0022-2364. DOI: 10.1016/0022-2364(83)90060-4. URL: http://dx.doi.org/10.1016/0022-2364(83)90060-4.

[42] E. L. Hahn. "Spin Echoes". In: *Phys. Rev.* 80 (4 Nov. 1950), pp. 580–594. DOI: 10.1103/PhysRev.80.580. URL: https://link.aps.org/doi/10.1103/PhysRev.80.580.

[43] Jürgen Hennig. "Echoes—how to generate, recognize, use or avoid them in MR-imaging sequences. Part I: Fundamental and not so fundamental properties of spin echoes". In: *Concepts in Magnetic Resonance* 3.3 (July 1991), pp. 125–143. ISSN: 1099-0534. DOI: 10.1002/cmr.1820030302. URL: http://dx.doi.org/10.1002/cmr.1820030302.

[44] P. B. Roemer et al. "The NMR phased array". In: *Magnetic Resonance in Medicine* 16.2 (Nov. 1990), pp. 192–225. ISSN: 1522-2594. DOI: 10.1002/mrm.1910160203. URL: http://dx.doi.org/10.1002/mrm.1910160203.

[45] N.I. Avdievich. "Transceiver-Phased Arrays for Human Brain Studies at 7 T". In: *Applied Magnetic Resonance* 41 (2011), pp. 483–506. DOI: https://doi.org/10.1007/s00723-011-0280-y.

[46] Kyle M. Gilbert et al. "Transmit/receive radiofrequency coil with individually shielded elements". In: *Magnetic Resonance in Medicine* 64.6 (2010), pp. 1640–1651. DOI: https://doi.org/10.1002/mrm.22574. eprint: https://onlinelibrary.wiley.com/doi/pdf/10.1002/mrm.22574. URL: https://onlinelibrary.wiley.com/doi/abs/10.1002/mrm.22574.

[47] Kamil Uğurbil et al. "Brain imaging with improved acceleration and SNR at 7 Tesla obtained with 64-channel receive array". In: *Magnetic Resonance in Medicine* 82.1 (2019), pp. 495–509. DOI: https://doi.org/10.1002/mrm.27695. eprint: https://onlinelibrary.wiley.com/doi/pdf/10.1002/mrm.27695. URL: https://onlinelibrary.wiley.com/doi/abs/10.1002/mrm.27695.

[48] G. Shajan et al. "A 16-channel dual-row transmit array in combination with a 31-element receive array for human brain imaging at 9.4 T". In: *Magnetic Resonance in Medicine* 71.2 (2014), pp. 870–879. DOI: https://doi.org/10.1002/mrm.24726. eprint: https://onlinelibrary.wiley.com/doi/pdf/10.1002/mrm.24726. URL: https://onlinelibrary.wiley.com/doi/abs/10.1002/mrm.24726.

[49] Qi Duan et al. "A 7T spine array based on electric dipole transmitters". In: *Magnetic Resonance in Medicine* 74.4 (2015), pp. 1189–1197. DOI: https://doi.org/10.1002/mrm.25817. eprint: https://onlinelibrary.wiley.com/doi/pdf/10.1002/mrm.25817. URL: https://onlinelibrary.wiley.com/doi/abs/10.1002/mrm.25817.

[50] J. Thomas Vaughan et al. “Whole-body imaging at 7T: Preliminary results”. In: *Magnetic Resonance in Medicine* 61.1 (2009), pp. 244–248. DOI: https://doi.org/10.1002/mrm.21751. eprint: https://onlinelibrary.wiley.com/doi/pdf/10.1002/mrm.21751. URL: https://onlinelibrary.wiley.com/doi/abs/10.1002/mrm.21751.

[51] C. J. Snyder et al. “Comparison between eight- and sixteen-channel TEM transceive arrays for body imaging at 7 T”. In: *Magnetic Resonance in Medicine* 67.4 (2012), pp. 954–964. DOI: https://doi.org/10.1002/mrm.23070. eprint: https://onlinelibrary.wiley.com/doi/pdf/10.1002/mrm.23070. URL: https://onlinelibrary.wiley.com/doi/abs/10.1002/mrm.23070.

[52] Gregor Adriany et al. “Transmit and receive transmission line arrays for 7 Tesla parallel imaging”. In: *Magnetic Resonance in Medicine* 53.2 (2005), pp. 434–445. DOI: https://doi.org/10.1002/mrm.20321. eprint: https://onlinelibrary.wiley.com/doi/pdf/10.1002/mrm.20321. URL: https://onlinelibrary.wiley.com/doi/abs/10.1002/mrm.20321.

[53] Stefan H. G. Rietsch et al. “7T ultra-high field body MR imaging with an 8-channel transmit/32-channel receive radiofrequency coil array”. In: *Medical Physics* 45.7 (2018), pp. 2978–2990. DOI: https://doi.org/10.1002/mp.12931. eprint: https://aapm.onlinelibrary.wiley.com/doi/pdf/10.1002/mp.12931. URL: https://aapm.onlinelibrary.wiley.com/doi/abs/10.1002/mp.12931.

[54] Cecil E Hayes et al. “An efficient, highly homogeneous radiofrequency coil for whole-body NMR imaging at 1.5 T”. In: *Journal of Magnetic Resonance (1969)* 63.3 (1985), pp. 622–628. ISSN: 0022-2364. DOI: https://doi.org/10.1016/0022-2364(85)90257-4. URL: https://www.sciencedirect.com/science/article/pii/0022236485902574.

[55] J. Thomas Vaughan et al. “Whole-body imaging at 7T: Preliminary results”. In: *Magnetic Resonance in Medicine* 61.1 (2009), pp. 244–248. DOI: https://doi.org/10.1002/mrm.21751. eprint: https://onlinelibrary.wiley.com/doi/pdf/10.1002/mrm.21751. URL: https://onlinelibrary.wiley.com/doi/abs/10.1002/mrm.21751.

[56] J.T. Vaughan et al. “Detunable transverse electromagnetic (TEM) volume coil for high-field NMR”. In: *Magnetic Resonance in Medicine* 47.5 (2002), pp. 990–1000. DOI: https://doi.org/10.1002/mrm.10141. eprint: https://onlinelibrary.wiley.com/doi/pdf/10.1002/mrm.10141. URL: https://onlinelibrary.wiley.com/doi/abs/10.1002/mrm.10141.

[57] Shajan Gunamony et al. *TRANSMIT / RECEIVE SWITCH , A TRANSMIT COIL ARRAY AND A RECEIVE COIL ARRAY FOR MRI*. U.S. Patent US10168402B2, Jan. 2019.

[58] David J Larkman and Rita G Nunes. “Parallel magnetic resonance imaging”. In: *Physics in Medicine and Biology* 52.7 (Mar. 2007), R15–R55. ISSN: 1361-6560. DOI:

10.1088/0031-9155/52/7/r01. URL: http://dx.doi.org/10.1088/0031-9155/52/7/R01.

[59] G. Shajan et al. "Three-layered radio frequency coil arrangement for sodium MRI of the human brain at 9.4 Tesla". In: *Magnetic Resonance in Medicine* 75.2 (2016), pp. 906–916. DOI: https://doi.org/10.1002/mrm.25666. eprint: https://onlinelibrary.wiley.com/doi/pdf/10.1002/mrm.25666. URL: https://onlinelibrary.wiley.com/doi/abs/10.1002/mrm.25666.

[60] Neal K. Bangerter et al. "Sodium MRI radiofrequency coils for body imaging". In: *NMR in Biomedicine* 29.2 (2016), pp. 107–118. DOI: https://doi.org/10.1002/nbm.3392. eprint: https://analyticalsciencejournals.onlinelibrary.wiley.com/doi/pdf/10.1002/nbm.3392. URL: https://analyticalsciencejournals.onlinelibrary.wiley.com/doi/abs/10.1002/nbm.3392.

[61] David M. Peterson et al. "Common mode signal rejection methods for MRI: Reduction of cable shield currents for high static magnetic field systems". In: *Concepts in Magnetic Resonance Part B: Magnetic Resonance Engineering* 19B.1 (2003), pp. 1–8. DOI: https://doi.org/10.1002/cmr.b.10090. eprint: https://onlinelibrary.wiley.com/doi/pdf/10.1002/cmr.b.10090. URL: https://onlinelibrary.wiley.com/doi/abs/10.1002/cmr.b.10090.

[62] Bernhard Gruber et al. "A 128-channel receive array for cortical brain imaging at 7T". In: *Magnetic Resonance in Medicine* 90.6 (Aug. 2023), pp. 2592–2607. ISSN: 1522-2594. DOI: 10.1002/mrm.29798. URL: http://dx.doi.org/10.1002/mrm.29798.

[63] Medicines and Healthcare products Regulatory Agency. *Safety Guidelines for Magnetic Resonance Imaging Equipment in Clinical Use*. 2022.

[64] Internation Electrotechnical Commission. *IEC 60601-2-33:2022*. 2022.

[65] W. Schnell et al. "Ultimate signal-to-noise-ratio of surface and body antennas for magnetic resonance imaging". In: *IEEE Transactions on Antennas and Propagation* 48.3 (Mar. 2000), pp. 418–428. ISSN: 0018-926X. DOI: 10.1109/8.841903. URL: http://dx.doi.org/10.1109/8.841903.

[66] Christopher Stumpf, Matthias Malzacher, and Lorenz-Peter Schmidt. "Radio Frequency Modeling of Receive Coil Arrays for Magnetic Resonance Imaging". In: *Journal of Imaging* 4.5 (May 2018), p. 67. ISSN: 2313-433X. DOI: 10.3390/jimaging4050067. URL: http://dx.doi.org/10.3390/jimaging4050067.

[67] Philip M. Robson et al. "Comprehensive quantification of signal-to-noise ratio and g-factor for image-based and k-space-based parallel imaging reconstructions". In: *Magnetic Resonance in Medicine* 60.4 (Sept. 2008), pp. 895–907. ISSN: 1522-2594. DOI: 10.1002/mrm.21728. URL: http://dx.doi.org/10.1002/mrm.21728.

[68] Santiago Aja-Fernández, Gonzalo Vegas-Sánchez-Ferrero, and Antonio Tristán-Vega. "Noise estimation in parallel MRI: GRAPPA and SENSE". In: *Magnetic Resonance Imaging* 32.3 (Apr. 2014), pp. 281–290. ISSN: 0730-725X. DOI: 10.1016/j.mri.2013.12.001. URL: http://dx.doi.org/10.1016/j.mri.2013.12.001.

[69] Bernhard Gruber et al. “RF coils: A practical guide for nonphysicists”. In: *Journal of Magnetic Resonance Imaging* 48.3 (2018), pp. 590–604. DOI: https://doi.org/10.1002/jmri.26187. eprint: https://onlinelibrary.wiley.com/doi/pdf/10.1002/jmri.26187. URL: https://onlinelibrary.wiley.com/doi/abs/10.1002/jmri.26187.

[70] Roger Jason Stafford. “The Physics of Magnetic Resonance Imaging Safety”. In: *Magnetic Resonance Imaging Clinics of North America* 28.4 (2020). MR Safety, pp. 517–536. ISSN: 1064-9689. DOI: https://doi.org/10.1016/j.mric.2020.08.002. URL: https://www.sciencedirect.com/science/article/pii/S1064968920300519.

[71] H. H. Pennes. “Analysis of Tissue and Arterial Blood Temperatures in the Resting Human Forearm”. In: *Journal of Applied Physiology* 85.1 (July 1998), pp. 5–34. ISSN: 1522-1601. DOI: 10.1152/jappl.1998.85.1.5. URL: http://dx.doi.org/10.1152/jappl.1998.85.1.5.

[72] Ingmar Graesslin et al. “A specific absorption rate prediction concept for parallel transmission MR”. In: *Magnetic Resonance in Medicine* 68.5 (Jan. 2012), pp. 1664–1674. ISSN: 1522-2594. DOI: 10.1002/mrm.24138. URL: http://dx.doi.org/10.1002/mrm.24138.

[73] *ICE internal documentation on Q-matrix generation.*

[74] Gabriele Eichfelder and Matthias Gebhardt. “Local specific absorption rate control for parallel transmission by virtual observation points”. In: *Magnetic Resonance in Medicine* 66.5 (May 2011), pp. 1468–1476. ISSN: 1522-2594. DOI: 10.1002/mrm.22927. URL: http://dx.doi.org/10.1002/mrm.22927.

[75] Yasutoshi Ishihara et al. “A precise and fast temperature mapping using water proton chemical shift”. In: *Magnetic Resonance in Medicine* 34.6 (Dec. 1995), pp. 814–823. ISSN: 1522-2594. DOI: 10.1002/mrm.1910340606. URL: http://dx.doi.org/10.1002/mrm.1910340606.

[76] Qi Duan et al. “Characterization of a dielectric phantom for high-field magnetic resonance imaging applications”. In: *Medical Physics* 41.10 (Oct. 2014). ISSN: 2473-4209. DOI: 10.1118/1.4895823. URL: http://dx.doi.org/10.1118/1.4895823.

[77] National Institutes of Health Advanced MRI. https://amri.ninds.nih.gov/cgi-bin/phantomrecipe/. 2016.

[78] T.W. Athey, M.A. Stuchly, and S.S. Stuchly. “Measurement of Radio Frequency Permittivity of Biological Tissues with an Open-Ended Coaxial Line: Part I”. In: *IEEE Transactions on Microwave Theory and Techniques* 30.1 (Jan. 1982), pp. 82–86. ISSN: 1557-9670. DOI: 10.1109/tmtt.1982.1131021. URL: http://dx.doi.org/10.1109/TMTT.1982.1131021.

[79] Alessandra La Gioia et al. “Open-Ended Coaxial Probe Technique for Dielectric Measurement of Biological Tissues: Challenges and Common Practices”. In: *Diagnostics* 8.2 (June 2018), p. 40. ISSN: 2075-4418. DOI: 10.3390/diagnostics8020040. URL: http://dx.doi.org/10.3390/diagnostics8020040.

[80] SPEAG. *DAK V2.4 Application Note: DAK/DAKS Best Practices*. 2017.

[81] Rohde & Schwarz. *Measurement of Dielectric Material Properties - Application Note*.

[82] Sohae Chung et al. "Rapid B1+ mapping using a preconditioning RF pulse with TurboFLASH readout". In: *Magnetic Resonance in Medicine* 64.2 (May 2010), pp. 439–446. ISSN: 1522-2594. DOI: 10.1002/mrm.22423. URL: http://dx.doi.org/10.1002/mrm.22423.

[83] H-P. Fautz et al. *B1 mapping of coil arrays for parallel transmission. Proc. Intl. Soc. Mag. Reson. Med. 16*. 2008.

[84] Vasily L. Yarnykh. "Actual flip-angle imaging in the pulsed steady state: A method for rapid three-dimensional mapping of the transmitted radiofrequency field". In: *Magnetic Resonance in Medicine* 57.1 (Dec. 2006), pp. 192–200. ISSN: 1522-2594. DOI: 10.1002/mrm.21120. URL: http://dx.doi.org/10.1002/mrm.21120.

[85] Jullie W. Pan, Donald B. Twieg, and Hoby P. Hetherington. "Quantitative spectroscopic imaging of the human brain". In: *Magnetic Resonance in Medicine* 40.3 (1998), pp. 363–369. DOI: https://doi.org/10.1002/mrm.1910400305. eprint: https://onlinelibrary.wiley.com/doi/pdf/10.1002/mrm.1910400305. URL: https://onlinelibrary.wiley.com/doi/abs/10.1002/mrm.1910400305.

[86] Bart Romke Steensma et al. "Tier-based formalism for safety assessment of custom-built radio-frequency transmit coils". In: *NMR in Biomedicine* 36.5 (2023), e4874. DOI: https://doi.org/10.1002/nbm.4874. eprint: https://analyticalsciencejournals.onlinelibrary.wiley.com/doi/pdf/10.1002/nbm.4874. URL: https://analyticalsciencejournals.onlinelibrary.wiley.com/doi/abs/10.1002/nbm.4874.

[87] James L. Kent et al. "Rapid 3D absolute B1+ mapping using a sandwiched train presaturated TurboFLASH sequence at 7T for the brain and heart". In: *Magnetic Resonance in Medicine* 89.3 (Nov. 2022), pp. 964–976. ISSN: 1522-2594. DOI: 10.1002/mrm.29497. URL: http://dx.doi.org/10.1002/mrm.29497.

[88] David A. Porter and Robin M. Heidemann. "High resolution diffusion-weighted imaging using readout-segmented echo-planar imaging, parallel imaging and a two-dimensional navigator-based reacquisition". In: *Magnetic Resonance in Medicine* 62.2 (May 2009), pp. 468–475. ISSN: 1522-2594. DOI: 10.1002/mrm.22024. URL: http://dx.doi.org/10.1002/mrm.22024.

[89] Karthik Lakshmanan et al. "The "Loopole" Antenna: A Hybrid Coil Combining Loop and Electric Dipole Properties for Ultra-High-Field MRI". In: *Concepts in Magnetic Resonance Part B* 2020.1 (2020), p. 8886543. DOI: https://doi.org/10.1155/2020/8886543. eprint: https://onlinelibrary.wiley.com/doi/pdf/10.1155/2020/8886543. URL: https://onlinelibrary.wiley.com/doi/abs/10.1155/2020/8886543.

Appendices

Appendix A

Simulation results processing

A.1 VBA macros

A.1.1 SAR result generation

```
Option Explicit

Sub Main
        Dim NumChannel, N, M As Integer

        NumChannel = 6

        For N = 1 To NumChannel
                For M = 1 To NumChannel
                        With SAR
                                .Reset
                                .PowerLossMonitor("loss (f
                                  =297.2) [AC" & N & M & "]")
                                .SetOption("CST C95.3")
                                .SetLabel("SAR" & N & M)
                                .SetOption("volaccuracy
                                  0.000001")
                                .Create
                        End With
                Next M
        Next N

End Sub
```

A.1.2 SAR export

```
'#Language "WWB-COM"

Option Explicit

Sub Main
        Dim NumChannel As Integer
        Dim FieldName As String
        Dim N,M As Integer
        Dim x0,x1,y0,y1,z0,z1,s As Double

        x0=CDbl("x0_exp")
        x1=CDbl("x1_exp")
        y0=CDbl("y0_exp")
        y1=CDbl("y1_exp")
        z0=CDbl("z0_exp")
        z1=CDbl("z1_exp")

        s=2

        NumChannel = 4

        For N = 1 To NumChannel
                For M = 1 To NumChannel
                        SelectTreeItem ("2D/3D Results\SAR\SAR"
                           & N & M)
                        Plot3DPlotsOn2DPlane False
                        With ASCIIExport
                             .Reset
                             .FileName(GetProjectPath("Project")
                                & "\SAR" & N & M & ".csv")
                             .Mode("FixedWidth")
                             .SetfileType("csv")
                             .SetCsvSeparator(",")
                             .Step(s)
                             .SetSubvolume(x0,x1,y0,y1,z0,z1)
                             .UseSubvolume(1)
                             .Execute
                        End With
                Next M
        Next N
```

```
End Sub
```

A.1.3 B1 export

```
'#Language "WWB-COM"

Option Explicit

Sub Main
        Dim NumChannel As Integer
        Dim FieldName As String
        Dim N,M As Integer
        Dim x0,x1,y0,y1,z0,z1,s As Double

        x0=cdbl("x0_exp")
        x1=cdbl("x1_exp")
        y0=cdbl("y0_exp")
        y1=cdbl("y1_exp")
        z0=cdbl("z0_exp")
        z1=cdbl("z1_exp")

        s=2

        NumChannel = 6

        For N = 1 To NumChannel
                SelectTreeItem ("2D/3D Results\B1+ and B1-\B1+ (
                    f=297.2) [AC" & N & N & "]")
                Plot3DPlotsOn2DPlane False
                With ASCIIExport
                     .Reset
                     .FileName(GetProjectPath("Project") & "\b1t
                        " & N & ".csv")
                     .Mode("FixedWidth")
                     .SetfileType("csv")
                     .SetCsvSeparator(",")
                     .Step(s)
                     .SetSubvolume(x0,x1,y0,y1,z0,z1)
                     .UseSubvolume(1)
                     .Execute
                End With
                SelectTreeItem ("2D/3D Results\B1+ and B1-\B1- (
```

```
                f=297.2) [AC" & N & N & "]")
            Plot3DPlotsOn2DPlane False
            With ASCIIExport
                .Reset
                .FileName(GetProjectPath("Project") & "\b1r"
                    & N & ".csv")
                .Mode("FixedWidth")
                .SetfileType("csv")
                .SetCsvSeparator(",")
                .Step(s)
                .SetSubvolume(x0,x1,y0,y1,z0,z1)
                .UseSubvolume(1)
                .Execute
            End With
        Next N

End Sub
```

A.1.4 Prostate mask generation

```
'#Language "WWB-COM"

Option Explicit
Sub Main
        ResultOperator3D.Initialize(Mesh.GetNx, Mesh.GetNy, Mesh
            .GetNz, "scalar")
        ResultOperator3D.FlagByMaterial("Voxel Data/Prostate")
        ResultOperator3D.SetType("dynamic sar")
        ResultOperator3D.Save(GetProjectPath("Result") & "\
            MaskProstate.rex")
        ResultOperator3D.Load(ResultOperator3D.GetFileName)
        ResultOperator3D.AddToTree("2D/3D Results\Mask\
            MaskProstate", "MaskProstate.rex")
End Sub
```

A.2 MATLAB scripts

A.2.1 B1 export parsing

```
function b1 = ReadB1(name)
    tmp = readmatrix(name);

    dim = zeros([1 3],'uint32');
```

```
    dim(1) = find(tmp(2:end,1) == tmp(1,1), 1, 'first');
    dim(2) = find(tmp(dim(1)+1:dim(1):end,2) == tmp(1,2), 1, '
        first');
    dim(3) = size(tmp, 1)/(dim(1) * dim(2));

    b1 = zeros(dim);
    b1(:,:,:) = reshape(tmp(:,8) + 1i * tmp(:,9), dim);
```

A.2.2 B1 results concatenation

```
function b1=CompileB1(ftx,frx,out_name)
    tx_list = afir_dir(ftx);
    rx_list = afir_dir(frx);

    b1.tx = ReadB1(tx_list(1).path);
    b1.rx = ReadB1(rx_list(1).path);
    b1.pos = ReadB1Pos(tx_list(1).path);

    for n = 2:size(tx_list,1)
        b1.tx = cat(4,b1.tx,ReadB1(tx_list(n).path));
        b1.rx = cat(4,b1.rx,ReadB1(rx_list(n).path));
    end

    m = matfile(out_name,'Writable',true);
    m.tx = b1.tx;
    m.rx = b1.rx;
    m.pos = b1.pos;

function pos = ReadB1Pos(name)
    tmp = readmatrix(name);

    dim = zeros([1 3],'uint32');
    dim(1) = find(tmp(2:end,1) == tmp(1,1), 1, 'first');
    dim(2) = find(tmp(dim(1)+1:dim(1):end,2) == tmp(1,2), 1, '
        first');
    dim(3) = size(tmp, 1)/(dim(1) * dim(2));

    pos = zeros([dim 3]);
    pos(:,:,:,:) = reshape([tmp(:,1) tmp(:,2) tmp(:,3)], [dim
        3]);
```

A.2.3 SAR export parsing

```
function [sar, stepsize] = LoadSARDataCST(name)
    tmp = readmatrix(name);
    stepsize = abs(tmp(1,1) - tmp(2,1));
    dim = zeros([1 3],'uint32');
    for n = 1:3
        dim(n) = (max(tmp(:,n), [], 'all') - min(tmp(:,n), [], '
            all'))/stepsize + 1;
    end
    sar = reshape(tmp(:,4), dim);
```

A.2.4 Q matrix array generation

```
function qmat = GenQMat(name, nTx)
    opts = detectImportOptions(sprintf(name, 1, 1));
    opts.SelectedVariableNames = 4;
    tmp = readmatrix(sprintf(name, 1, 1), opts);
    sar = zeros(nTx, nTx, size(tmp, 1));
    qmat = sar;
    for n = 1:nTx
        for m = 1:nTx
            sar(n, m, :) = readmatrix(sprintf(name, n, m), opts)
                ;
        end
    end
    for n = 1:nTx
        for m = 1:nTx
            if n == m
                qmat(n, m, :) = sar(n, m, :);
            elseif n < m
                qmat(n, m, :) = (sar(n, m, :) - 1i.*(sar(m, n,
                    :)) - (sar(n, n, :) + sar(m, m, :)).*(1 - 1i)
                    )/2;
            else
                qmat(n, m, :) = conj(qmat(m, n, :));
            end
        end
    end
end
```

A.2.5 Coil B1+ and SAR performance assessment

```
clc;
close all;
```

```
clear;

load("loop_4x2_b1_duke5mm.mat")
load("loop_4x2_q_duke5mm.mat");
load("loop_4x2_vop03_duke5mm.mat");

maskTarget=LoadSARDataCSTNonunif("mask\MaskProstate.csv");
maskBody=LoadSARDataCSTNonunif("mask\MaskBody.csv");

ntx=size(tx,4);

a=sqrt(50);
k=1e6;

b1=k*reshape(tx(repmat(maskTarget,[1 1 1 ntx])~=0),[],ntx);

u0=cat(1,ones([ntx 1]),zeros([ntx-1 1]));
lb=cat(1,zeros([ntx 1]),-2*pi*ones([ntx-1 1]));
kub=10;
ub=cat(1,kub*ones([ntx 1]),2*pi*ones([ntx-1 1]));

opt=optimoptions("fmincon","Algorithm","sqp");
opt.MaxFunctionEvaluations=1e5;
opt.MaxIterations=1e4;

niter=1e1;
% fval_best=OptSarEff(u0,ntx,a^2*conj(vop),a*b1);
fval_best=OptB1Eff(u0,ntx,a*b1);
u_best=u0;

for n=1:niter
    % [u,fval]=fmincon(@(u)OptSarEff(u,ntx,a^2*conj(vop),a*b1),
      u0,[],[],[],[],lb,ub,[],opt);
    [u,fval]=fmincon(@(u)OptB1Eff(u,ntx,a*b1),u0,[],[],[],[],lb,
      ub,[],opt);
    if fval<fval_best
       fval_best=fval;
       u_best=u;
    end
    u0=cat(1,kub*rand([ntx 1]),2*pi*rand([ntx-1 1])-pi);
end
```

```
v=Par2Vec(u_best,ntx);
v=v/norm(v);

psar=CompPeakSar(q,a*conj(v));
b1mag=abs(a*b1*v);
b1mean=mean(b1mag,"all");
sarEff=b1mean/sqrt(psar);
b1std=std(b1mag,0,"all");
b1homog=1-b1std/b1mean;
b1min=min(b1mag,[],"all");
b1max=max(b1mag,[],"all");

sl=uint16(size(tx,3)/2);

im=squeeze(pagemtimes(v.',permute(tx(:,:,sl,:),[4 1 2 3])));
im=a*abs(im);
im(maskBody(:,:,sl)==0)=0;
% im(maskTarget(:,:,sl)==0)=0;
im_ph=angle(im);

maskTarget(maskTarget>0)=1;
boundaries=bwboundaries(rot90(maskTarget(:,:,sl),-1));
im=rot90(k*im,-1);
clim=k*[0 1e-6];

figure();
hold on
imagesc(im,clim);
thisBoundary = boundaries{1};
x = thisBoundary(:,2);
y = thisBoundary(:,1);
plot(x, y, 'r-', 'LineWidth', 1);
hold off
colormap('jet');
cb=colorbar();
cb.Title.String="uT/sqrt(W)";
xticks([]);
yticks([]);
axis image;
```

```
qp=load("loop_4x2_q_plot_duke5mm.mat");
sar_plt=ComputeSAR(qp.q,a*v);
[~,I]=max(sar_plt,[],"all");
[idx,idy,idz]=ind2sub(size(maskTarget),I);
sar_plt=reshape(sar_plt,size(maskTarget));
im_sar=flip(rot90(sar_plt(:,:,idz),-1),1);

figure();
imagesc(im_sar,[0 psar]);
colormap('jet');
cb=colorbar();
cb.Title.String="W/kg";
xticks([]);
yticks([]);
axis image;

function out=OptSarEff(u,ntx,q,b1)
    v=Par2Vec(u,ntx);
    v=v/norm(v);

    b1mean=mean(abs(b1*v),"all");
    psar=CompPeakSar(q,v);

    out=sqrt(psar)/b1mean;
end

function out=OptB1Eff(u,ntx,b1)
    v=Par2Vec(u,ntx);
    v=v/norm(v);

    out=-mean(abs(b1*v),"all");
end

function psar=CompPeakSar(q,v)
    psar=max(ComputeSAR(q,v));
end

function v=Par2Vec(u,ntx)
    v=u(1:ntx).*exp(1i*[0;u(ntx+1:end)]);
end
```

Chapter 9

AFI reconstruction

9.1 Build directory item list

```
function out = afir_dir(folder)
    out = dir(folder);
    out = rmfield(out,{'date','bytes','datenum'});
    m = 0;
    for n = 1:size(out)
        out(n - m).path = sprintf('%s\\%s', out(n - m).folder,
            out(n - m).name);
        if out(n - m).name == "." || out(n - m).name == ".."
            out(n - m) = [];
            m = m + 1;
        end
    end
```

9.2 AFI reconstruction

```
function [famap, b1] = afir_recon(folder_mag, folder_ph, b1ref)
    mag_list = afir_dir(folder_mag);
    ph_list = afir_dir(folder_ph);

    slices = uint16(size(mag_list,1)/2);
    meta = dicominfo(mag_list(1).path);

    comb = zeros([meta.Height meta.Width 2]);
    famap = zeros([meta.Height meta.Width slices]);

    vref = ParseParams(mag_list(1).path, "sTXSPEC.asNucleusInfo
        [0].flReferenceAmplitude", "=");
```

```
    fa = ParseParams(mag_list(1).path, "adFlipAngleDegree[0]",
        '=');

    tr0 = ParseParams(mag_list(1).path, "alTR[0]", '=');
    tr1 = ParseParams(mag_list(1).path, "alTR[1]", '=');
    n_tr = tr1/tr0;

    for n = 1:slices
        for m = 1:2
            idx = n + (m - 1) * slices;

            mag = double(dicomread(mag_list(idx).path));
            ph = double(dicomread(ph_list(idx).path));
            ph = (ph - 2048)/4096 * 2 * pi;

            comb(:,:,m) = mag.*exp(1j*ph);
        end

        famap(:,:,n) = comb(:,:,2)./comb(:,:,1);
        famap(:,:,n) = real(acosd((famap(:,:,n)*n_tr - 1)./(n_tr
            - famap(:,:,n))));
    end

    b1 = b1ref/(fa/famap * vref);
end

function out = ParseParams(file, name, delim)
    stream = fopen(file,'r');
    while ~feof(stream)
        tok = regexp(fgetl(stream),delim,'split');
        for n = 1:size(tok,2)
            tok(n) = strip(tok(n));
        end
        if tok(1) == name
            out = str2double(tok(2));
            break;
        end
    end
    fclose(stream);
end
```